NTNU Trondheim
Norwegian University of Science and Technology
Department of Marine Technology

PROJECT DESCRIPTION SHEET

Name of the candidate: Svenn Are Tutturen

Field of study: Marine control engineering

Thesis title (Norwegian): Tema innen dynamisk posisjonering: Systemidentifikasjon, estimering av GNSS og MRU målearmer, og hybrid integralregulering.

Thesis title (English): Topics in dynamic positioning: System identification, GNSS and MRU lever arm estimation, and hybrid integral action.

Background

The low-speed dynamic model of a DP vessel is well known, both high fidelity process models and low-fidelity design models. However, the methods and procedures for identification of the model parameters is still a field of development. For specialized vessels such parametric studies are traditionally conducted through model-scale experiments in a model basin and through hydrodynamic computer programs. For full-scale testing, on the other hand, recent technological development of sensor technologies, data acquisition, and communication make more accurate dynamic data available for analysis and estimation of vessel parameters.

The ship R/V Gunnerus, owned by NTNU, is planned in the spring of 2015 to be retrofitted with new podded propulsion. The old propellers and rudders will then be replaced by new prototype podded permanent magnet (PM) azimuth thrusters. As part of this replacement, a study on the efficiency of the thruster system, low-speed responsiveness, and maneuverability of the ship is conducted before and after the retrofit to document changes and improvements to the ship's dynamic behavior. This study is conducted through several sea trials for the ship before and after the retrofit.

The scope of this project is to study thruster dynamics and low-speed ship models for R/V Gunnerus, and to analyze the corresponding sea trials data collected through the different tests on August 14-15, 2013. The objective here is to draw conclusions on methods for and results from system identification of the thruster dynamics and low-speed dynamics of a DP vessel based on numerical studies for R/V Gunnerus. In addition, the objective is to develop a method for estimation of the lever arms for the pos-ref and IMU sensors in the vessel based on persistently exciting motions of the DP vessel.

Work description

1) Perform a literature review, providing relevant references, on:
   - Modeling of thruster dynamics and low-speed dynamics for DP vessels.
   - Methods for system identification, especially step tests and system identification software.

   Write a list with abbreviations and definitions, and a section explaining particularly relevant terms and concepts related to DP systems and system identification methods in an alphabetic order.
2) Propose relevant dynamic models for low-speed thruster and rudder dynamics, considering particularly:
   - advanced model(s) (incl. the relationships between thrust force, RPM, and power),
   - simplified model(s) that are appropriate for system identification based on available measurements, and
   - thruster configuration and net thruster force/moment (thrust allocation).
3) Propose relevant dynamic models for low-speed and wave motions of a DP vessel, considering particularly:
   - high-fidelity models incl. environmental loads, and
   - simplified low-fidelity models (3 DOF DP; forward speed dynamics; steering dynamics) appropriate for system identification based on available measurements.

4) Analyze the results from Test "006 – Thrust agility test" and the settling times for the produced thrust in each commanded thrust direction. Generate a polar plot with response time in the radial direction and plot the corresponding envelopes for thrust response and speed response based on the different tests carried out.
5) Analyze the results from Test "4-corner DP maneuver". Based on the KM log, report in a table the duration for each of the 4 maneuvers, and the accumulated thrust force and power for each thruster during each of the 4 maneuvers and in total. Repeat the analysis for the same tests conducted later on 06.11.2013 and compare and discuss the results.
6) For each of the subtests conducting pure DP (zero speed) in the test reports of 15.08.2013 and 08.11.2013, make a table and report the following values (based on a 5 min. interval of the test): Average wind; Observed waves; Ocean current; Positioning and heading accuracy (Std); Average thruster force and accumulated power (energy).
7) Based on step test responses for Gunnerus, identify relevant thrust T $[N]$ and propeller speed n $[rps]$ time constants for the thrusters.
8) Based on step test responses in surge for Gunnerus, and assuming the thruster steps respond instantaneously, identify relevant surge speed u $[m/s]$ time constants for the ship.
9) Based on step test responses in sway for Gunnerus, and assuming the thruster steps respond instantaneously, identify relevant sway speed v $[m/s]$ time constants for the ship.
10) Based on step test responses in yaw for Gunnerus, and assuming the thruster steps respond instantaneously, identify relevant yaw rate r $[rad/s]$ time constants for the ship.

11) For the estimation of pos-ref lever arms, show the following:
    - The regressor matrix in an adaptive setup satisfies a PE requirement given some assumptions of motion of the vessel. Conclude with a proposition.
    - The lever arms l_i and the rotation point P_0 are uniformly completely observable through the measurements, given some assumptions of motion of the vessel. Conclude with a proposition.
    - The physical interpretation of the rotation point P_0.

    Then do the following:
    - Propose an observer-based estimation design and conclude with a theorem.
    - Propose an alternative estimation design (adaptive, RLS, etc.) and conclude with a theorem.
    - Verify the methods using relevant sea-trial tests for Gunnerus as a case study.
    - Discuss the numerical results of the two estimation methods when compared to the real measured values on the ship.
12) Propose a setup for also including the MRUs into the lever arm identification system:
    - Derive and discuss the observability properties of the system.
    - Propose a numerical estimation design based on measurements during vessel motion.
    - Verify the method using Gunnerus sea-trial as a case study and discuss the results.

Tentatively:

13) Derive a hybrid "PID-type" DP control law, including a discrete resetting of the integral action to better compensate fast variations in the bias forces. Prove stability of the resulting closed-loop hybrid dynamical system, and perform simulations to verify the effectiveness of the algorithm compared to a conventional design.

Guidelines
The scope of work may prove to be larger than initially anticipated. By the approval from the supervisor, described topics may be deleted or reduced in extent without consequences with regard to grading.

The candidate shall present his personal contribution to the resolution of problems within the scope of work. Theories and conclusions should be based on mathematical derivations and logic reasoning identifying the various steps in the deduction.

The report shall be organized in a rational manner to give a clear exposition of results, assessments, and conclusions. The text should be brief and to the point, with a clear language. The report shall be written in English (preferably US) and contain the following elements: Abstract, acknowledgements, table of contents, main body, conclusions with recommendations for further work, list of symbols and acronyms, references, and (optionally) appendices. All figures, tables, and equations shall be numerated. The original contribution of the candidate and material taken from other sources shall be clearly identified. Work from other sources shall be properly acknowledged using quotations and a Harvard citation style (e.g. *natbib* Latex package). The work is expected to be conducted in an honest and ethical manner, without any sort of plagiarism and misconduct. Such practice is taken very seriously by the university and will have consequences. NTNU can use the results freely in research and teaching by proper referencing, unless otherwise agreed upon.

The thesis shall be submitted with two printed and electronic copies, to 1) the main supervisor and 2) the external examiner, each copy signed by the candidate. The final revised version of this work description must be included. The report must appear in a bound volume or a binder according to the NTNU standard template. Computer code and a PDF version of the report shall be included electronically.

Start date: 1 February, 2014 **Due date:** As specified by the administration.

Supervisor: Roger Skjetne
Co-advisor(s): Øivind K. Kjerstad

Trondheim, _____

_____
Roger Skjetne
Supervisor

Summary

This thesis consists of three main parts. The first part of the master thesis looks at the identification of thruster dynamics and low speed ship dynamics. The relevant parameters identified are time constants and time delays in the system. Simple step tests are used for the identification. Different models for identification are suggested, both for uncoupled surge, sway, and yaw dynamics. Other test results, such as agility plots, DP 4 corner tests, and pure DP tests (stationkeeping) are reported. All the results are to be compared to similar tests performed after R/V Gunnerus has a retrofit of the thruster system.

The second part discusses another problem, and that is the topic of numerically estimating the body frame position of the GNSS and MRU sensors. For the GNSS position an Luenberger observer design and an adaptive scheme are proposed and analyzed. The estimation designs are tested using numerical simulations and experimental data from the Gunnerus sea trials. A similar Luenberger observer is proposed for the MRU positions, and experimental data from the sea trials are used to test the observer.

The third part discusses a hybrid augmentation of integral action. The motivation is a DP system, where typically the integral action is tuned very low to avoid oscillations due to the integral action. When there is a sudden load change, such as a ice load that hits the vessel, or if a mooring wire snaps, then a hybrid update augmentation could be useful, to speed up the convergence of the integral action. The update law is a linear update law based on the error in the states (the velocity for the DP system). The augmentation can significantly improve performance, especially for very large disturbance changes.

Sammendrag

Denne avhandlingen består av tre hoveddeler. Den første delen av masteravhandlingen ser på identifisering av thrusterdynamikk og lavhastighets skipsdynamikk. Relevante parametre som blir identifisert er tidskonstanter og tidsforsinkelser i systemet. Enkle sprangresponser er brukt i identifikasjonen. Forskjellige modeller for identifisering er foreslått, både for jag-, svai- og gir-dynamikk. Ander testresultater, deriblant en grafisk fremstilling av thrusterrespons, en DP-manøver i lav hastighet, samt en DP-manøver hvor skipet holder seg i ro er rapportert. Alle resultatene vil bli sammenlignet med lignende tester etter FF Gunnerus har fått ombygd sitt thrustersystem.

Del to av avhandlingen omhandler en annen problemstilling, og det er å numerisk estimere armene til GNSS- og MRU-sensorer. For GNSS-problemet så er et Luenberger estimatordesign presentert, og en adaptiv løsning er også foreslått og analysert. De foreslåtte estimatorene er testet ved å bruke numeriske simuleringer som benytter eksperimentell data fra sjøprøvene med FF Gunnerus. Et lignende Luenberger-oppsett er foreslått for MRU-armene, og eksperimentell data fra sjøprøvene er brukt til teste estimatoren.

Den tredje delen diskuterer en hybrid augmentering til integraleffekt i en kontroller. Motivasjonen er dynamisk posisjonering, hvor integraleffekten typisk er stilt inn ganske lavt for å forhindre at integraleffekten induserer svingninger i systemet. Når det intreffer en plutselig lastforandring, for eksempel fra en islast, eller at en forankringsline ryker, så kan det være nyttig med en hybrid augmentasjon av integraleffekten, for å øke hastigheten til integraleffekten sin konvergens. Oppdateringsloven er proposjonal med størrelsen til feilen i tilstandene i systemet (for det foreslåtte DP-systemet brukes feilen i hastighet for å bestemme denne størrelsen). Denne hybride augmenteringen kan øke ytelsen til systemet, spesielt ved store og plutselige lastendringer.

Acknowledgement

This thesis was completed between January and July 2014 alongside a course for the integrated PhD studies as the last part of my master's degree in Marine Technology at the Norwegian University for Science and Technology (NTNU).

The two first parts of the thesis are a continuation of the project thesis from last semester. This is a stand alone thesis, and the project thesis is not needed for the understanding of this work. The third and last part of the Thesis is an extension of a paper written for the PhD course MR8500 - Advanced Topics in Marine Control Systems.

I would like to thank the crew at R/V Gunnerus for two pleasant cruises (sea trials), and MARINTEK for all the data collection. I would like to thank Seatex for the MRUs at R/V Gunnerus, and allowing us to use the data from these, and I would like to thank Professor Sverre Steen at the Department of Marine Technology, NTNU, that have led the sea trials.

I would especially like to thank my supervisor Professor Roger Skjetne at the Department of Marine Technology, NTNU. He has been a great motivation for the study of control theory, especially the nonlinear part. Roger has also helped guide me through the master thesis, and I am grateful. I would also like to thank Professor Andrew Teel at UCSB that taught MR8500 (at NTNU) in hybrid control theory, and he has been a great inspiration for working on hybrid control. Lastly, I would like to thank my co-advisor PhD candidate Øivind K. Kjerstad at the Department of Marine Technology for helpful discussions.

Table of Contents

List of Tables

List of Figures

Definitions

BODY frame a reference frame fixed to the craft, where the x axis points forward (from aft to fore), the y axis to starboard, and the z axis points down (Fossen, 2011)

Dynamically positioned vessel a free-floating vessel which maintains its position (fixed location or predetermined track) exclusively by means of thrusters (Fossen, 2011)

Maneuvering the study of ship motion in the absence of wave excitation (Fossen, 2011)

NED frame a reference frame with x axis to pointing to the true North, y axis pointing East, and z axis pointing down, normal to the Earth. Considered interial for a marine vessel operating in a local area (Fossen, 2011)

Seakeeping the study of motion of a marine craft on constant course and speed when there is wave excitation (Fossen, 2011)

List of acronyms

DOF Degree of freedom

DP Dynamic positioning

fb feedback

FOPDT First order plus dead time

GNSS Global navigation satellite system

GPS Global positioning system

INS Inertial navigation system

LTV Linear time varying

MRU Motion reference unit

N North

NE Northeast

NED North, east, down

NW Northwest

PE Persistence of excitation

PID Proportional, integral, derivative

rpm revolutions per minute

rps revolutions per second

S South

sb starboard

SE Southeast

SW Southwest

UGAS Uniformly globally asymptotically stable

UGpAS Uniformly globally pre-asymptotically stable

Nomenclature

$\boldsymbol{\eta}$	orientation vector in NED-coordinates
$\boldsymbol{\nu}$	body fixed velocity vector
$\boldsymbol{\omega}$	body fixed angular velocity vector
$\boldsymbol{\Theta}$	vector of Euler angles
$\boldsymbol{x}$	state vector
$\boldsymbol{y}$	output (response)
δ	time delay
T	time constant

Notation

Lower case bold letters, such as $\boldsymbol{x}$ indicate a vector, and uppercase bold letters such as $\boldsymbol{A}$ represent matrices.

Time derivatives are indicated by the dot notation, such that $\dot{x}$ is the time derivative of x. For discrete updates the notation x^+ is used to indicate the value of x after a discrete update.

Chapter 1

Introduction

1.1 Background

Dynamic positioning (DP) of marine vessels are a well-established commercial application which enables automatic position and heading control in various operational scenarios (see for instance (Kongsberg Maritime, 2006) and (Rolls-Royce Marine, 2009)). It is also an established and active field of research (Fossen, 2011). Therefore, developments in control theory and sensor technology that may improve performance and/or reduce the economical effort of designing, verifying, and operating such systems are of interest.

This thesis considers three topics which may have such implications:

- Identification of low-speed vessel models and analysis of actuation system performance,
- estimation of GNSS and MRU lever arms based on vessel maneuvering data,
- hybrid integral action for discontinuous updates of the control systems environmental disturbance rejection.

Although each of these topics will be given a more in depth introduction in their respective chapters, the two first topics apply an extensive data set gathered during two sea trial campaigns using the NTNU owned research vessel R/V Gunnerus.

The reason for these sea trials is that R/V Gunnerus has a planned retrofit of the thruster system. Figure 1.1 below show a sketch of the old and new thruster configuration. The illustration show the current thruster configuration with two propellers and rudders in the stern. These will be replaced with two prototype permanent magnet azimuth thrusters. There is also a tunnel thruster in the bow, that will not be replaced.

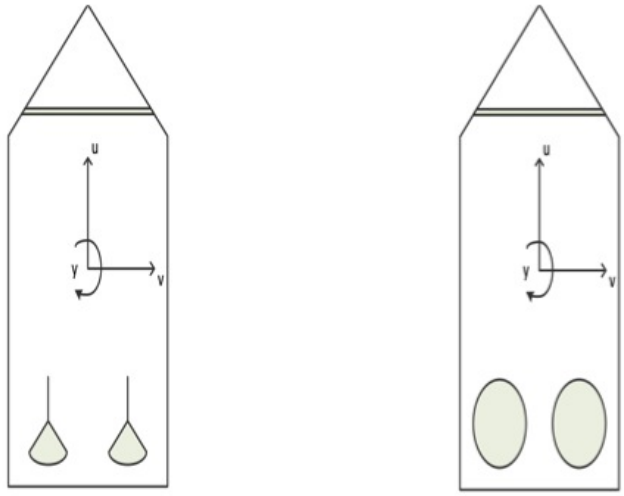

Figure 1.1: Thruster retrofit, illustration - thrust region before (left), and after (right) the retrofit

1.1.1 R/V Gunnerus sea trials

The first sea trial was performed in calm sea in the Trondheimsfjord in August 2013, and the second one in open sea outside Kristiansund in November 2013. The experimental test campaigns ware performed by NTNU and MARINTEK. The tests relevant for this master thesis were performed in order to compare the response and performance of the current thruster configuration of R/V Gunnerus to the retrofit. This include the performance of the thruster system itself, and the performance in DP mode. When the retrofit is finished, there will be more sea trials.

The tests performed relevant for the thesis include several step tests in surge, sway, and yaw, where the thruster response, and the combined thruster and vessel hull response were of interest. Thrust agility tests were performed. This results in a plot showing the time constants of the of the thruster responses in different directions. A step in thrust force is applied for heading of $0°$, $45°$, $90°$, $135°$, $180°$, $-135°$, $-90°$, and $-45°$.

There were performed several stationkeeping tests, referred to as ”pure DP” in this thesis. The reported values include the average thrust force, the power consumption, and the

position accuracy. Another maneuver, called the DP 4 corner, which is more thoroughly explained in Section 3.5.2 was performed. This maneuver tests the performance of the DP system in low speed. The accumulated thrust force, and the accumulated power is logged, along with the duration of the maneuver(s).

All the above tests are meant to give a good platform for comparison when evaluating the performance of the retrofit compared to the old configuration. The tests are all explained more thoroughly in Section 3.5, before the results are presented.

Also, experimental data from some of the performed maneuvers from these sea trials will be used in the lever arm estimation problem.

In the thesis the first sea trial in August is referenced as either the ”sea trial in calm sea” (or calm water), ”the first sea trial”, or ”the sea trial performed in August”. Similarly is the sea trial from November either references as ”the sea trial at sea” (or open sea), ”the second sea trial”, or ”the November sea trial”.

During the two sea trials MARINTEK has logged data, and for the first sea trial the log from the Dynamic Positioning (DP) system was collected. This log was collected by a Kongsberg Maritime representative, and sent to the MARINTEK log. This log is only available from the first sea trial. The data collected exclusively by MARINTEK is referenced as ”MARINTEK data”, or ”data collected by MARINTEK”, and the data from the DP system is referenced as ”the DP data”.

1.2 Main contributions

For the system identification part of Chapter 3 simple models for identification are proposed, and the response of thruster system, and the combined response of the thruster system and the vessel are reported. Data from several DP maneuvers are reported, such that the data can be compared to R/V Gunnerus data after retrofit.

In Chapter 4 the main contribution are algorithms that estimate several GNSS (or MRU) sensor lever arms, by using a simple setup without including the INS, and for the GNSS case the algorithms use the vessel velocity, and the raw data from GNSS anteannas only.

In Chapter 5 the main contribution are the rigorous stability proofs of the hybrid system for both the first order linear system, and the DP system. In this thesis limits for how large these discrete updates can be has been found, and it is proven to be stable.

1.3 Thesis structure

In Chapter 2 modeling relevant for the other chapters is covered. This includes modeling of vessel kinetics and kinematics, and thruster dynamics. High fidelity models are covered, and also the decoupled, and simplified models needed for system identification in Chapter 3.

In Chapter 3 system identification by step tests are discussed, before suggested models used for the identification are proposed. In Section 3.5 the step tests are analyzed, and other test results are presented, such as the thrust agility tests, DP 4 corner, and pure DP tests (stationkeeping).

Chapter 4 discuss and analyze the lever arm estimation problem, and results on experimental data are presented. In Chapter 5 the hybrid integral action is presented, and analyzed, before simulation results are shown on a first order linear system, and a DP system.

Chapter 3 - 5 each discuss a separate topic, and each chapter has a conclusion including suggestions for further work within the respective chapters. This is because each chapter presents results and they are separate in their topic.

Chapter 2

Modeling

2.1 Vessel models

The modeling of following section is to a high degree based on material from Fossen (2011).

Vessel kinetics is normally expressed in BODY-frame, and the kinematics in North-East-Down (NED)-frame. There exists numerous models with varying complexity, dependent on operation. The main difference is for high- and low-speed applications, where different forms of hydrodynamic damping dominate for different speed regimes, and the Coriolis and centripetal terms become negligible for low speed.

2.1.1 High fidelity model

Kinematics

Vessel kinematics is given as (Fossen, 2011)

$$\dot{\boldsymbol{\eta}} = \boldsymbol{R}(\boldsymbol{\Theta})\boldsymbol{\nu}, \tag{2.1}$$

where

$$\boldsymbol{\eta} = \begin{bmatrix} N & E & D & \phi & \theta & \psi \end{bmatrix}^\top \in \mathbb{R}^{6\times 1}, \tag{2.2}$$

contain the North, East, and down positions, and the angular orientation (Euler angles) in roll (ϕ), pitch (θ), and yaw (ψ). The velocity vector $\boldsymbol{\nu}$ is given as

$$\boldsymbol{\nu} = \begin{bmatrix} u & v & w & p & q & r \end{bmatrix}^\top \in \mathbb{R}^{6\times 1}, \tag{2.3}$$

where u, v, and w are the velocities in surge (x-direction), sway (y-direction), and heave (down-direction), respectively. The other half of $\boldsymbol{\nu}$ is given by the angular velocities in roll (p), pitch (q), and yaw (r). The $\boldsymbol{\eta}$ vector is given in NED-coordinates, and $\boldsymbol{\nu}$ in BODY-coordinates. The rotation matrix $\boldsymbol{R}(\boldsymbol{\Theta})$ transforms the coordinate frame between BODY to NED and is given as

$$\boldsymbol{R}(\boldsymbol{\Theta}) = \begin{bmatrix} c\psi c\theta & -s\psi c\phi + c\psi s\theta s\phi & s\psi s\phi + c\psi c\phi s\theta \\ s\psi c\theta & c\psi c\phi + s\phi s\theta s\psi & -c\psi s\phi + s\theta s\psi c\phi \\ -s\theta & c\theta s\phi & c\theta c\phi \end{bmatrix} \in \mathbb{R}^{3\times 3}, \tag{2.4}$$

where $c(\cdot) = \cos(\cdot)$, $s(\cdot) = \sin(\cdot)$.

Also, the time derivative of the rotation matrix is given by

$$\dot{\boldsymbol{R}}(\boldsymbol{\Theta}) = \boldsymbol{R}(\boldsymbol{\Theta})\boldsymbol{S}(\boldsymbol{\omega}) \tag{2.5}$$

where $\boldsymbol{S}(\boldsymbol{\omega})$ is a skew-symmetric matrix given by

$$\boldsymbol{S}(\boldsymbol{\omega}) = \begin{bmatrix} 0 & -r & q \\ r & 0 & -p \\ -q & p & 0 \end{bmatrix}. \tag{2.6}$$

Kinetics

The vessel kinetics is generally given as (Fossen, 2011)

$$\boldsymbol{M}_{RB}\dot{\boldsymbol{\nu}} + \boldsymbol{C}_{RB}(\boldsymbol{\nu})\boldsymbol{\nu} + \boldsymbol{M}_A(\boldsymbol{\nu}_r)\boldsymbol{\nu}_r + \boldsymbol{C}_A(\boldsymbol{\nu}_r)\boldsymbol{\nu}_r + \boldsymbol{D}(\boldsymbol{\nu}_r)\boldsymbol{\nu}_r + \boldsymbol{g} = \boldsymbol{\tau} + \boldsymbol{\tau}_{wind} + \boldsymbol{\tau}_{wave}. \tag{2.7}$$

The terms in the equations are

- relative velocity $\boldsymbol{\nu}_r = \boldsymbol{\nu} - \boldsymbol{\nu}_c$, where $\boldsymbol{\nu}_c$ is the velocity of the current,
- interia terms: $\boldsymbol{M}_{RB}$ (rigid body) and $\boldsymbol{M}_A$ (added mass)
- Coriolis and centripetal terms: $\boldsymbol{C}_{RB}$ (rigid body), and $\boldsymbol{C}_A$ (due to added mass),
- damping forces: $\boldsymbol{D}(\boldsymbol{\nu}_r) = (\boldsymbol{D}_p + \boldsymbol{D}_v)$, where $\boldsymbol{D}_p$ is the linear potential damping, and $\boldsymbol{D}_v$ contains the viscous damping (vortex shedding, skin friction),
- restoring forces: $\boldsymbol{g}$ (hydrostatics),
- environmental forces:
  - $\boldsymbol{\tau}_{wind}$: wind forces,
  - $\boldsymbol{\tau}_{wave}$: first order oscillatory waves forces and second order waves forces (mean drift, slowly varying drift forces, sum-frequency forces) (Faltinsen, 1990).
  - current: the forces from the current are included in $\boldsymbol{D}(\boldsymbol{\nu}_r)$ due to the relative velocity $\boldsymbol{\nu}_r$,

- propulsion forces, $\boldsymbol{\tau}$: the forces generated by the thrusters of the vessel

The Coriolis terms are present in the equation because the kinetics is expressed in BODY frame, which is a rotating moving reference frame with respect to an inertial reference frame (Sørensen, 2012).

2.1.2 Uncoupled surge dynamics

From Fossen (2011) the uncoupled surge dynamics for a longitudinally symmetric ship, where m is the mass, $X_{\dot{u}}$ is the added mass in surge, X_u and $X_{|u|u|}$ are linear and nonlinear damping, respectively, can be written

$$(m - X_{\dot{u}})\dot{u} - X_u u_r - X_{|u|u|}|u_r|u_r = \chi, \tag{2.8}$$

where χ comprise of the external forces, and the control input. The nonlinear damping will dominate for higher vessel speeds, and the linear damping dominates for low speeds.

2.1.3 Sway-yaw subsystem

For a constant surge velocity $u \approx u_0$, a linear sway-yaw subsystem, known as the second order Nomoto Model, can be written (Fossen, 2011)

$$\boldsymbol{M}\dot{\boldsymbol{\nu}} + \boldsymbol{N}(u_0)\boldsymbol{v}_r = \boldsymbol{b}\alpha \tag{2.9}$$

with

$$\boldsymbol{M} = \begin{bmatrix} m - Y_{\dot{v}} & mx_g - Y_{\dot{r}} \\ mx_g - Y_{\dot{r}} & I_z - N_{\dot{r}} \end{bmatrix} \in \mathbb{R}^{2\times 2}, \tag{2.10}$$

and $\boldsymbol{N} \in \mathbb{R}^{2\times 2}$ contain the speed dependent terms from $\boldsymbol{C}(\boldsymbol{v})$ and the linear damping matrix, $\boldsymbol{D}$ from Eq. (2.7) (Fossen, 2011). The rudder angles are collected in the vector $\boldsymbol{\alpha}$. Let the α in Eq. (2.9) be a scalar. To relate this to the tests with R/V Gunnerus, that has two rudders, assume that the rudders have an equal angle, and thus modelled as a single rudder. Looking at the transfer function from the rudder angle to the yaw-rate, it can be written as (Fossen, 2011)

$$\frac{r}{\alpha}(s) = \frac{K_y(1 + T_3 s)}{(1 + T_1 s)(1 + T_2 s)}. \tag{2.11}$$

Also, for the sway motion a similar relationship is found as

$$\frac{v}{\alpha}(s) = \frac{K_v(1 + T_v s)}{(1 + T_1 s)(1 + T_2 s)}, \tag{2.12}$$

where r is the yaw rate, and v is the sway velocity, $K_y,\ K_v$ are the steady state gains, and $T_1,\ T_2$, and T_3 are the time constants.

First order approximation

Fossen (2011) defines a equivalent time constant so that from (2.11) the equivalent time constant T_r is defined as

$$T_r := T_1 + T_2 - T_3, \tag{2.13}$$

and from (2.12) the equivalent time constant $T_{\bar{v}}$ is defines as

$$T_{\bar{v}} := T_1 + T_2 - T_v, \tag{2.14}$$

and hence, the models given by (2.11) and (2.12) can be approximated by the first order models as

$$\frac{r}{\delta}(s) = \frac{K_y}{1 + T_r s}, \tag{2.15}$$

and

$$\frac{v}{\delta}(s) = \frac{K_v}{1 + T_{\bar{v}} s}. \tag{2.16}$$

2.1.4 Low speed models

For low speed applications, like dynamic positioning, the linear damping will dominate the nonlinear part (Fossen, 2011), so $\boldsymbol{D}(\boldsymbol{\nu}_r) \approx \boldsymbol{D}\boldsymbol{\nu}$, where $\boldsymbol{D}$ is the linear damping matrix. The Coriolis and centripetal terms can be neglected, also due to low speed.

DP (3 DOF) - Linearized model

For dynamic positioning of a vessel it is common to restrict the workspace to 3 degrees of freedom (DOF). Only the horizontal plane (surge, sway and yaw) is considered, and this gives $\boldsymbol{\eta}$ and $\boldsymbol{\nu}$ as

$$\boldsymbol{\eta} = \begin{bmatrix} N & E & \psi \end{bmatrix}^\top \tag{2.17}$$

$$\boldsymbol{\nu} = \begin{bmatrix} u & v & r \end{bmatrix}^\top, \tag{2.18}$$

and the rotation matrix reduces to

$$\boldsymbol{R}(\boldsymbol{\Theta}) = \boldsymbol{R}(\psi) = \begin{bmatrix} \cos(\psi) & -\sin(\psi) & 0 \\ \sin(\psi) & \cos(\psi) & 0 \\ 0 & 0 & 1 \end{bmatrix}. \tag{2.19}$$

In the linearized DP model the slowly varying drift forces, mean drift forces, and the current are all collected into a bias $\boldsymbol{b}$. Since current is captured in the bias, the relative velocity vector is not included in the model anymore (it becomes superfluous) (Fossen, 2011).

The kinematics and kinetics for the linearized 3 DOF DP model is written as (Fossen, 2011)

$$\dot{\boldsymbol{\eta}} = \boldsymbol{R}(\psi)\boldsymbol{\nu} \tag{2.20}$$

$$\boldsymbol{M}\dot{\boldsymbol{\nu}} + \boldsymbol{D}\boldsymbol{\nu} = \boldsymbol{R}^T(\psi)\boldsymbol{b} + \boldsymbol{\tau} + \boldsymbol{\tau}_{wind} + \boldsymbol{\tau}_{wave1} \tag{2.21}$$

$$\dot{\boldsymbol{b}} = -\boldsymbol{T}^{-1}\boldsymbol{b} + \boldsymbol{w}_b \quad (\text{ or } \dot{\boldsymbol{b}} = \boldsymbol{w}_b), \tag{2.22}$$

where $\boldsymbol{w}_b$ is white Gaussian noise (Sørensen, 2012), and $\boldsymbol{\tau}_{wave1}$ comprise only of the first order wave forces. The bias force is modeled by a Gauss-Markov process above, and could also be modeled as a white noise process (Sørensen, 2012), which is given in parenthesis in Eq. (2.22). Here $\boldsymbol{b}$ is a slowly varying disturbance or bias force, and the linear damping matrix satisfies $\boldsymbol{D} > 0$.

2.2 Thruster dynamics

This section is based on Sørensen (2012), and Smogeli (2006). Please see these references for more in-depth analysis of thruster control, especially other control strategies such as torque control, and combined torque and power control. Only speed control will be covered in the following, both because this is the most common strategy, and because it is the algorithm used for thruster control at Gunnerus (Schultz, 2013).

Thruster control is an important aspect, and good control algorithms can save fuel, and wear and tear of the equipment. Based on the force demand calculated from the high level DP controller, or from manual control, the thrust allocation distributes the force demand to each thruster. Based on the required force given by the thrust allocation, the low level thruster controller calculates the desired shaft speed of the propeller. Other possible control strategies include torque control, and power control.

The low level thruster control scheme consists of five main components (Sørensen, 2012). There is a reference generator to ensure physically feasible input, a core controller (feedback controller), a friction feedforward term, a intertia feedforward term, and a torque saturation block to limit the commanded torque within allowed (and physical) limits. This commaned torque, Q_c is fed into the electric motor, and the motor dynamics can be modelled as a first order model such as

$$\dot{Q}_m = \frac{1}{T_m}(Q_m - Q_c), \tag{2.23}$$

where Q_m, Q_c, and T_m are the actual motor torque, the commanded motor torque, and the first order time constant for the motor dynamics, respectively. The shaft dynamics is given as

$$I_s\dot{\omega} = Q_m - Q_a - K_\omega\omega, \tag{2.24}$$

where I_s, Q_a, K_ω, and ω are the shaft inertia, the propeller load torque, the friction coefficient, and the shaft speed respectively. Finally, hydrodynamic loss effects will affect the

delivered thrust. The thrust force actually delivered after losses have been accounted for is called the actual thrust T_a. For a DP vessel typical loss effects are (Sørensen, 2012)

- in-line velocity fluctuations,
- cross-coupling drag,
- Coanda effect,
- ventilation,
- in-and-out-of-water-effects,
- thruster-thruster interaction.

For R/V Gunnerus ventilation is only a problem in rough weather when the propellers comes close to the surface, and similarly for in-and-out-of-water-effects (really bad weather). The tunnel thruster is only effective for low-speed, and will become inefficient at higher speed due to cross-coupling drag.

The relationship between actual thrust force $T_a[N]$ and actual torque $Q_a[Nm]$, with the shaft speed of the thruster are given by (Sørensen, 2012)

$$T_a = sign(n)\rho K_T D^4 n^2, \tag{2.25}$$

$$Q_a = sign(n)\rho K_Q D^5 n^2, \tag{2.26}$$

where $n[\frac{1}{s}]$ is the shaft speed, $\rho[\frac{kg}{m^3}]$ is the water density, $D[m]$ the propeller diameter, and $K_T[-] > 0$, and $K_Q[-] > 0$ are the thrust and torque coefficients, respectively. Values for K_T and K_Q are found from open water tests. Both coefficients are a function of a number of parameters, the advance ratio, the expanded blade area (ratio), the pitch ratio, and the number of blades. For Q_a the Reynold number and the maximum thickness of the blade with respect to the chord length is also of importance. The advance ratio J_a is given as

$$J_a = \frac{V_a}{nD}, \tag{2.27}$$

where V_a is the inflow velocity on the propeller.

The power consumption can be found from (Sørensen, 2012)

$$P_a = 2\pi n Q_a = sign(n)2\pi K_Q \rho D^5 n^3. \tag{2.28}$$

2.2.1 Simplified model

According to Strand et al. (2001), full scale experiments have shown that the thruster dynamics can be modelled as a first order process with quite satisfactory results. This gives the thruster dynamics as

$$\dot{T}_m = -A_{thr}^{-1}(T_m - T_c) \tag{2.29}$$

where T_m and T_c are obtained and commanded thrust, respectively. $A_{thr} \in \mathbb{R}^{3\times3}$ is a diagonal matrix containing the time constants for the thrust in surge, sway, and yaw direction, respectively. This model is applicable for the step test analysis, and will be used in the system identification process.

2.2.2 Thrust allocation

The DP controller (or manual control by levers) calculates desired force and moment to be applied in surge, sway, and yaw. Thrust allocation is the process of distributing this force demand on the thrusters of the vessel, and the low level thruster controller map this to a desired shaft speed of the individual thrusters (Sørensen, 2012). In the case of an overactuated vessel, the thrust allocation problem becomes an optimization problem. Most DP vessels are overactuated. Generally, the thrust force is written as (Fossen, 2011)

$$\boldsymbol{\tau} = \boldsymbol{T}(\boldsymbol{\beta})\boldsymbol{K}\boldsymbol{u}, \tag{2.30}$$

where $\boldsymbol{\beta}$ is a vector of the azimuth angles. Let n be the number of DOF's, and r be the number of thruster, then the thrust configuration matrix $\boldsymbol{T}(\boldsymbol{\beta}) \in \mathbb{R}^{n\times r}$ geometrically describes the thruster position and their orientation with respect to the centre of rotation. The matrix $\boldsymbol{K} \in \mathbb{R}^{r\times r}$ is a diagonal matrix containing the thrust coefficients. For speed controlled thrusters, $\boldsymbol{K}$ and $\boldsymbol{u} \in \mathbb{R}^r$ are given as

$$\begin{aligned}\boldsymbol{K} &= diag\{k_1, \quad k_2, \quad \cdots, \quad k_r\} \\ &= diag\{\rho K_{T1} D_1^4, \quad \rho K_{T2} D_2^4, \quad \cdots, \quad \rho K_{Tr} D_r^4\},\end{aligned} \tag{2.31}$$

$$u = \begin{bmatrix} |n_1|n_1 \\ |n_2|n_2 \\ \cdots \\ |n_r|n_r \end{bmatrix}. \tag{2.32}$$

For R/V Gunnerus (before retrofit), there are two main fixed pitch propellers (Sørensen, 2012) with rudder in the stern, and a tunnel thruster in the bow (no azimuth thrusters). Given the following definitions

$$u_1 : \text{port main propeller} \tag{2.33}$$

$$u_2 : \text{starboard main propeller} \tag{2.34}$$

$$u_3 : \text{tunnel thruster, bow,} \tag{2.35}$$

and let l_1, l_1 and l_3 be the moment arms in yaw for u_1, u_2 and u_3, respectively. For $F_1 = k_1 u_1$, $F_2 = k_2 u_2$, and $F_3 = k_3 u_3$, the thrust configuration is shown in Figure 2.1.

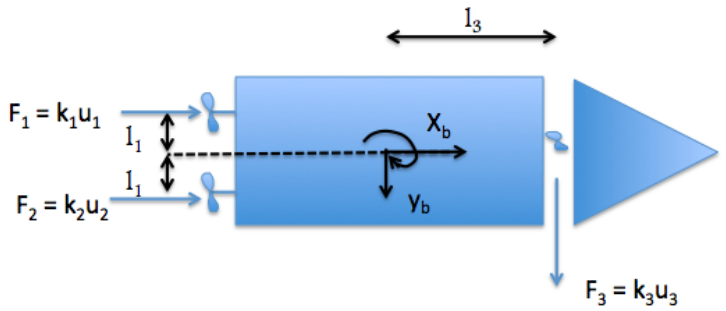

Figure 2.1: Thruster configuration, Gunnerus - before retrofit (bow to the right)

Be defining the rudder angles $\boldsymbol{\alpha}$ as

$$\boldsymbol{\alpha} = \begin{bmatrix} \alpha_1 & \alpha_2 \end{bmatrix}^T \in \mathbb{R}^2, \tag{2.36}$$

where α_1 and α_2 are the rudder angles of the port and starboard rudder, respectively, the thrust configuration matrix is written as

$$\boldsymbol{T} = \begin{bmatrix} b_{11}(\alpha) & b_{12}(\alpha) & 0 \\ b_{21}(\alpha) & b_{22}(\alpha) & 1 \\ b_{31}(\alpha)l_1 & b_{32}(\alpha)(-l_1) & -l_3 \end{bmatrix}. \tag{2.37}$$

If the surge speed is small, and the tunnel thruster is active, the yaw motion will not depend linearly on the rudder angle as in the sway-yaw subsystem of Section 2.1.3.

Chapter 3

Model Identification

3.1 Introduction

Simple system identification tests as step tests, and the logging of other maneuvers such as different DP maneuvers, are useful to get a rough overview over the performance of the DP system, and of the thruster configuration. R/V Gunnerus has a planned thruster retrofit, and results from simple tests can be used to compare the responsiveness, and effectiveness of the two thruster systems.

Simple identification of performance of the DP system, and time constants found in step tests could also function as a first benchmark for simulators, and the data found could give an indication of the simulator performance.

In this chapter the step tests are analyzed using the plot function in MATLAB, and then the results of the tests are read off manually, using MATLAB plots.

This chapter is structured such that in Section 3.2 system identification by step tests are discussed, before suggested models used for the identification are proposed in Section 3.3. Some data that are needed for the tests are unavailable, and this is discussed in Section 3.4. In Section 3.5 the step tests are analyzed, and other test results are presented, such as the thrust agility tests, DP 4 corner, and pure DP tests (stationkeeping).

3.2 System identification by step tests

3.2.1 First order system

A step test is a system subject to a sudden change in the input reference, a jump/step from one constant value to another. This section takes its results from Palm (2009) and Smith

and Corripio (2006). For a general 1^{st} order system of the form

$$a\dot{y} + by = u, \tag{3.1}$$

$$\rightarrow T\dot{y} + y = \frac{u}{b} \tag{3.2}$$

where T is the time constant, ($T = \frac{a}{b}$). If u is a step input, the response (output) y is given as

$$y(t) = y(0)\mathrm{e}^{-\frac{t}{T}} + \frac{U}{b}(1 - \mathrm{e}^{-\frac{t}{T}}), \tag{3.3}$$

where U is the magnitude of the input (the step). This implies two useful results that can be applied to extract information from a step response of a 1^{st} order system;

- as steady state is reached ($t \rightarrow \infty$) the steady state gain, K_p can be found from

  $$K_p = \frac{\Delta y}{\Delta u}, \tag{3.4}$$

  where Δy and Δu are the change in output and input, respectively, due to the step input. For Eq. (3.3) K_p is

  $$K_p = \frac{\frac{U}{b} - y(0)}{U} = \frac{y_{ss} - y(0)}{U}, \tag{3.5}$$

- for y_{ss} and $y(0)$ representing the steady state output value and output initial value, respectively, the time constant can be found from the response curve as the time difference from the step was applied to the response reaches $y(0) + (1 - \mathrm{e}^{-1})[y_{ss} - y(0)]$. This corresponds to the time it takes for the response to reach about 0.632 of its steady state value.

2^{nd} order system

A general second order system can be written as

$$\frac{K_p}{(T_1 s + 1)(T_2 s + 1)}, \tag{3.6}$$

where K_p is the steady state gain, and T_1 and T_2 are the time constants. It is hard to get the time constants from a second order response curve. However, there are methods for finding both time constants for a second order system, such as "Smith's method" from Seborg et al. (2004) and Smith (1972). Smith's method utilizes a normal step test, and looks at the time at 20% and 60% of the response. Another method is that of Rangaiah and Krishnaswamy (1994) where an overdamped second order process is estimated from a step test by the use of 3 points, 14%, 55%, 91% (Seborg et al., 2004). However, according to Smith and Corripio (2006), methods like these have low precision, since the amount of information contained in a step test is too low. These methods will not be further analyzed. The first order plus dead time (FOPDT) will instead be of main concern for the step tests.

First order plus dead time approximation (FOPDT)

The first order plus dead time approximation method has a transfer function G(s) of the form

$$G(s) = \frac{K_p}{Ts+1}\mathrm{e}^{-\delta s}, \tag{3.7}$$

where δ and T are the dead time and the time constant, respectively. The steady state gain K_p is found from (3.4). The recommended method of Smith and Corripio (2006) for approximating a higher order curve as a FOPDT was initially proposed by Smith (1972). This method is based on the idea that the response curve and the approximated model should coincide at the two points where the rate of change is high. The two chosen points are ($\delta + \frac{T}{3}$) and ($\delta + T$). Using the notation of Smith and Corripio (2006) let $t_1 = \delta + \frac{T}{3}$, and $t_2 = \delta + T$. In other words, t_1 is at about $(1 - \mathrm{e}^{-\frac{1}{3}}) \approx 0.283$ of the response, and t_2 is at $1 - \mathrm{e}^{-1} \approx 0.632$ of the response. This renders the following solution for the dead time δ and the time constant T

$$T = \frac{3}{2}(t_2 - t_1) \tag{3.8}$$

$$\delta = t_2 - T \tag{3.9}$$

Approximating higher order systems with first order time delay functions

When the system is of higher order, but one time constant is by far the largest, then the system can be approximated as a first order system with a time delay (Seborg et al., 2004). According to Smith and Corripio (2006) the following rule of thumb can be used to approximate a higher order model into a first order model: *preserve the time constant of the highest value, and "add" the other time constants to the time delay*. This is the same as the first order Taylor series approximation given by Seborg et al. (2004) for δ as one of the lower time constants, as

$$\frac{1}{\delta s+1} \approx \mathrm{e}^{-\delta s}. \tag{3.10}$$

The thruster dynamics is significantly faster than the vessel motion, and this motivates a model structure of first order plus dead time systems (FOPDT) for the step tests that are performed. The delay can be used to estimate the time constant of the thruster dynamics.

3.3 Proposed identification models for the step tests

As mentioned in Section 3.2, the information that can be obtained in a step test is limited. The most advanced result that to some certainty can be extracted is a FOPDT approximation. This could allow for a second order model, where one of the time constants could be included in the delay. This is the approximation that will be used for all the step tests in the analysis, and the proposed models are discussed below.

The steady state gains are mentioned in the models, but will not be collected in the identification results. The responsiveness of the system is of interest, so the time constants and delay time are the interesting parameters to compare responsiveness of this thruster configuration with the retrofit.

In the Laplace-domain (Palm, 2009), let T(s), u(s), n(s), v(s), and r(s) represent thrust, surge speed, shaft speed of the thrusters, sway speed, and yaw rate $[^\circ/s]$, respectively. Let T_1, T_2, and so on, represent time constants. All the suggested models below will be identified identified by the FOPDT approximation of Section 3.2.1

3.3.1 Thrust and shaft speed time constants

For the thrust identification, two time constants are of interest. The time constant for the shaft speed, and the time constant for the obtained thrust force. The obtained thrust force is calculated from Eq. (2.25) from the measured shaft speed, since the thrust force is not measured. These two quantities will reach steady state at the same time, but have different time constants. This is due to the quadratic mapping between shaft speed and thrust force from Eq. (2.25).

By the discussion in Section 2.2 the dynamics from commanded thrust force to obtained shaft speed is of second order, that consists of a first order motor model, and first order shaft dynamics in cascade. The dynamics from commanded to obtained thrust force is also of second order since the mapping from shaft speed to thrust force is static. It is also proposed a first order model by Section 2.2.1, since real life experiments show that this approximation is satisfactory. In the following, a first order plus dead time approximation of Section 3.2.1 is applied, and that will capture both time constants of the second order model. If the delay and the time constant are added together, then this could approximate the time constant of the first order thruster model. The transfer function from commanded thrust, $T_c(s)$ to obtained shaft speed $n(s)$ is

$$\frac{n(s)}{T_c(s)} = \frac{K_p}{(1+T_1 s)(1+T_2 s)}, \tag{3.11}$$

and the first order plus dead time approximation is given as

$$\frac{n(s)}{T_c(s)} = \frac{K_p}{1+T_3 s} \mathrm{e}^{-\delta s}. \tag{3.12}$$

The models for thrust force are the same. The first order plus dead time approach will be used to find the time constant and the dead time of the thruster system.

3.3.2 Speed time constants

In the following let K_p, K_v, and K_r be steady state gains, δ a time delay, and T a time constant.

Proposed model for surge step tests

Using the decoupled surge dynamics of Eq. (2.8), and a first order thruster dynamics of Eq. (2.29), letting the thruster dynamics be the delay in a FOPDT approximation, the dynamics from commanded shaft speed $n(s)$ to obtained surge speed $u(s)$ can be written as

$$u(s) = \frac{K_p}{1+Ts}\mathrm{e}^{-\delta s}n(s) \tag{3.13}$$

where the model takes $n(s)$ as input and the surge speed $u(s)$ as output. The thruster dynamics is included as a delay. The delay can further be modelled using the first order Taylor series approximation of Eq. (3.10) as

$$\mathrm{e}^{-\delta s} \approx \frac{1}{(\delta s+1)}, \tag{3.14}$$

where δ is an estimate of the time constant of the thruster dynamics.

Proposed model for the sway step responses

The proposed model for the sway step tests is a model from commanded thrust (or commanded shaft speed), $T(s)$ to obtained sway speed $v(s)$. As discussed in Section 2.1.3 a first order model can be approximated. A delay time is added to model the response of the first order thruster dynamics (Section 2.2.1),

$$v(s) = \frac{K_v}{1+Ts}\mathrm{e}^{-\delta s}T(s). \tag{3.15}$$

Proposed model for the yaw step direction test responses

The proposed model for the yaw step tests are a model from commanded moment, W(s) [kNm] to obtained yaw rate, r [$^\circ/s$], and as above, by the discussion in Section 2.1.3 a first order model can be approximated, a delay time is added to model the first order thruster dynamics, such that the model becomes

$$r(s) = \frac{K_r}{1+Ts}\mathrm{e}^{-\delta s}W(s). \tag{3.16}$$

3.4 Uavailable data

Some data are unavailable from the sea trials, and it makes the data gathered in Section 3.5 incomplete. This section summarize what data that is lacking for thrust and power, and how this is handled.

3.4.1 Thrust data

Thruster mapping for the main thrusters

For the sea trials done in August, the calculated thrust force is gathered from the DP system. However, for the November sea trials, no thrust force estimates are available. Kongsberg Maritime have supplied their mapping (Schultz, 2013) for the thrusters at Gunnerus, and the mapping they use for the two main thruster is similar to Eq. (2.25), where $c = \rho K_T D^4$, and it is written as

$$T_a = cn^2, \tag{3.17}$$

where T_a is in $[kN]$, and n in rotations per second $[\frac{1}{s}]$, and c is a constant coefficient, that vary with the sign of the shaft speed. The value of c for bollard pull (Smogeli, 2006) and free run condition is shown in Table 3.1 (Schultz, 2013)

Table 3.1: KM thrustmapping

Bollard condition		
	$n > 0$	$n < 0$
c	6.6	-4.1
Free run condition		
	$n > 0$	$n < 0$
c	9.4	-6.4

Also, in order to have a good estimate of the thrust mapping in stationkeeping and DP maneuvers, the results of the pure DP logs from August has been back-calculated to find the mapping used. The measurement series of thrust force and shaft speed are used to find the constant coeffcient c for both positive and negative shaft speed, and the values found are included in Table 3.2. Note that the values are in between the bollard pull, and free run condition values.

Table 3.2: Back-calculated thrust mapping from

	$n > 0$	$n < 0$
c	8.13	-5.8

For the zero speed DP maneuvres completed in November, the mapping of Table 3.2 could have been applied to find an estimate of the thrust force for the two main propellers.

Unfortunately, MARINTEK only measure the absolute value of the shaft speed for November data, so the rotational direction of the shaft is unknown. From the pure DP manuevers performed in calm sea (August) in Section 3.5.3, often one propeller has positive rotation while the other has negative (see Table 3.11 and 3.12 where one thruster generate less thrust than the other. This is simply due to rotational direction, since they have about the

same rotational speed (magnitude)). Therefore, in order to have an estimate of the thrust force, a mean of the two c values will be used. So in the mapping from $n^2[rps^2]$ to thrust force $[kN]$ from Eq. (3.17) a value of

$$c = \frac{8.13 + 5.8}{2} = 6.97, \tag{3.18}$$

will be used. This gives a rough estimate of the thrust force. However, since the mapping does not take thrust losses into account, it is already quite rough. This mapping is used to find an estimate of the thrust force for the November sea trials for the DP 4 corner in Section 3.5.2, and for pure DP in Section 3.5.3.

Tunnel thruster

The thrust force for the tunnel thruster is available for the sea trials at calm sea (August), but not for the trials at sea in November. The shaft speed of the tunnel thruster is however logged in November, but Kongsberg did not have the mapping for this thruster since it is delivered by another vendor (Schultz, 2013), and the mapping for this thruster has not been obtained, unfortunately. The thrust mapping could have been back-calculated from August thrust data, but unfortunately, the shaft speed was not logged at that time.

3.4.2 Power data

For power consumption MARINTEK measured the shaft torque for the two main propellers, and found the power from Eq. (2.28). This is for both the sea trials. For the tunnel thruster the power consumption is not measured, and is therefore not available.

3.5 Identification results

For both the pure DP tests of Section 3.5.3, and the DP 4 corner of Section 3.5.2, the environmental conditions are logged for each maneuver. That is, wind speed and direction is found from a measurement series, and the size, and direction of the waves are manually read off just before the DP maneuver, and the values were collected from a weather buoy that MARINTEK logged. The ”DP current” is the value estimated by the DP system, and is read off the DP operator screen.

3.5.1 Thrust agility tests

As mentioned in Section 1.1.1, for the thrust agility tests a step in thrust force is applied for heading of $0°$, $45°$, $90°$, $135°$, $180°$, $-135°$, $-90°$, and $-45°$. This gives a plot of responsiveness of the thruster system. Due to lack of setpoint measurements, power feedback from MARINTEK is used to determine when the steps were applied.

For the agility plots the total response is considered. That is, the time constant found include the dead time, such that the total system response is plotted in the agility plots. That is, the time constant found is the time of 0.632 of the response (see Section 3.2).

Time constants from the tunnel thruster are highly inaccurate, because of low sampling (1 Hz). Both the start of the step, and the time where the response is at 0.632 of the response is quite uncertain. Still, the time constants found give an indication on the responsiveness of the tunnel thruster, so they are included.

Agility tests with no yawing moment applied

For no yawing moment, two thrust agility tests were performed. One where half of maximum available thrust was applied, and one where maximum thrust was applied. The environmental conditions for both these two tests were about equal. The wind speed and direction has been found from the DP data, and the current and waves were found before the tests were performed. The current is the DP current read from the DP system on board the vessel (the operator station).

The environmental conditions are found in Table 3.3, and the thrust time constants are found in Figure 3.1, and 3.2 for half and full thrust, respectively. On the radial axis time in seconds is plotted, and the time constant is shown for the two main thrusters (port and startboard), and the tunnel thruster. For direction $0°$, and $180°$ the tunnel thruster is not applicable.

Table 3.3: Environmental conditions thrust agility, no yawing moment

Environment	
Wind, speed	
Average	*Std.*
3.3	0.5
Wind, direction [°]	
Average	*Std.*
22.9	9.0
Waves	
H_s *[m]*	*Direction [°]*
0.1	South/SW
Current	
Speed [m/s]	*Direction [°]*
0.2	318

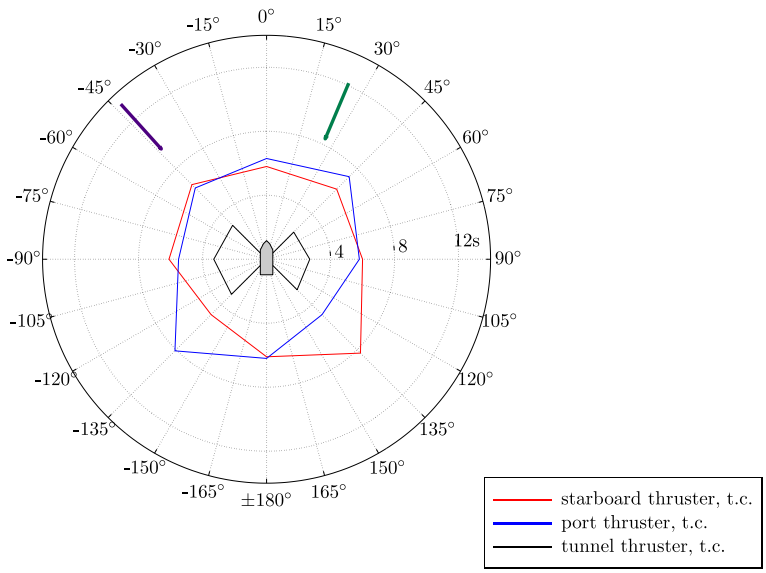

Figure 3.1: Agility plot, thrust time constant, no yawing moment - half thrust. Wind of $3.3\frac{m}{s}$ (green) and current of $0.2\frac{m}{s}$ (purple)

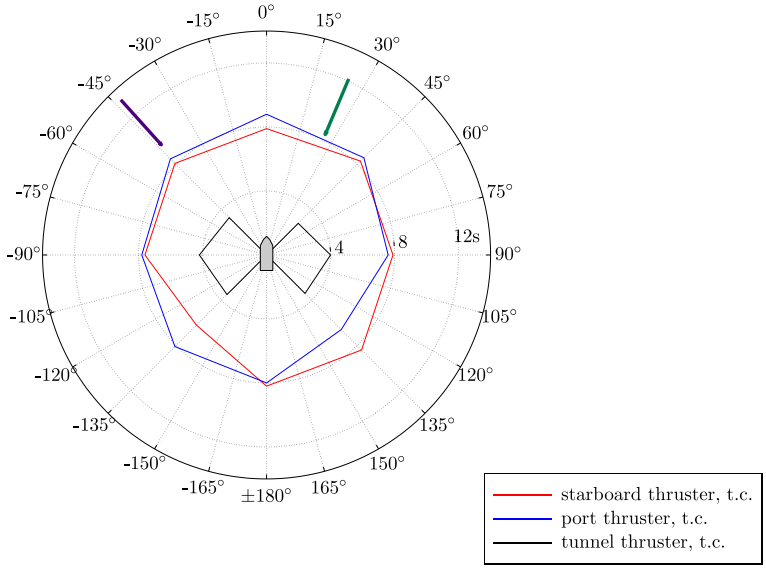

Figure 3.2: Agility plot, thrust time constant, no yawing moment - full thrust. Wind of $3.3\frac{m}{s}$ (green) and current of $0.2\frac{m}{s}$ (purple)

Agility test with applied yawing moment

A thrust agility tests was performed with an applied yawing moment of 100%. The thrust applied was 100% of available thrust force. The environmental conditions has been found similarly to Section 3.5.1, and is found in Table 3.4, and the thrust time constants are found in Figure 3.3.

Table 3.4: Environmental conditions thrust agility, with yawing moment

Environment	
Wind, speed	
Average	*Std.*
4.3	0.5
Wind, direction [°]	
Average	*Std.*
26.8	6.9
Waves	
H_s *[m]*	*Direction [°]*
0.1	S/SW
Current	
Speed [m/s]	*Direction [°]*
0.2	318

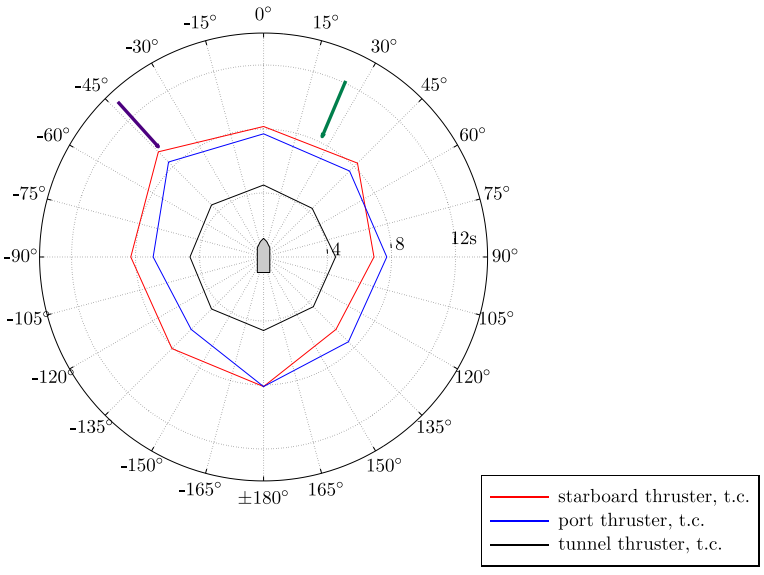

Figure 3.3: Agility plot - thrust time constant, with yawing moment. Wind of $4.3\frac{m}{s}$ (green) and current of $0.2\frac{m}{s}$ (purple)

3.5.2 DP 4 corner tests

In order to compare the existing thruster configuration with the retrofit, a maneuvre called DP 4 corner was performed. This is to compare responsiveness of the thrusters, position accuracy, thrust usage, and power consumption. This maneuvre is illustrated in Figure 3.4, and it consists of four parts:

- 1. Ahead, heading same: From DP steady state with heading north, change desired position 50 m ahead, keeping same heading,
- 2. Crab port, heading same: At the instant the vessel reach the operating circle of the new setpoint, position setpoint is changed to 50 m port (west) of the vessel,
- 3. Astern, heading change: At the instant the vessel reach the operating circle of the new setpoint, the new desired setpoint is 50m eastern (south) and heading set to -90° (west),
- 4. Astern, heading same: AS the instant the vessel reach the operating circle of the new setpoint, new setpoint is set to be 50 m astern (east, back to original position), with heading still -90° (west).

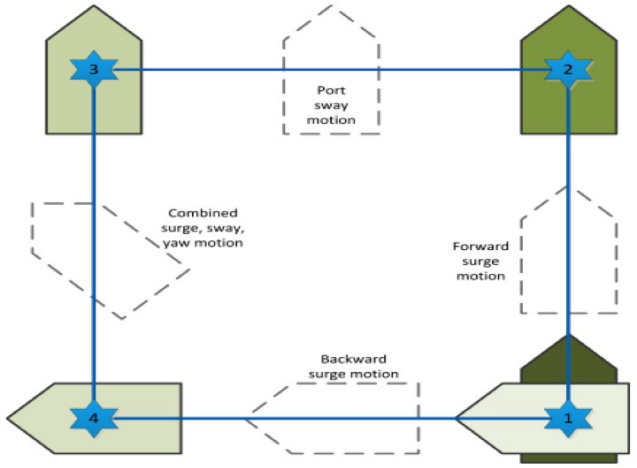

Figure 3.4: DP 4 corner, illustration

DP 4 corner - calm sea

During the sea trials in calm sea (August) one DP 4 corner was performed. The log from the DP system is available, but MARINTEK's log contains only half of the maneuver. The DP data is used to find the duration. The setpoints in position error are available, so the duration estimates are quite accurate. However, a lot of measurements are unavailable for the first half of the maneuver. Even though the DP system logged shaft speed, and thrust force for the sea trials in August, these values were collected by MARINTEK as the trial

was ongoing. Because of this, thrust force for the first half of this maneuver is unavailable, but power consumption is available for the entire maneuver, since this was collected from the DP system log. See Table 3.5 for the environmental conditions, and Table 3.6 for the thrust and power consumption.

Table 3.5: DP 4 corner - environmental conditions,calm sea - 3035

Environment	
Wind, speed [m/s]	
Average	*Std.*
5.3	0.3
Wind, direction [°]	
Average	*Std.*
42.2	2.2
Waves	
H_s *[m]*	*Direction [°]*
0.2	N
Current	
Speed [m/s]	*Direction [°]*
0.3	147

Table 3.6: DP 4 corner maneuver - calm sea

Maneuvre	**Duration [s]**	**Accumulated thrust force [kNs]**				**Accumulated power [kJ]**			
		SB	*Port*	*Tunnel*	*Total*	*SB*	*Port*	*Tunnel*	*Total*
Ahead, heading same	134	—	—	—	—	690	600	—	1290
Crab port, heading same	214	—	—	—	—	4750	4380	—	9130
Astern, heading change	142	770	1230	1080	3080	3230	4520	—	7750
Astern, heading same	134	600	1100	960	2660	3620	3790	—	7410
Total	624	—	—	—	—	12290	13290	—	25580

DP 4 corner - at sea

Two DP 4 corner tests were performed in the November sea trials, and only MARINTEK logged (no logs from the DP system itself). MARINTEK performed extensive logs containing quite good North and East position measurements, shaft speed measurements of all thrusters, and a calculated power consumption of the two main thrusters. Setpoints are therefore unavailable, but in order to find the duration of each maneuver, the north-east plot is used in combination with the plots of north position, east position and heading. The duration is not very accurate, but should be correct to within some seconds of margin.

The N-E plot of the first test is shown in Figure 3.5. Note that in the last part of the maneuver there is an overshoot in east-position before the vessel returns to desired east position. For the logs in Table 3.7, and 3.8, the duration is stopped when the correct east

value is reached the first time (neglecting the overshoot), to get a better estimate of the power consumption as if there were no overshoot. It should also be noted that the vessel does not perfectly track the square as it was supposed to do.

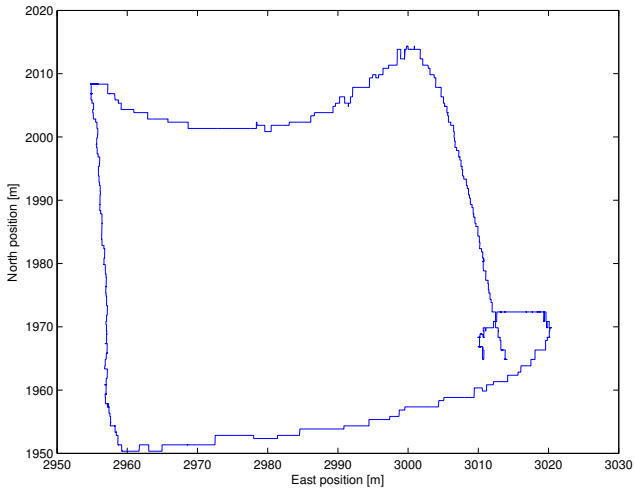

Figure 3.5: NE-plot of DP 4 corner test 1, at sea

Table 3.7: DP 4 corner - environmental conditions, at sea - test 1

Environment	
Wind, speed [m/s]	
Average	*Std.*
2.9	0.5
Wind, direction [°]	
Average	*Std.*
178.0	7.5
Waves	
H_s *[m]*	*Direction [°]*
1.5	345
Current	
Speed [m/s]	*Direction [°]*
0.2	N/NW

Table 3.8: DP 4 corner - maneuver, at sea - test 1

Maneuvre	**Duration [s]**	**Accumulated thrust force [kNs]**				**Accumulated power [kJ]**			
		SB	*Port*	*Tunnel*	*Total*	*SB*	*Port*	*Tunnel*	*Total*
Ahead, heading same	117	310	290	—	600	630	410	—	1040
Crab port, heading same	180	1430	1910	—	3340	4960	6720	—	11680
Astern, heading change	163	530	570	—	1100	1510	1190	—	2700
Astern, heading same	85	1850	2270	—	4120	8770	12630	—	21400
Total	545	4120	5040	—	9160	15870	20950	—	36820

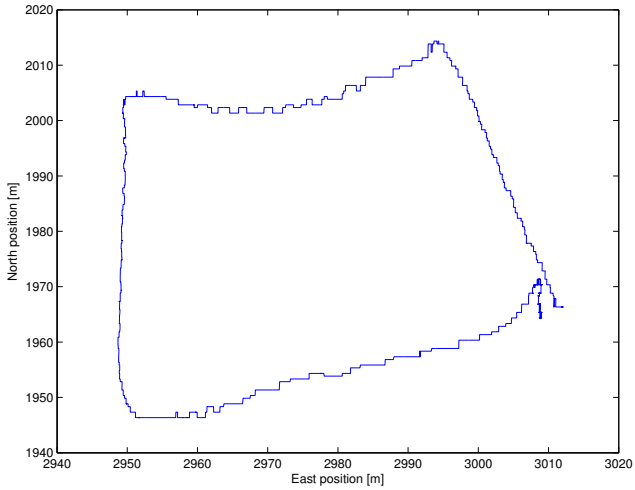

Figure 3.6: NE-plot of DP 4 corner test 2, at sea

Table 3.9: DP 4 corner - environmental conditions, at sea - test 2

Environment	
Wind, speed [m/s	
Average	*Std.*
2.8	0.4
Wind, direction [°]	
Average	*Std.*
174.3	6.8
Waves	
H_s *[m]*	*Direction [°]*
1.5	345
Current	
Speed [m/s]	*Direction [°]*
0.4	N/NW

Table 3.10: DP 4 corner - maneuver, at sea - test 2

Maneuvre	Duration [s]	Accumulated thrust force [kNs]				Accumulated power [kJ]			
		SB	*Port*	*Tunnel*	*Total*	*SB*	*Port*	*Tunnel*	*Total*
Ahead, heading same	101	310	370	—	680	660	850	—	1510
Crab port, heading same	207	1050	1300	—	2350	3500	3670	—	7170
Astern, heading change	120	640	460	—	1100	1800	900	—	2700
Astern, heading same	118	2890	3240	—	6130	13820	18600	—	32420
Total	546	4890	5370	—	10260	19780	24020	—	43800

3.5.3 Pure DP tests

For the pure DP tests, the vessel is simply trying to maintain position for a five minute interval. There were three tests performed in calm water (in August), and nine tests at sea, with different heading. In August these tests were performed right before other maneuvers, such as the DP 4 corner maneuver of Section 3.5.2. For the pure DP maneuvers performed in at sea, the table names indicate a heading of the vessel. This heading name is the observed (by the operator) heading relative to the mean environmental forces, and therefore it might deviate from the direction of the environmental forces reported in the table.

The tests are performed at slightly varying environmental conditions. The intention of the logging of the thrust, and power usage is to perform the same maneuver after the retrofit, and compare.

The thrust force in the tables below is T_a, the delivered thrust (see Section 2.2). This is why two average thrust values can be different when power consumption is about the same; the propellers rotate in opposite directions, and forward is optimal.

Results - calm sea

For the test in August, the North and East measurements are sampled too low, and give a poor estimate of the standard deviation in the position error. The heading measurements on the other hand, are useful, and give a indication of DP performance.

Table 3.11: Pure DP, calm sea - test 1

Environment			***DP system performance***		
Wind, speed [m/s]			**Position acc. (Std.) [m]**		
Average	*Std.*		*North*	*East*	
2.6	0.4		—	—	
Wind, direction [°]			**Heading**		
Average	*Std.*		*Average [°]*	*Std [°]*	
18 .0	4.6		62.1	0.4	
Waves			**Average thruster force [kN]**		
H_s *[m]*	*Direction [°]*		*SB thruster*	*Port thruster*	*Tunnel thruster*
negligible	—		5.5	3.9	2.7
Current			**Total average**: 12.1 kN		
Speed [m/s]	*Direction [°]*		**Accumulated power [kJ]**		
0.3	325 (during)-334(after)		*SB thruster*	*Port thruster*	*Tunnel thruster*
			2860	3500	—
			Total acc. power:: 6360 kJ (ex. tunnel thr.)		

Table 3.12: Pure DP, calm sea - test 2

Environment			***DP system performance***		
Wind, speed [m/s]			**Position acc. (Std.) [m]**		
Average	*Std.*		*North*	*East*	
2.2	0.4		—	—	
Wind, direction [°]			**Heading**		
Average	*Std.*		*Average [°]*	*Std [°]*	
3.3	9.4		130.2	0.4	
Waves			**Average thruster force [kN]**		
H_s *[m]*	*Direction [°]*		*SB thruster*	*Port thruster*	*Tunnel thruster*
small ripples	—		4.0	5.5	2.9
Current			**Total average**: 12.4 kN		
Speed [m/s]	*Direction [°]*		**Accumulated power [kJ]**		
0.2	223 (before)-241 (after)		*SB thruster*	*Port thruster*	*Tunnel thruster*
			3100	3280	—
			Total acc. power:: 6380 kJ (ex. tunnel thr.)		

Table 3.13: Pure DP, calm sea - test 3

Environment			***DP system performance***		
Wind, speed [m/s]			**Position acc. (Std.) [m]**		
Average	*Std.*		*North*	*East*	
3.9	0.3		—	—	
Wind, direction [°]			**Heading**		
Average	*Std.*		*Average [°]*	*Std [°]*	
43.8	2.6		358.8	0.79	
Waves			**Average thruster force [kN]**		
H_s *[m]*	*Direction [°]*		*SB thruster*	*Port thruster*	*Tunnel thruster*
0.2	North		0.67	0.65	0.53
Current			**Total average**: 1.85 kN		
Speed [m/s]	*Direction [°]*		**Accumulated power [kJ]**		
0.1	235		*SB thruster*	*Port thruster*	*Tunnel thruster*
			129	545	—
			Total acc. power:: 674 kJ (ex. tunnel thr.)		

Results - at sea

For the November sea trials the position measurements are better, and they are therefore included in the table. As mentioned in Section 3.4.1, the thrust force is not available for these sea trials, and the thrust mapping of Section 3.4.1 is used to find the thrust force estimate.

Table 3.14: Pure DP, at sea - test 1, relative heading 0 degrees

Environment			***DP system performance***		
Wind, speed [m/s]			**Position acc. (Std.) [m]**		
Average	*Std.*		*North*	*East*	
5.2	1.1		0.8	0.6	
Wind, direction [°]			**Heading**		
Average	*Std.*		*Average [°]*	*Std [°]*	
79.1	7.7		336.1	0.8	
Waves			**Average thruster force [kN]**		
H_s *[m]*	*Direction [°]*		*SB thruster*	*Port thruster*	*Tunnel thruster*
2.1	N-NW		1.2	1.0	—
Current (meas. by Kongsberg)			**Total average**: 2.2 kN		
Speed [m/s]	*Direction [°]*		**Accumulated power [kJ]**		
0.4	—		*SB thruster*	*Port thruster*	*Tunnel thruster*
			860	413	—
			Total acc. power:: 1273 kJ (ex. tunnel thr.)		

Table 3.15: Pure DP, at sea - test 2, relative heading 90 degrees

Environment			***DP system performance***		
Wind, speed [m/s]			**Position acc. (Std.) [m]**		
Average	*Std.*		*North*	*East*	
3.3	0.5		0.6	0.9	
Wind, direction [°]			**Heading**		
Average	*Std.*		*Average [°]*	*Std [°]*	
72.5	13.9		65.5	0.8	
Waves			**Average thruster force [kN]**		
H_s *[m]*	*Direction [°]*		*SB thruster*	*Port thruster*	*Tunnel thruster*
2.3	340		4.3	3.9	—
Current (meas. by Kongsberg)			**Total average**: 8.2 kN (ex. tunnel thr.)		
Speed [m/s]	*Direction [°]*		**Accumulated power [kJ]**		
0.3	98		*SB thruster*	*Port thruster*	*Tunnel thruster*
			3660	3590	—
			Total acc. power:: 7250 kJ (ex. tunnel thr.)		

Table 3.16: Pure DP, at sea - test 3, relative heading 0 degrees

Environment			***DP system performance***		
Wind, speed [m/s]			**Position acc. (Std.) [m]**		
Average	*Std.*		*North*	*East*	
4.2	0.6		0.7	0.3	
Wind, direction [°]			**Heading**		
Average	*Std.*		*Average [°]*	*Std [°]*	
190.8	7.5		11.0	0.78	
Waves			**Average thruster force [kN]**		
H_s *[m]*	*Direction [°]*		*SB thruster*	*Port thruster*	*Tunnel thruster*
1.7	14		5.0	5.6	—
Current (meas. by Kongsberg)			**Total average**: 10.6 kN (ex. tunnel thr.)		
Speed [m/s]	*Direction [°]*		**Accumulated power [kJ]**		
0.36	336		*SB thruster*	*Port thruster*	*Tunnel thruster*
			3660	3590	—
			Total acc. power:: 7250 kJ (ex. tunnel thr.)		

Table 3.17: Pure DP, at sea - test 4, relative heading 90 degrees

Environment			***DP system performance***		
Wind, speed [m/s]			**Position acc. (Std.) [m]**		
Average	*Std.*		*North*	*East*	
4.3	1.0		0.5	0.5	
Wind, direction [°]			**Heading**		
Average	*Std.*		*Average [°]*	*Std [°]*	
204.8	5.6		101.7	0.9	
Waves			**Average thruster force [kN]**		
H_s *[m]*	*Direction [°]*		*SB thruster*	*Port thruster*	*Tunnel thruster*
1.7	14		1.4	2.0	—
Current			**Total average**: 3.4 kN (ex. tunnel thr.)		
Speed [m/s]	*Direction [°]*		**Accumulated power [kJ]**		
0.2	247		*SB thruster*	*Port thruster*	*Tunnel thruster*
			1060	1240	—
			Total acc. power:: 2300 kJ (ex. tunnel thr.)		

Table 3.18: Pure DP, at sea - test 5, relative heading 45 degrees

Environment			***DP system performance***		
Wind, speed [m/s]			**Position acc. (Std.) [m]**		
Average	*Std.*		*North*	*East*	
4.2	0.5		0.5	0.4	
Wind, direction [°]			**Heading**		
Average	*Std.*		*Average [°]*	*Std [°]*	
215.3	14.0		55.3	0.7	
Waves			**Average thruster force [kN]**		
H_s *[m]*	*Direction [°]*		*SB thruster*	*Port thruster*	*Tunnel thruster*
1.7	14		2.8	2.4	—
Current			**Total average**: 5.2 kN (ex. tunnel thr.)		
Speed [m/s]	*Direction [°]*		**Accumulated power [kJ] over 5 min**		
0.25	300		*SB thruster*	*Port thruster*	*Tunnel thruster*
			2020	1090	—
			Total acc. power:: 3110 kJ (ex. tunnel thr.)		

Table 3.19: Pure DP, at sea - test 6, relative heading 135 degrees

Environment			***DP system performance***		
Wind, speed [m/s]			**Position acc. (Std.) [m]**		
Average	*Std.*		*North*	*East*	
4.7	0.7		0.5	0.4	
Wind, direction [°]			**Heading**		
Average	*Std.*		*Average [°]*	*Std [°]*	
210.3	7.1		146.0	0.8	
Waves			**Average thruster force [kN]**		
H_s *[m]*	*Direction [°]*		*SB thruster*	*Port thruster*	*Tunnel thruster*
1.7	14		5.5	5.6	—
Current			**Total average**: 11.1 kN (ex. tunnel thr.)		
Speed [m/s]	*Direction [°]*		**Accumulated power [kJ]**		
0.3	191		*SB thruster*	*Port thruster*	*Tunnel thruster*
			5480	5560	—
			Total acc. power:: 11040 kJ (ex. tunnel thr.)		

Table 3.20: Pure DP, at sea - test 7, relative heading 180 degrees

Environment			***DP system performance***		
Wind, speed [m/s]			**Position acc. (Std.) [m]**		
Average	*Std.*		*North*	*East*	
4.1	0.5		0.6	0.3	
Wind, direction [°]			**Heading**		
Average	*Std.*		*Average [°]*	*Std [°]*	
212.3	9.0		190.1	0.7	
Waves			**Average thruster force [kN]**		
H_s *[m]*	*Direction [°]*		*SB thruster*	*Port thruster*	*Tunnel thruster*
1.7	14		2.0	1.6	—
Current			**Total average**: 3.6 kN (ex. tunnel thr.)		
Speed [m/s]	*Direction [°]*		**Accumulated power [kJ]**		
0.21	231		*SB thruster*	*Port thruster*	*Tunnel thruster*
			1220	810	—
			Total acc. power:: 2030 kJ (ex. tunnel thr.)		

Table 3.21: Pure DP, at sea - test 8, relative heading 0 degrees

Environment			***DP system performance***		
Wind, speed [m/s]			**Position acc. (Std.) [m]**		
Average	*Std.*		*North*	*East*	
6.9	0.6		0.7	0.8	
Wind, direction [°]			**Heading**		
Average	*Std.*		*Average [°]*	*Std [°]*	
166.0	8.1		241.7	0.7	
Waves			**Average thruster force [kN]**		
H_s *[m]*	*Direction [°]*		*SB thruster*	*Port thruster*	*Tunnel thruster*
1.9	West		1.1	1.5	—
Current			**Total average**: 2.5 kN (ex. tunnel thr.)		
Speed [m/s]	*Direction [°]*		**Accumulated power [kJ]**		
0.5	240		*SB thruster*	*Port thruster*	*Tunnel thruster*
			790	590	—
			Total acc. power:: 1380 kJ (ex. tunnel thr.)		

Table 3.22: Pure DP, at sea - test 9, relative heading -90 degrees

Environment			***DP system performance***		
Wind, speed [m/s]			**Position acc. (Std.) [m]**		
Average	*Std.*		*North*	*East*	
6.9	0.7		0.8	0.9	
Wind, direction [°]			**Heading**		
Average	*Std.*		*Average [°]*	*Std [°]*	
167.6	7.3		150.4	2.8	
Waves			**Average thruster force [kN]**		
H_s *[m]*	*Direction [°]*		*SB thruster*	*Port thruster*	*Tunnel thruster*
1.85	West		23.3	21.2	—
Current			**Total average**: 44.5 kN (ex. tunnel thr.)		
Speed [m/s]	*Direction [°]*		**Accumulated power [kJ]**		
0.6	200		*SB thruster*	*Port thruster*	*Tunnel thruster*
			29620	28140	—
			Total acc. power:: 57760 kJ (ex. tunnel thr.)		

3.5.4 Step tests

There were several step tests performed, all at the calm water sea trials in August. One intention is to find the responsiveness of the thrusters. That is, the time constant for the shaft speed, and for the thrust force. Also, the goal is to find the time constants for the vessel response in surge, sway, and yaw. The shaft speed and thrust time constants are found for surge and sway. The tunnel thruster response is not included in this analysis since the values for the tunnel thruster are of low sampling rate, and it is difficult to determine

when steps are applied. In the agility plots of Section (3.5.1) the tunnel thruster response (including dead time) is plotted, and it can be verified that it is faster than the main propellers. Therefore, the response of the main propellers has the highest time constant, and the response of the tunnel thruster is not of great interest.

For the surge and sway step tests the proposed model of Eq. (3.12) is applied to find the shaft speed time constant and dead time, and also the thrust force time constant and dead time.

For surge, the proposed model of Eq. (3.13) from commanded thrust (or shaft speed) to surge speed is applied for the speed time constants and delay time. The same approach is used for the sway speed time constant, by using the model of Eq. (3.15). For the yaw step tests, time constants and delays are found for the yaw rate according to Eq. (3.16). Also, the rudder time constants are found according to the FOPDT approach of Section 3.2.1.

For all the tables below, the time constant is represented by T, and T_n is the time constant for the shaft speed, and T_{thrust} is the time constant for the thrust. Similarly is δ a time delay (or dead time), and δ_n is the delay for shaft speed, and δ_{thrust} is the delay for thrust. For the rudder time constants, T_{sb} and T_{port} represent the time constants for starboard and port rudder, respectively. Similarly for the delays δ_{sb} and δ_{port}.

About how tests are read

For all the step tests no setpoints are available. To figure out when steps are applied, the curves for power feedback is applied, since power responds quickly. In the cases where the power curve is unclear the shaft speed feedback curve is used.

Surge step tests

Several step tests in surge were performed for both forward and backward speed. For forward speed the step tests were run for a step in thrust magnitude [%] of $0-5\%$, $5-10\%$, $10-15\%$, $15-25\%$, $25-40\%$, $40-0\%$, $0-80\%$ and $80-0\%$. Figure 3.7 and 3.8 show the surge velocity, shaft speed feedback, and power feedback for the forward speed step tests. Table 3.23 present the time constant and delay time for the shaft speed and thrust feedback, whereas Table 3.24 show the speed time constant and delay. Some of the step tests results are omitted, due to uncertainty, or for the case of $40-0\%$, and $80-0\%$ they are not included since they did not reach steady state before the tests were finished.

For backward speed the step tests were run for a step in thrust magnitude [%] of $0-5\%$, $5-10\%$, $10-15\%$, $15-20\%$, $20-0\%$, $0-40\%$, and $40-0\%$. Figure 3.9 and 3.10 show the surge velocity, shaft speed feedback, and power feedback for the backward speed step tests. Table 3.25 present the time constant and delay time for the shaft speed and thrust feedback, whereas Table 3.26 show the speed time constant and delay. As with the forward speed test results, the tests with poor data is not included in the tables.

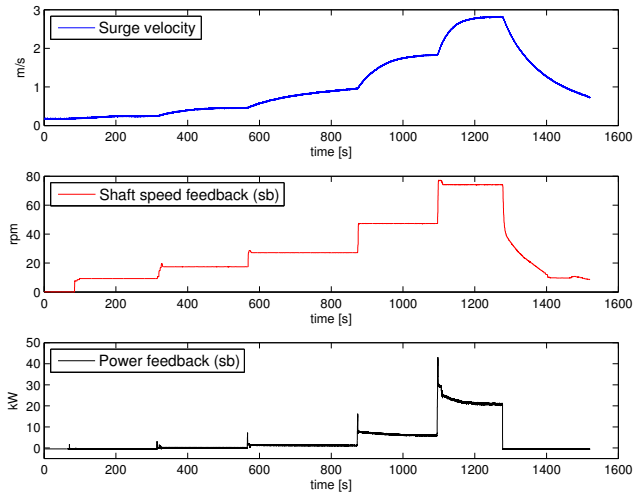

Figure 3.7: Step test in surge - forward velocity. Surge velocity (top, blue), shaft speed feedback for starboard thruster (red), and power feedback for starboard thruster (black). Power and shaft speed feedback is used to indicate when the input is applied. The steps shown in the figure are test number 0-5,5-10,10-15,15-25, 25-40, and 40-0 (ref. Table (ref. Table 3.23, and 3.24).

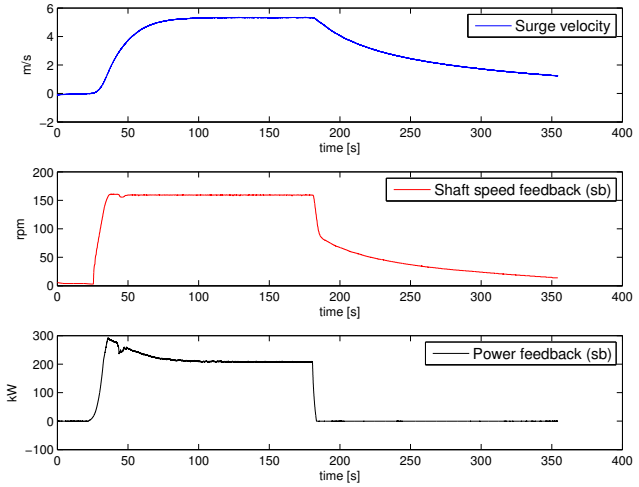

Figure 3.8: Step test in surge - forward velocity. Surge velocity (top, blue), shaft speed feedback for starboard thruster (red), and power feedback for starboard thruster (black). Power and shaft speed feedback is used to indicate when the input is applied. The step shown in the figure is for 0-80 (ref. Table 3.23, and 3.24).

Table 3.23: Surge step tests, forward speed - thrust and shaft speed time constants

Step mag. [%]	$T_n[s]$	$\delta_n[s]$	$T_{thrust}[s]$	$\delta_{thrust}[s]$
0-80	5.5	2.9	4.7	5.6
25-40	1.1	2.0	2.2	1.5
15-25	1.0	1.9	1.4	1.8
10-15	1.4	11.6	0.3	12.7

Table 3.24: Surge step tests, forward speed - speed time constants

Step mag. [%]	$T[s]$	$\delta[s]$
0-80	16.4	8.5
25-40	34.2	1.4
15-25	59.2	1.8
10-15	135.0	7.2
5-10	63.3	5.0
0-5	65.5	6.0

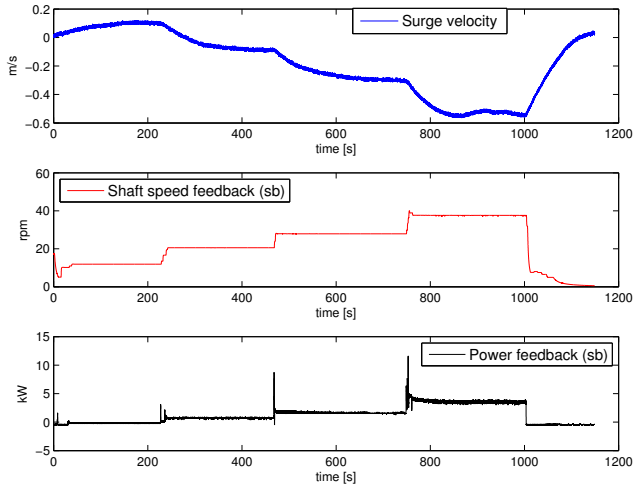

Figure 3.9: Step test in surge - backward velocity. Surge velocity (top, blue), shaft speed feedback for starboard thruster (red), and power feedback for starboard thruster (black). Power and shaft speed feedback is used to indicate when the input is applied. The steps shown in the figure are test number 0-5,5-10,10-15,15-20, and 20-0 (ref. Table Table 3.25, and 3.26).

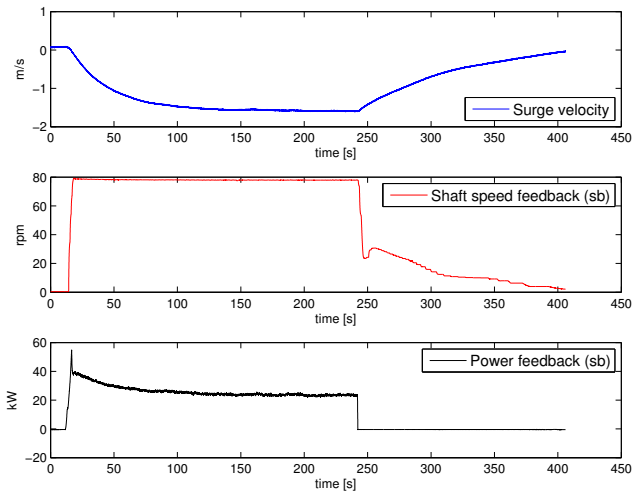

Figure 3.10: Step test in surge - backward velocity. Surge velocity (top, blue), shaft speed feedback for starboard thruster (red), and power feedback for starboard thruster (black). Power and shaft speed feedback is used to indicate when the input is applied. The step shown in the figure is for 0-40 (ref. Table 3.25, and 3.26).

Table 3.25: Surge step tests, backward speed - thrust and shaft speed time constants

Step mag. $[\%]$	$T_n[s]$	$\delta_n[s]$	$T_{thrust}[s]$	$\delta_{thrust}[s]$
0-40	1.6	2.7	1.6	3.4
15-20	4.4	1.2	4.4	1.3
10-15	2.6	4.3	0.6	6.4
5-10	0.5	5.4	0.8	5.3
20-0	2.7	2.3	1.2	2.4

Table 3.26: Surge step tests, backward speed - speed time constants

Step mag. $[\%]$	$T[s]$	$\delta[s]$
0-40	30.7	3.1
15-20	36.6	5.5
10-15	76.6	0.6
5-10	64.6	1.4
20-0	51.4	9.0

Sway step tests

For the sway step tests, step tests were performed for starboard and port side. For the starboard tests steps of thrust magnitude of $[\%]$ of $0-25\%$, $0-50\%$, $0-75\%$, $0-$

100% and $100 - 0\%$ were run. For port side, all the same tests except $0 - 75\%$ were performed.

As seen from Figure 3.11 and 3.13 the surge velocity is considerable for the step tests. This is probably because of the thruster configuration. The vessel has one tunnel thruster, and two propellers in the stern, and the vessel needs a certain surge velocity to have full flexibility to move in sway. If only the tunnel thruster is used it would induce a moment that have to be counteracted by the stern propellers.

Due to the high surge velocity the total speed is used. That is,

$$\sqrt{v^2 + u^2}, \tag{3.19}$$

where u and v are the surge and sway velocity, respectively. The plots for total speed, shown in Figure 3.11 and 3.13 indicate a clearer step response shape, but for some of the step tests, it does not seem like steady state is reached. The values found are therefore of lower quality. The values reported for starboard are found in Table 3.27 for the thrust, and shaft speed time constants, and in Table 3.28 for the speed time constants. For the port step response the values are found in Table 3.29 for the thrust time constants, and in Table 3.30 for the speed time constants.

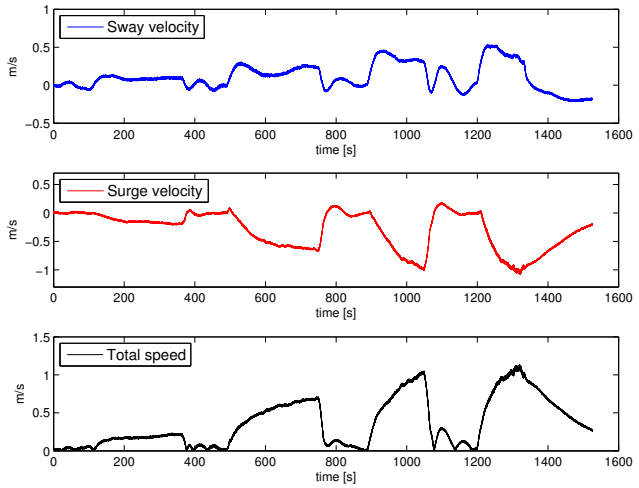

Figure 3.11: Step test in sway - starboard. Sway velocity (top, blue), surge velocity (red), and total speed (black). The steps shown in the figure are test number 0-25,0-50,0-75,0-100, and 100-0 of (ref. Table 3.27, and 3.28).

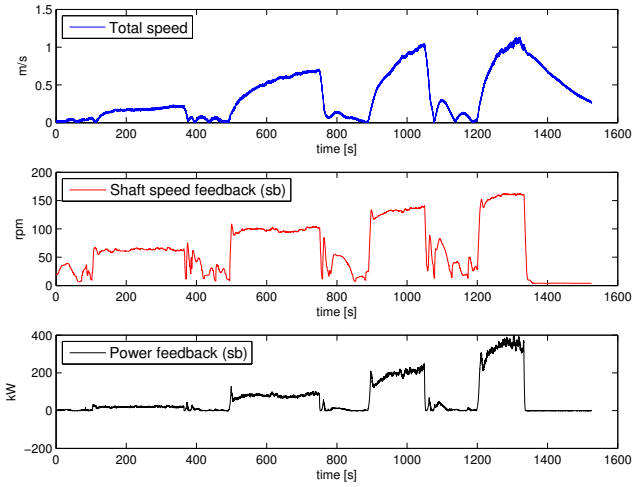

Figure 3.12: Step test in sway - starboard. Total speed (top, blue), shaft speed feedback for starboard thruster (red), and power feedback for starboard thruster (black). Power and shaft speed feedback is used to indicate when the input is applied. The steps shown in the figure are test number 0-25,0-50,0-75,0-100 (ref. Table 3.27, and 3.28).

Table 3.27: Sway step tests, starboard speed - thrust and shaft speed time constants for sb thruster

Step mag. [%]	$T_n[s]$	$\delta_n[s]$	$T_{thrust}[s]$	$\delta_{thrust}[s]$
0-100	4.7	3.3	4.4	4.9
0-75	3.9	2.7	3.5	4.1
0-50	2.5	3.0	2.5	3.8
0-25	2.1	1.2	1.2	2.7
100-0	4.2	1.6	2.8	1.1

Table 3.28: Sway step tests, main propellers, starboard - speed time constants

Step mag. [%]	$T[s]$	$\delta[s]$
0-100	10.7	2.7
0-75	12.5	2.6
0-50	15.6	1.1
0-25	14.4	4.0

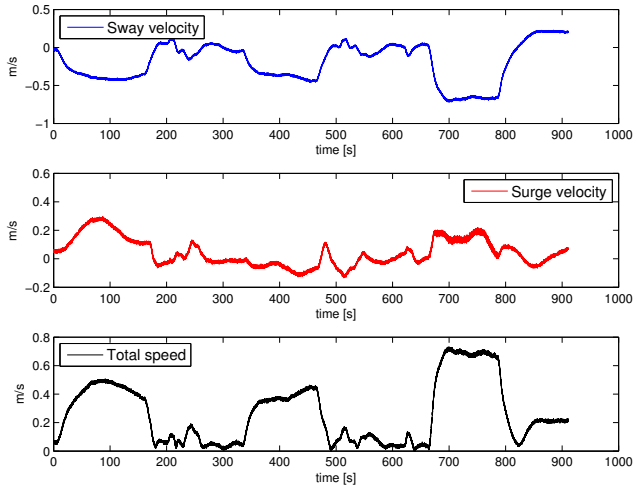

Figure 3.13: Step test in sway - port. Sway velocity (top, blue), surge velocity (red), and total speed (black). The steps shown in the figure are test number 0-25,0-50,0-100 (ref. Table 3.29, and 3.30).

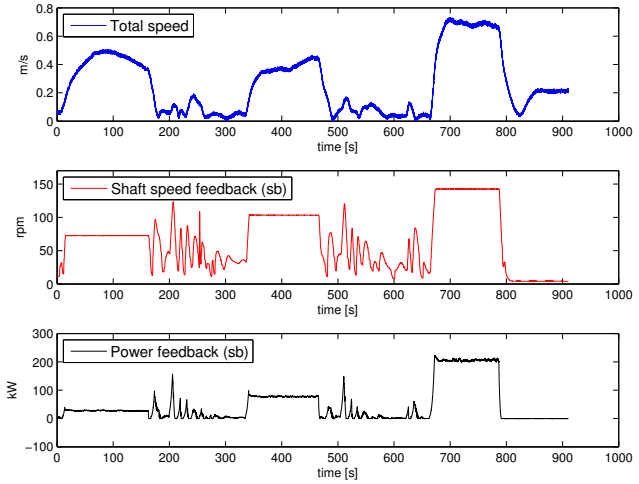

Figure 3.14: Step test in sway - port. Total speed (top, blue), shaft speed feedback for starboard thruster (red), and power feedback for starboard thruster (black). Power and shaft speed feedback is used to indicate when the input is applied. The steps shown in the figure are test number 0-25,0-50,0-100 (ref. Table 3.29, and 3.30).

Table 3.29: Sway port step tests - thrust and shaft speed time constants for port thruster

Step mag. [%]	$T_n[s]$	$\delta_n[s]$	$T_{thrust}[s]$	$\delta_{thrust}[s]$
0-100	4.5	2.9	4.0	5.0
0-50	2.4	2.9	2.7	3.2
0-25	1.0	3.4	1.1	3.4
100-0	4.2	1.5	2.7	1.0

Table 3.30: Sway step tests, main propellers, port - time constant

Step mag. [%]	$T[s]$	$\delta[s]$
0-100	9.0	2.5
0-50	12.8	1.3
0-25	18.8	1.0

Yaw step tests

Four yaw step tests were performed. Two where the vessel turned starboard (at speeds of 3 knots, and 6 knots), and two where the vessel turned port (at speeds of 3 knots, and 6 knots). For all the yaw step tests both the rudder angles are first stepped to 20 degrees, and then the rudders are stepped to their maximum angle (about 47 degrees). Notice for instance from Figure 3.15 that the step in rudder angle from 20 to 47 degrees gives an initial pulse in yaw rate, but does not significantly change the steady state yaw rate value. The yaw rate time constant found in Table 3.31 is for the step response from 0 to 20 degrees rudder angle, and for Table 3.32 for 47 to 0 degrees rudder angle. For the step from 20 to 47 degrees a time constant is not found since the response is so unclear and does not resemble a normal step response. The rudder angle change is used to indicate when a step is applied. All the steady state yaw rates oscillate after the new value is reached, and the steady state value is chosen as the observed mean value of this oscillation.

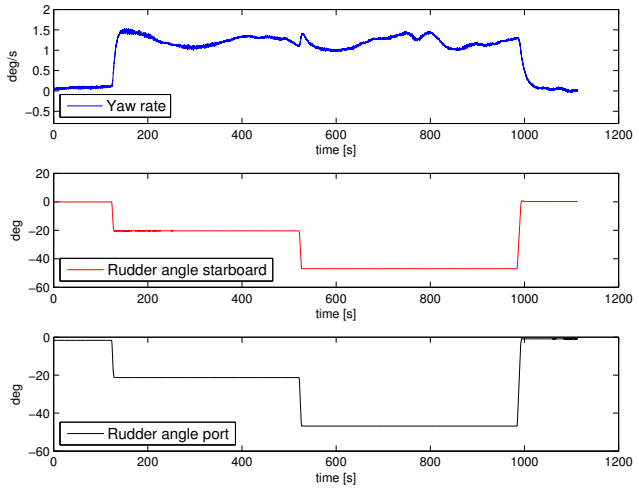

Figure 3.15: Step test in yaw - starboard at 3kn. Yaw rate (top, blue), rudder angle starboard (red), and rudder angle port (black). The steps shown in the figure are for rudder angle steps of 0-50 (ref. Table), 50-100, and 100-0 (ref. Table 3.31, 3.32, and 3.33).

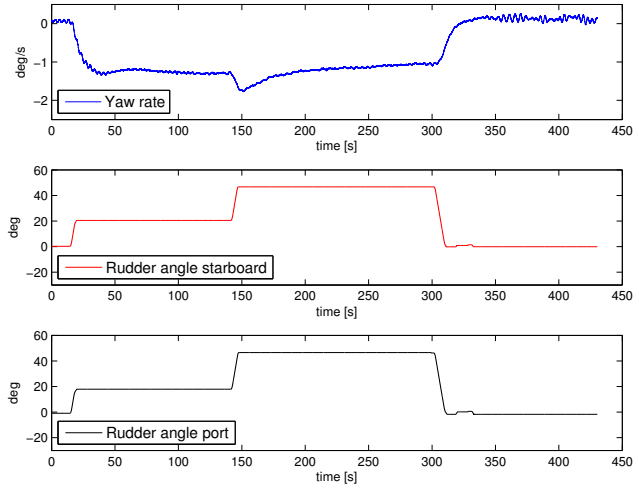

Figure 3.16: Step test in yaw - port at 3kn. Yaw rate (top, blue), rudder angle starboard (red), and rudder angle port (black). The steps shown in the figure are for rudder angle steps of 0-50 (ref. Table), 50-100, and 100-0 (ref. Table 3.31, 3.32, and 3.34).

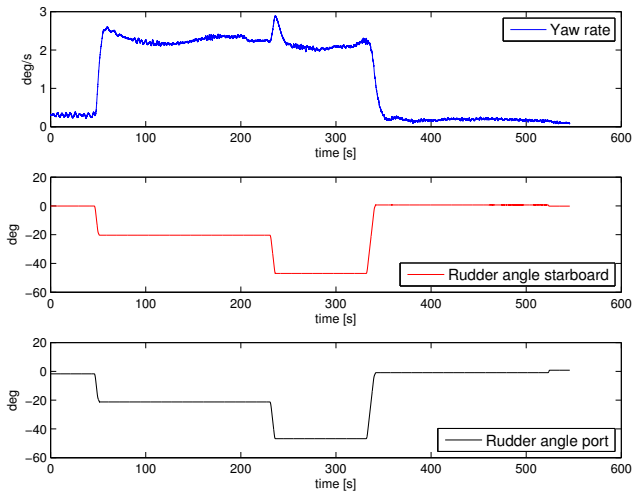

Figure 3.17: Step test in yaw - startboard at 6kn. Yaw rate (top, blue), rudder angle starboard (red), and rudder angle port (black). The steps shown in the figure are for rudder angle steps of 0-50, 50-100, and 100-0 (ref. Table 3.31, 3.32, and 3.35).

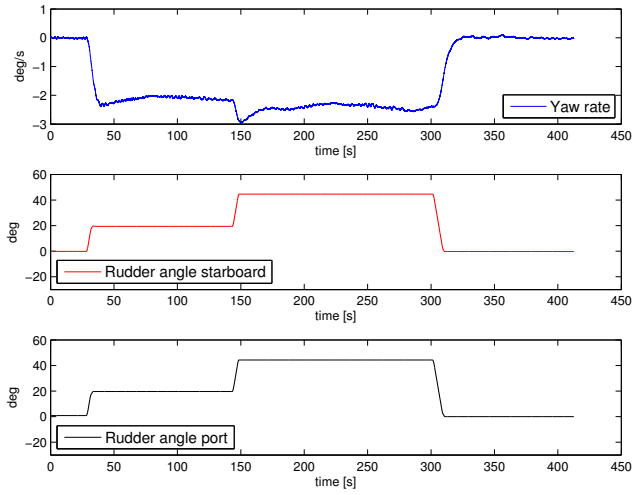

Figure 3.18: Step test in yaw - port at 6kn. Yaw rate (top, blue), rudder angle starboard (red), and rudder angle port (black). The steps shown in the figure are for rudder angle steps of 0-50, 50-100, and 100-0 (ref. Table 3.31, 3.32, and 3.36).

Yaw rate time constant The yaw rate time constants for $0-50[\%]$ and $100-0[\%]$ are shown in Table 3.31 and 3.32, respectively.

Table 3.31: Yaw step tests - time constant 0-50

Step 0-50 [%]	$T[s]$	$\delta[s]$
Starboard, 3kn	4.7	2.1
Port, 3kn	5.6	2.0
Starboard, 6kn	2.9	2.0
Port, 6kn	3.0	1.9

Table 3.32: Yaw step tests - time constant 100-0

Step 100-0 [%]	$T[s]$	$\delta[s]$
Starboard, 3kn	10.5	5.2
Port, 3kn	7.4	5.6
Starboard, 6kn	4.7	6.1
Port, 6kn	5.1	5.6

Rudder time constant Based on the plot of rudder angle, and assuming that the steps were applied when the rudder starts to change angle, the time constant is found for the rudder response for the different yaw maneuvers in the tables below.

Table 3.33: Yaw step tests - rudder time constant, starboard 3 kn

Step mag. [%]	$T_{sb}[s]$	δ_{sb}	$T_{port}[s]$	$\delta_{port}[s]$
0-50	1.8	0.8	1.7	1.3
50-100	2.4	1.0	2.3	1.0
100-0	4.2	1.4	4.2	1.5

Table 3.34: Yaw step tests - rudder time constant, port 3 kn

Step mag. [%]	$T_{sb}[s]$	δ_{sb}	$T_{port}[s]$	$\delta_{port}[s]$
0-50	1.8	0.9	2.0	0.7
50-100	2.4	1.0	2.4	1.2
100-0	4.2	1.4	4.4	1.5

Table 3.35: Yaw step tests - rudder time constant, starboard 6 kn

Step mag. [%]	$T_{sb}[s]$	δ_{sb}	$T_{port}[s]$	$\delta_{port}[s]$
0-50	1.8	1.0	1.8	1.0
50-100	2.1	1.2	2.3	1.1
100-0	4.2	1.5	4.1	1.5

Table 3.36: Yaw step tests - rudder time constant, port 6 kn

Step mag. [%]	$T_{sb}[s]$	δ_{sb}	$T_{port}[s]$	$\delta_{port}[s]$
0-50	1.8	0.9	1.7	1.0
50-100	2.3	1.1	2.3	1.0
100-0	4.1	1.4	4.1	1.4

3.6 Conclusions and further work

The data logging of this chapter is simple, and the results give a rough indication of performance of the system. The different maneuvers give an overall indication of DP performance, the thruster performance, and how the thruster system in combination with the vessel hull behave.

The agility tests give a simple and graphical measure of thruster response time. A DP 4 corner for the new thruster configuration could give good indications on power consumption, and total (accumulated) thruster force, and the same for the pure DP maneuvers. It is a drawback that much data for the tunnel thruster is lacking. Because of this, the DP 4 corner would only give a rough performance comparison. Also, the thrust mapping used is somewhat simple, and does not take loss effects into account. This means that the thrust force calculated is more accurate under normal (no significant thrust losses), and zero speed conditions. For the November sea trials, the rotational direction of the shaft speed is not known, so the thrust data is not very reliable for these maneuvers, but it gives a rough indication.

For further work the same tests should be run with the new thruster configuration, and the new tests should be performed under similar environmental conditions. For the agility plots, the DP 4 corner, and the pure DP maneuvers the same data as the data reported in this chapter should be reported for the new system to compare. Similarly for the step tests it could be interesting to see how the new thurster system responds, and how the vessel responds. For the step tests, especially for the sway step tests, longer tests should be run, such that it is certain that steady state is reached.

Chapter 4

Lever arm estimation for GNSS and MRU sensors

This Chapter considers the topic of estimating the body frame position of the GNSS and MRU sensors. For the GNSS position an observer design and an adaptive scheme are proposed and analyzed. The estimation designs are tested using numerical simulations and experimental data from the Gunnerus sea trials. A similar observer is proposed for the MRU positions, and experimental data from the sea trials are used to test the observer.

4.1 Introduction

In automatic motion control of marine vessels we usually consider set-point stabilization. This means that the vessel is actuated such that a defined point P_0 in the vessel body frame converges to and tracks a predefined position or path in the NED frame. As it is often impractical or impossible to place motion sensing equipment in P_0, it is important to know accurately where the sensors are placed. This makes it possible to compensate for the motion difference between the sensor location and P_0. If this is inaccurate it may lead to degraded position tracking performance and increased fuel consumption. Today, these lever arms are measured at dock using a laser surveying technique. Although accurate, it is time consuming, expensive, and potentially subject to human errors as the laser equipment must be moved several times for each lever arm. Therefore, this Chapter proposes to estimate the lever arms of both GNSS antennas and MRUs numerically using the sensor measurements from a maneuver with sufficient rotation and movement of the vessel. This is attractive as it removes the human influence and does not requiring expensive time at dock.

For GPS and INS integration extensive research has been performed in Tang et al. (2009),

Hong et al. (2005), Hong et al. (2006), Hong et al. (2004), a single antenna GPS with accurate measurements is used in combination with a low-grade inertial measurement unit (IMU). In Hong et al. (2005) the observability of the error states in the INS/GPS integrated system is studied, and in Hong et al. (2006) experimental studies verify the lever arm estimation of the GPS antenna using a setup on a car. In Batista et al. (2011) observability of linear motion quantities in navigation systems is considered, and sufficient and necessary conditions for observability are derived.

4.1.1 Scope

The scope of work is to analyze and test the two following methods for simultaneously estimating multiple lever arms for GNSS sensors:

- A Luenberger observer design
- An adaptive observer design

These methods will be analytically derived and their stability properties will be analyzed. As a part of this, observability and persistence of excitation investigations will be performed to investigate what level of motion and perturbation is required for the lever arm estimates to converge to the true values.

The observability of the system is considered in Section 4.2.1, and requirement for the problem to be observable is found. A design for a (Luenberger) observer is proposed, and stability is proven (Section 4.2.1). In Section 4.2.2 an adaptive observer is proposed, and stability and convergence of the adaptive observer is shown in Section 4.2.2. Further, the persistence of excitation criteria is investigated in Section 4.2.2.

Also, in Section 4.3 the problem setup for MRU lever arms are formulated, and in Section 4.3.1 the observability of the dynamics is considered. In Section 4.3.2 an observer is proposed.

For the GNSS lever arms two case studies with data from the sea trials with R/V Gunnerus are performed in Section 4.4. In the first case study (Section 4.4.1) data from a sea trial is used, but the GPS data is simulated, and in the second 4.4.1 experimental GPS data is used. A case study for the MRU lever arms is performed in Section 4.4.2. Data from a sea trial with R/V Gunnerus is used.

In the following, the rotation matrix will be viewed as a signal, such that the system equations, instead of being nonlinear, can be treated as linear time varying (LTV). The GNSS and MRU problems are treated separately, and it is assumed that all needed measurements are available.

4.2 GNSS

As discussed in Section 4.1 $\boldsymbol{P}_0$ is normally a pre-defined point on the vessel. From this point the lever arms to the different GNSS antennas are measured by surveying with laser equipment. Then the measurements from the GNSS antennas are used to find the NED position of $\boldsymbol{P}_0$ as the vessel is in operation.

When the GNSS measurements are used in a estimation algorithm to find the lever arms, the $\boldsymbol{P}_0$ position that is found is the NED-position of the rotation point of the vessel. Depending on the operation, or load condition this rotation point would move.

4.2.1 Luenberger observer design

The GNSS positions in the North-East-Down (NED) frame is given as

$$\boldsymbol{P}_{GNSSi} = \begin{bmatrix} P_{GNSSi_N} & P_{GNSSi_E} & P_{GNSSi_D} \end{bmatrix}^\top \in \mathbb{R}^3, \tag{4.1}$$

where i denotes a GNSS sensor. For m GNSS sensors this can be written

$$\begin{aligned} \boldsymbol{P}_{GNSS1}(t) &= \boldsymbol{P}_0(t) + \boldsymbol{R}(\boldsymbol{\Theta})\boldsymbol{l}_1 \\ \boldsymbol{P}_{GNSS2}(t) &= \boldsymbol{P}_0(t) + \boldsymbol{R}(\boldsymbol{\Theta})\boldsymbol{l}_2 \\ &\vdots \\ \boldsymbol{P}_{GNSSm}(t) &= \boldsymbol{P}_0(t) + \boldsymbol{R}(\boldsymbol{\Theta})\boldsymbol{l}_m \end{aligned} \tag{4.2}$$

where

$$\boldsymbol{l}_i = \begin{bmatrix} l_{xi} \\ l_{yi} \\ l_{zi} \end{bmatrix}, \quad i = 1 \dots m, \tag{4.3}$$

is a vector that contains the body fixed coordinates of a lever arm, and $\boldsymbol{P}_0(t)$ is the NED-position of the vessel rotation point as discussed in Section 4.1. The rotation matrix $\boldsymbol{R}(\boldsymbol{\Theta})$ between the BODY and the NED frame given by Eq. (2.4) of Section 2.1.1.

Eq. (4.2) can be written as

$$\boldsymbol{x} = \begin{bmatrix} \boldsymbol{P}_0 \\ \boldsymbol{l}_1 \\ \boldsymbol{l}_2 \\ \vdots \\ \boldsymbol{l}_m \end{bmatrix} \in \mathbb{R}^{3n}, \quad n = m + 1, \tag{4.4}$$

$$\boldsymbol{y} = \begin{bmatrix} \boldsymbol{P}_{GNSS1} \\ \boldsymbol{P}_{GNSS2} \\ \vdots \\ \boldsymbol{P}_{GNSSm} \end{bmatrix} \in \mathbb{R}^{3m}, \tag{4.5}$$

where $\boldsymbol{x}$ consists of the states to be estimated, and $\boldsymbol{y}$ is the output.

As mentioned in Section 4.1.1 the Euler angles (ϕ, θ, and ψ) Fossen (2011) are viewed as an input signals to the system, so it is a linear time varying (LTV) system, instead of a nonlinear system, setting $\boldsymbol{R}(\boldsymbol{\Theta}) := \boldsymbol{R}(t)$. Also, p, q, r, and $\dot{p}$, $\dot{q}$, and $\dot{r}$ are considered input signals.

The dynamics of $\boldsymbol{P}_0$ can be represented as (Fossen, 2011)

$$\dot{\boldsymbol{P}}_0 = \boldsymbol{R}(t)\boldsymbol{\nu}(t), \tag{4.6}$$

where $\boldsymbol{\nu} = \begin{bmatrix} u & v & w \end{bmatrix}^\top$ is the linear velocity of the vessel in BODY-coordinates, assumed measured. The lever arms are constants, and hence

$$\dot{\boldsymbol{l}}_i = \boldsymbol{0}, \quad i = 1 \dots m. \tag{4.7}$$

The dynamic lever arm system can be written as

$$\dot{\boldsymbol{x}} = \boldsymbol{A}\boldsymbol{x} + \boldsymbol{B}(t)\boldsymbol{\nu}(t), \tag{4.8}$$
$$\boldsymbol{y} = \boldsymbol{C}(t)\boldsymbol{x}. \tag{4.9}$$

The matrices of (4.8) and (4.9) are given by

$$\boldsymbol{A} = \boldsymbol{0}_{3n\times 3n}, \tag{4.10}$$
$$\boldsymbol{B}(t) = \begin{bmatrix} \boldsymbol{R}(t)^\top & \boldsymbol{0}_{3\times 3} & \boldsymbol{0}_{3\times 3} & \cdots & \boldsymbol{0}_{3\times 3} \end{bmatrix}^\top \in \mathbb{R}^{3n\times 3}, \tag{4.11}$$

$$\boldsymbol{C}(t) = \begin{bmatrix} \boldsymbol{I}_{3\times 3} & \boldsymbol{R}(t) & \boldsymbol{0}_{3\times 3} & \cdots & \boldsymbol{0}_{3\times 3} \\ \boldsymbol{I}_{3\times 3} & \boldsymbol{0}_{3\times 3} & \boldsymbol{R}(t) & \ddots & \vdots \\ \vdots & \vdots & \ddots & \ddots & \boldsymbol{0}_{3\times 3} \\ \boldsymbol{I}_{3\times 3} & \boldsymbol{0}_{3\times 3} & \cdots & \boldsymbol{0}_{3\times 3} & \boldsymbol{R}(t) \end{bmatrix} \in \mathbb{R}^{3m\times 3n}. \tag{4.12}$$

Observability assessment

In this section an observability criterion for the system given by Eq. (4.8) - (4.9) will be investigated. Because the $\boldsymbol{A}$ matrix of (4.8) is zero, the state transition matrix is identity. This gives the following observability gramian for the system as (Chen, 2009),

$$\boldsymbol{W}_0(t_0, t_1) = \int_{t_0}^{t_1} \boldsymbol{C}(\tau)^\top \boldsymbol{C}(\tau) \mathrm{d}\tau, \tag{4.13}$$

and if $\boldsymbol{W}_0(t_0, t_1)$ is nonsingular, the system is observable (Chen, 2009).

$\boldsymbol{C}(t)^\top$ for (4.8) - (4.9) is

$$\boldsymbol{C}(t)^\top = \begin{bmatrix} \boldsymbol{I}_{3\times3} & \boldsymbol{I}_{3\times3} & \cdots & \boldsymbol{I}_{3\times3} \\ \boldsymbol{R}(t)^\top & \boldsymbol{0}_{3\times3} & \cdots & \boldsymbol{0}_{3\times3} \\ \boldsymbol{0}_{3\times3} & \boldsymbol{R}(t)^\top & \ddots & \vdots \\ \vdots & \ddots & \ddots & \boldsymbol{0}_{3\times3} \\ \boldsymbol{0}_{3\times3} & \cdots & \boldsymbol{0}_{3\times3} & \boldsymbol{R}(t)^\top \end{bmatrix} \in \mathbb{R}^{3n\times3m}, \tag{4.14}$$

and $\boldsymbol{C}(t)^\top\boldsymbol{C}(t)$ is given as

$$\boldsymbol{C}(t)^\top\boldsymbol{C}(t) = \begin{bmatrix} (n-1)\boldsymbol{I}_{3\times3} & \boldsymbol{R}(t) & \cdots & \boldsymbol{R}(t) & \boldsymbol{R}(t) \\ \boldsymbol{R}(t)^\top & \boldsymbol{I}_{3\times3} & \boldsymbol{0}_{3\times3} & \cdots & \boldsymbol{0}_{3\times3} \\ \vdots & \boldsymbol{0}_{3\times3} & \ddots & \ddots & \vdots \\ \boldsymbol{R}(t)^\top & \vdots & \ddots & I_{3\times3} & \boldsymbol{0}_{3\times3} \\ \boldsymbol{R}(t)^\top & \boldsymbol{0}_{3\times3} & \cdots & \boldsymbol{0}_{3\times3} & \boldsymbol{I}_{3\times3} \end{bmatrix} \in \mathbb{R}^{3n\times3n}. \tag{4.15}$$

From (4.12) it can be found that if $\boldsymbol{R}(t)$ has full rank, then $\boldsymbol{C}(t)$ and $\boldsymbol{C}(t)^\top$ also have full rank, i.e. $3m$. From Chen (2009) it is found that the rank of $\boldsymbol{C}(t)^\top\boldsymbol{C}(t) \in \mathbb{R}^{3n\times3n}$ will at most be $3m$, as

$$rank(\boldsymbol{AB}) \leq min(\text{rank}(\boldsymbol{A}), \text{rank}(\boldsymbol{B})) \tag{4.16}$$

where both $\boldsymbol{A}$ and $\boldsymbol{B}$ are matrices. In other words the matrix is not full rank in the first place, and need to "add rank" as time increases (Anderson et al., 1986). To find the observability condition(s), Theorem 6.O12 from Chen (2009) is used.

Theorem 1 (Thm 6.O12 (Chen, 2009))**.** *Let $\boldsymbol{A}(t)$ and $\boldsymbol{C}(t)$ be continously differentiable, then the n-dimensional pair $(\boldsymbol{A}(t), \boldsymbol{C}(t))$ is observable at t_0 if there exists a finite $t_1 > t_0$ such that*

$$rank \begin{bmatrix} \boldsymbol{N}_0 \\ \boldsymbol{N}_1 \\ \vdots \\ \boldsymbol{N}_{n-1} \end{bmatrix} = n$$

where $\boldsymbol{N}_{m+1} = \boldsymbol{N}_m(t)\boldsymbol{A}(t) + \frac{d}{dt}\boldsymbol{N}_m(t) \quad m = 0, 1 \ldots n-1$
with $\boldsymbol{N}_0 = \boldsymbol{C}(t)$.

For the system of (4.8) - (4.9) both $\boldsymbol{C}(t)$ and $\boldsymbol{A}(t)$ are continuously differentiable, and $\boldsymbol{C}(t)$ has rank $3m$ given that $\boldsymbol{R}(t)$ has full rank. Hence, given $\boldsymbol{C}(t)$ full row rank, a rank of 3 is lacking to fulfil rank n of theorem 6.O12 ($\boldsymbol{C}(t)$ has three more columns than rows). Thus, $\boldsymbol{N}_1, ...\boldsymbol{N}_{n-1}$ must contribute with 3 more independent rows for the observability condition to be satisfied.

$\boldsymbol{N}_1$**:**

$$\boldsymbol{N}_1 = \boldsymbol{N}_0(t)\boldsymbol{A}(t) + \frac{d}{dt}\boldsymbol{N}_0(t) \tag{4.17}$$

$$= \boldsymbol{0}_{3\times3} + \frac{d}{dt}\boldsymbol{C}(t), \tag{4.18}$$

$$\dot{C} = \begin{bmatrix} \mathbf{0}_{3\times3} & \boldsymbol{R}(t)\boldsymbol{S}(t) & \mathbf{0}_{3\times3} & \cdots & \mathbf{0}_{3\times3} \\ \mathbf{0}_{3\times3} & \mathbf{0}_{3\times3} & \boldsymbol{R}(t)\boldsymbol{S}(t) & \ddots & \vdots \\ \vdots & \vdots & \ddots & \ddots & \mathbf{0}_{3\times3} \\ \mathbf{0}_{3\times3} & \mathbf{0}_{3\times3} & \cdots & \mathbf{0}_{3\times3} & \boldsymbol{R}(t)\boldsymbol{S}(t) \end{bmatrix}, \tag{4.19}$$

where it has been used that $\dot{\boldsymbol{R}}(t) = \boldsymbol{R}(t)\boldsymbol{S}(t)$ from Eq. 2.5, and $\boldsymbol{S}(t)$ is given by Eq. (2.6).

$\boldsymbol{N}_2$:

$$\boldsymbol{N}_2 = \boldsymbol{N}_1(t)\boldsymbol{A}(t) + \frac{d}{dt}\boldsymbol{N}_1(t) \tag{4.20}$$

$$= \ddot{\boldsymbol{C}}(t), \tag{4.21}$$

$$\ddot{\boldsymbol{C}} = \begin{bmatrix} \mathbf{0}_{3\times3} & \boldsymbol{R}(t)[\boldsymbol{S}(t)^2 + \dot{\boldsymbol{S}}(t)] & \mathbf{0}_{3\times3} & \cdots & \mathbf{0}_{3\times3} \\ \mathbf{0}_{3\times3} & \mathbf{0}_{3\times3} & \boldsymbol{R}(t)[\boldsymbol{S}(t)^2 + \dot{\boldsymbol{S}}(t)] & \ddots & \vdots \\ \vdots & \vdots & \ddots & \ddots & \mathbf{0}_{3\times3} \\ \mathbf{0}_{3\times3} & \mathbf{0}_{3\times3} & \cdots & \mathbf{0}_{3\times3} & \boldsymbol{R}(t)[\boldsymbol{S}(t)^2 + \dot{\boldsymbol{S}}(t)] \end{bmatrix}. \tag{4.22}$$

giving

$$\begin{bmatrix} \boldsymbol{N}_0 \\ \boldsymbol{N}_1 \\ \boldsymbol{N}_2 \end{bmatrix} = \begin{bmatrix} \boldsymbol{I}_{3\times3} & \boldsymbol{R}(t) & \mathbf{0}_{3\times3} & \cdots & \mathbf{0}_{3\times3} \\ \boldsymbol{I}_{3\times3} & \mathbf{0}_{3\times3} & \boldsymbol{R}(t) & \ddots & \vdots \\ \vdots & \vdots & \ddots & \ddots & \mathbf{0}_{3\times3} \\ \boldsymbol{I}_{3\times3} & \mathbf{0}_{3\times3} & \cdots & \mathbf{0}_{3\times3} & \boldsymbol{R}(t) \\ \mathbf{0}_{3\times3} & \boldsymbol{R}(t)\boldsymbol{S}(t) & \mathbf{0}_{3\times3} & \cdots & \mathbf{0}_{3\times3} \\ \mathbf{0}_{3\times3} & \mathbf{0}_{3\times3} & \boldsymbol{R}(t)\boldsymbol{S}(t) & \ddots & \vdots \\ \vdots & \vdots & \ddots & \ddots & \mathbf{0}_{3\times3} \\ \mathbf{0}_{3\times3} & \mathbf{0}_{3\times3} & \cdots & \mathbf{0}_{3\times3} & \boldsymbol{R}(t)\boldsymbol{S}(t) \\ \mathbf{0}_{3\times3} & \boldsymbol{R}(t)[\boldsymbol{S}(t)^2 + \dot{\boldsymbol{S}}(t)] & \mathbf{0}_{3\times3} & \cdots & 0_{3\times3} \\ \mathbf{0}_{3\times3} & \mathbf{0}_{3\times3} & \boldsymbol{R}(t)[\boldsymbol{S}(t)^2 + \dot{\boldsymbol{S}}(t)] & \ddots & \vdots \\ \vdots & \vdots & \ddots & \ddots & \mathbf{0}_{3\times3} \\ \mathbf{0}_{3\times3} & \mathbf{0}_{3\times3} & \cdots & \mathbf{0}_{3\times3} & \boldsymbol{R}(t)[\boldsymbol{S}(t)^2 + \dot{\boldsymbol{S}}(t)] \end{bmatrix}, \tag{4.23}$$

where

$$\dot{\boldsymbol{S}} = \begin{bmatrix} 0 & -\dot{r} & \dot{q} \\ \dot{r} & 0 & -\dot{p} \\ -\dot{q} & \dot{p} & 0 \end{bmatrix}. \tag{4.24}$$

For the system to be observable, the requirement is that there exists a time t_1 such that

$$\text{rank}(\begin{bmatrix} \boldsymbol{N}_0 \\ \boldsymbol{N}_1 \\ \boldsymbol{N}_2 \end{bmatrix}) = 3n.$$

Since $\boldsymbol{S}(t)$ is a skew-symmetric matrix, it is always singular. The observability requirement is therefore that there has to exists a time t_1 where rank $(\boldsymbol{R}(t)[\boldsymbol{S}(t)^2 + \dot{\boldsymbol{S}}(t)]) = 3$. Since $\det \boldsymbol{R}(t) = 1$, $\boldsymbol{R}(t)$ is always nonsingular (Chen, 2009), and the observability requirement reduce to that $[\boldsymbol{S}(t)^2 + \dot{\boldsymbol{S}}(t)]$ need to have full rank. This is summarized in the proposition below.

Proposition 1. *For the system of (4.8) and (4.9) to be observable at time t_0, there have to exist a time $t_1 > t_0$ where*

$$\textit{rank}[\boldsymbol{S}(t)^2 + \dot{\boldsymbol{S}}(t)] = 3. \tag{4.25}$$

Example 1. *For a constant yaw rate $r = 1$, $p, q, \dot{r}, \dot{q} = 0$, and $\dot{p} = 0.1$ at t_1, $\boldsymbol{S}(t)^2 + \dot{\boldsymbol{S}}(t)$ becomes*

$$\boldsymbol{S}(t)^2 + \dot{\boldsymbol{S}}(t) = \begin{bmatrix} -1 & 0 & 0 \\ 0 & -1 & -0.1 \\ 0 & 0.1 & 0 \end{bmatrix}$$

which has full rank.

By trying to maneuver the vessel with a constant yaw rate r, observability will be assured if there also exists some acceleration in roll or pitch. This will in practice always be the case.

Luenberger observer design and stability analysis

For the system dynamics of equations (4.8), and (4.9) the following observer is proposed

$$\begin{aligned} \dot{\hat{\boldsymbol{x}}} &= \boldsymbol{B}(t)\boldsymbol{\nu}(t) + \boldsymbol{W}\boldsymbol{C}(t)^\top \tilde{\boldsymbol{y}} \\ &= \boldsymbol{B}(t)\boldsymbol{v}(t) + \boldsymbol{W}\boldsymbol{C}(t)^\top \boldsymbol{C}(t)\tilde{\boldsymbol{x}}, \end{aligned} \tag{4.26}$$

$$\tilde{\boldsymbol{y}} = \boldsymbol{C}(t)\tilde{\boldsymbol{x}}, \tag{4.27}$$

where $\boldsymbol{W} = \boldsymbol{W}^\top > 0 \in \mathbb{R}^{3n \times 3n}$, $\tilde{\boldsymbol{x}} = \boldsymbol{x} - \hat{\boldsymbol{x}}$, $\tilde{\boldsymbol{y}} = \boldsymbol{y} - \hat{\boldsymbol{y}}$, and with closed loop error dynamics as

$$\dot{\tilde{\boldsymbol{x}}} = -\boldsymbol{W}\boldsymbol{C}(t)^\top \boldsymbol{C}(t)\tilde{\boldsymbol{x}}. \tag{4.28}$$

In order to evaluate the stability properties of the observer design, the following lemma from Anderson et al. (1986) is applied.

Lemma 1. *Exponential stability of LTV system (Anderson et al., 1986)*
For a system given by $\dot{\boldsymbol{x}} = \boldsymbol{F}(t)\boldsymbol{x}$, and the function $\boldsymbol{F}(\cdot)$ is locally integrable. Suppose there exits a positive definite matrix $\boldsymbol{P} = \boldsymbol{P}^\top > 0$ such that

$$\boldsymbol{P}\boldsymbol{F}(t) + \boldsymbol{F}(t)^\top \boldsymbol{P} \leq -\boldsymbol{N}(t)^\top \boldsymbol{N}(t) \tag{4.29}$$

for some matrix function $\boldsymbol{N}(\cdot)$ and all t. Then $\dot{\boldsymbol{x}} = \boldsymbol{F}(\boldsymbol{t})\boldsymbol{x}$ is uniformly stable in the sense of Lyapunov.

If, further the pair $[\boldsymbol{F}(t), \boldsymbol{N}(t)]$ *is uniformly completely observable, that is, writing* $\boldsymbol{\phi}(t,\tau)$ *as the transition function of* $\dot{\boldsymbol{x}} = \boldsymbol{F}(t)\boldsymbol{x}$*, there exits* $T > 0,\ \beta > 0,\ \alpha > 0$ *such that*

$$\beta \boldsymbol{I} \geq \int_t^{t+T} \boldsymbol{\phi}(t,\tau)^\top \boldsymbol{C}(\tau)^\top \boldsymbol{C}(\tau)\boldsymbol{\phi}(t,\tau)\mathrm{d}\tau \geq \alpha \boldsymbol{I}$$

then $\dot{\boldsymbol{x}} = \boldsymbol{F}(t)\boldsymbol{x}$ *is exponentially stable.*

From equations (4.27) and (4.28), $F(t) = -\boldsymbol{W}\boldsymbol{C}(t)^\top \boldsymbol{C}(t)$ and $\boldsymbol{P} = \boldsymbol{W}^{-1}$ gives

$$\begin{aligned} \boldsymbol{P}\boldsymbol{F}(t) + \boldsymbol{F}(t)^\top \boldsymbol{P} &= -2\boldsymbol{C}(t)^\top \boldsymbol{C}(t) \\ &= -\boldsymbol{N}(t)^\top \boldsymbol{N}(t), \end{aligned} \tag{4.30}$$

where

$$\boldsymbol{N}(t) = \sqrt{2}\boldsymbol{C}(t), \tag{4.31}$$

and the discussion above is summarized in Theorem 2 below.

Theorem 2. *The observer design of (4.26) is exponentially stable given that the observability condition of Proposition 1 holds, according to Lemma 1.*

4.2.2 Adaptive observer design

Another way to solve the lever arm estimation problem is an adaptive solution. This set up will remove $\boldsymbol{P}_0$ as a variable to be estimated, and thus have full state measurements available. The value of $\boldsymbol{P}_0$ can then be found once the lever arms have converged, from Eq. (4.2) as

$$\boldsymbol{P}_0 = \boldsymbol{P}_{GNSSi}(t) - \boldsymbol{R}(\boldsymbol{\Theta})\boldsymbol{l}_i. \tag{4.32}$$

By taking the time derivative of (4.2), using (4.6) and $\boldsymbol{R}(\Theta) = \boldsymbol{R}(t),\ \boldsymbol{S}(\omega) = \boldsymbol{S}(t)$, the lever arm problem can be formulated as

$$\begin{aligned} \dot{\boldsymbol{P}}_{GNSS1}(t) &= \boldsymbol{R}(t)\boldsymbol{\nu}(t) + \boldsymbol{R}(t)\boldsymbol{S}(t)\boldsymbol{l}_1 \\ \dot{\boldsymbol{P}}_{GNSS2}(t) &= \boldsymbol{R}(t)\boldsymbol{\nu}(t) + \boldsymbol{R}(t)\boldsymbol{S}(t)\boldsymbol{l}_2 \\ &\vdots \\ \dot{\boldsymbol{P}}_{GNSSn}(t) &= \boldsymbol{R}(t)\boldsymbol{\nu}(t) + \boldsymbol{R}(t)\boldsymbol{S}(t)\boldsymbol{l}_n, \end{aligned} \tag{4.33}$$

and Eq. 4.33 can be written as

$$\boldsymbol{x}(t) = \begin{bmatrix} \boldsymbol{P}_{GNSS1} \\ \boldsymbol{P}_{GNSS2} \\ \vdots \\ \boldsymbol{P}_{GNSSn} \end{bmatrix}, \tag{4.34}$$

$$\boldsymbol{y}(t) = \boldsymbol{I}_{3n\times 3n}\boldsymbol{x}, \tag{4.35}$$

where $\boldsymbol{x}$ are the states to be estimated, and $\boldsymbol{y}$ is the output. This system can be written as

$$\dot{\boldsymbol{x}} = \boldsymbol{B}(t)\boldsymbol{\nu}(t) + \boldsymbol{\Omega}(t)\boldsymbol{\varphi}, \tag{4.36}$$
$$\boldsymbol{y} = \boldsymbol{C}\boldsymbol{x}, \tag{4.37}$$

where

$$\boldsymbol{B}(t) = \begin{bmatrix} \boldsymbol{R}(t) \\ \boldsymbol{R}(t) \\ \vdots \\ \boldsymbol{R}(t) \end{bmatrix} \in \mathbb{R}^{3n\times 3}, \tag{4.38}$$
$$\boldsymbol{C} = \boldsymbol{I}_{3n\times 3n}, \tag{4.39}$$
$$\boldsymbol{\varphi} = \begin{bmatrix} \boldsymbol{l}_1 \\ \boldsymbol{l}_2 \\ \cdots \\ \boldsymbol{l}_n \end{bmatrix} \in \mathbb{R}^{3n}, \tag{4.40}$$

$$\boldsymbol{\Omega}(t) = \begin{bmatrix} \boldsymbol{R}(t)\boldsymbol{S}(t) & \boldsymbol{0}_{3\times 3} & \cdots & \boldsymbol{0}_{3\times 3} \\ 0_{3\times 3} & \boldsymbol{R}(t)\boldsymbol{S}(t) & \ddots & \vdots \\ \vdots & & \ddots & \boldsymbol{0}_{3\times 3} \\ \boldsymbol{0}_{3\times 3} & \cdots & \boldsymbol{0}_{3\times 3} & \boldsymbol{R}(t)\boldsymbol{S}(t) \end{bmatrix} \in \mathbb{R}^{3n\times 3n}. \tag{4.41}$$

Adaptive observer design and stability analysis

Let a state observer be given as

$$\begin{aligned} \dot{\hat{\boldsymbol{x}}} &= \boldsymbol{B}(t)\boldsymbol{\nu}(t) + \boldsymbol{\Omega}(t)\hat{\boldsymbol{\varphi}} + \boldsymbol{L}\boldsymbol{y} - \boldsymbol{L}\boldsymbol{C}\hat{\boldsymbol{x}} \\ &= \boldsymbol{B}(t)\boldsymbol{\nu}(\boldsymbol{t}) + \boldsymbol{\Omega}(t)\hat{\boldsymbol{\varphi}} + \boldsymbol{L}\boldsymbol{C}\tilde{\boldsymbol{x}}, \end{aligned} \tag{4.42}$$

where $\boldsymbol{L} \in \mathbb{R}^{3n\times 3n}$ and $\tilde{\boldsymbol{x}} = \boldsymbol{x} - \hat{\boldsymbol{x}}$. Let $\tilde{\boldsymbol{\varphi}} = \boldsymbol{\varphi} - \hat{\boldsymbol{\varphi}}$, and

$$\dot{\tilde{\boldsymbol{x}}} = \dot{\boldsymbol{x}} - \dot{\hat{\boldsymbol{x}}} = -\boldsymbol{L}\boldsymbol{C}\tilde{\boldsymbol{x}} + \boldsymbol{\Omega}\tilde{\boldsymbol{\varphi}}, \tag{4.43}$$
$$\dot{\tilde{\boldsymbol{\varphi}}} = \dot{\boldsymbol{\varphi}} - \dot{\hat{\boldsymbol{\varphi}}} = -\dot{\hat{\boldsymbol{\varphi}}}. \tag{4.44}$$

Define the following Control Lyapunov Function (CLF) (Khalil, 2002)

$$V = \frac{1}{2}\tilde{\boldsymbol{x}}^\top\tilde{\boldsymbol{x}} + \frac{1}{2}\tilde{\boldsymbol{\varphi}}^\top\boldsymbol{\Gamma}^{-1}\tilde{\boldsymbol{\varphi}}, \tag{4.45}$$

where the constant matrix $\boldsymbol{\Gamma} = \boldsymbol{\Gamma}^\top > 0$. This gives

$$\dot{V} = \tilde{\boldsymbol{x}}^\top[-\boldsymbol{L}\boldsymbol{C}\tilde{\boldsymbol{x}} + \boldsymbol{\Omega}\tilde{\boldsymbol{\varphi}}] + \tilde{\boldsymbol{\varphi}}^\top\boldsymbol{\Gamma}^{-1}(-\dot{\hat{\boldsymbol{\varphi}}}) \tag{4.46}$$
$$= -\tilde{\boldsymbol{x}}^\top\boldsymbol{L}\boldsymbol{C}\tilde{\boldsymbol{x}} + \tilde{\boldsymbol{x}}^\top\boldsymbol{\Omega}\tilde{\boldsymbol{\varphi}} - \tilde{\boldsymbol{\varphi}}^\top\boldsymbol{\Gamma}^{-1}\dot{\hat{\boldsymbol{\varphi}}}. \tag{4.47}$$

For the following update law for $\hat{\boldsymbol{\varphi}}$

$$\dot{\hat{\boldsymbol{\varphi}}} := \boldsymbol{\Gamma}\boldsymbol{\Omega}^\top \tilde{\boldsymbol{x}}, \tag{4.48}$$

$\dot{V}$ becomes

$$\dot{V} = -\tilde{\boldsymbol{x}}^\top \boldsymbol{L}\boldsymbol{C}\tilde{\boldsymbol{x}} \leq 0. \tag{4.49}$$

Let $\boldsymbol{L}\boldsymbol{C} > 0$, then $\dot{V}$ is negative semidefinite. Barbalat's lemma (Slotine and Li, 1991) is applied, and restated here for convenience.

Lemma 2. *(Barbalat's lemma) If the differentiable function f(t) has a finite limit as $t \to \infty$, and if $\dot{f}$ is uniformly continuous, then $f(t) \to 0$ as $t \to \infty$.*

To assess uniform continuity, Slotine and Li (1991) states that a sufficient condition for a differentiable function is that its derivative is bounded. For the above CLF, this implies that $\ddot{V}$ should be bounded, and $\ddot{V}$ is given as

$$\ddot{V} = -2\tilde{\boldsymbol{x}}^\top \boldsymbol{L}\boldsymbol{C}\dot{\tilde{\boldsymbol{x}}} \tag{4.50}$$

From Eq. (4.49) it is shown that $\dot{V} \leq 0$, and therefore V is bounded, and from (4.45) it can be concluded that both $\tilde{\boldsymbol{x}}$ and $\tilde{\boldsymbol{\varphi}}$ are bounded. From (4.43), since both $\tilde{\boldsymbol{x}}$ and $\tilde{\boldsymbol{\varphi}}$ are bounded, $\dot{\tilde{\boldsymbol{x}}}$ is bounded, and hence is $\ddot{V}$ bounded. So $\dot{V}$ is uniformly continuous, and by Barbalat's lemma $\dot{V} \to 0$ as $t \to \infty$, and hence $\tilde{\boldsymbol{x}} \to \boldsymbol{0}$ as $t \to \infty$. This implies that $\dot{\tilde{\boldsymbol{x}}} \to \boldsymbol{0}$ as $t \to \infty$, and from (4.43) it follows that $\boldsymbol{\Omega}\tilde{\boldsymbol{\varphi}} \to \boldsymbol{0}$ as $t \to \infty$.

Percistence of excitation

Consider $\boldsymbol{\Omega}\tilde{\boldsymbol{\varphi}} = \boldsymbol{0}$. In order to have $\tilde{\boldsymbol{\varphi}} = \boldsymbol{0}$ as the only solution $\boldsymbol{\Omega}$ need to be persistently excited. For a update law of the form (4.48), then persistence of excitation (PE) can be formulated as (Slotine and Li, 1991)

Theorem 3. *(Persistence of excitation) The matrix $\boldsymbol{\Omega}$ is persistently excited if there exists $\alpha, T > 0$ such that $\forall t$*

$$\int_t^{t+T} \boldsymbol{\Omega}(\tau)^\top \boldsymbol{\Omega}(\boldsymbol{\tau})\mathrm{d}\tau > \alpha \boldsymbol{I} \tag{4.51}$$

Seeing that $\boldsymbol{\Omega}(t)$ is diagonal, condition (4.51) will only depend on $\boldsymbol{R}(t)\boldsymbol{S}(t)$, and PE criterion can be evaluated based on $\boldsymbol{R}(t)\boldsymbol{S}(t)$ as the integrand (with $\boldsymbol{I} := \boldsymbol{I}_{3\times 3}$ in (4.51)). Looking at the integrand

$$(\boldsymbol{R}(t)\boldsymbol{S}(t))^\top \boldsymbol{R}(t)\boldsymbol{S}(t) = \boldsymbol{S}(t)^\top \boldsymbol{R}(t)^\top \boldsymbol{R}(t)\boldsymbol{S}(t) \tag{4.52}$$

$$= \boldsymbol{S}(t)^\top \boldsymbol{S}(t). \tag{4.53}$$

This result is valid due to $\boldsymbol{R}^\top \boldsymbol{R} = \boldsymbol{I}$, which is a fundamental property of the rotation matrix (Fossen, 2011). The expression for $\boldsymbol{S}(t)^\top \boldsymbol{S}(t)$ is given as

$$\boldsymbol{S}(t)^\top \boldsymbol{S}(t) = \begin{bmatrix} r(t)^2 + q(t)^2 & -p(t)q(t) & -p(t)r(t) \\ -p(t)q(t) & r(t)^2 + p(t)^2 & -q(t)r(t) \\ -p(t)r(t) & -q(t)r(t) & p(t)^2 + q(t)^2 \end{bmatrix}, \tag{4.54}$$

and the PE criteria can be written as

$$\int_t^{t+T} \boldsymbol{S}(\tau)^\top \boldsymbol{S}(\tau)\mathrm{d}\tau = \begin{bmatrix} \int_t^{t+T}[q(\tau)^2+r(\tau)^2]\mathrm{d}\tau & -\int_t^{t+T} p(\tau)q(\tau)\mathrm{d}\tau & -\int_t^{t+T} p(\tau)r(\tau)\mathrm{d}\tau \\ -\int_t^{t+T} p(\tau)q(\tau)\mathrm{d}\tau & \int_t^{t+T}[p(\tau)^2+r(\tau)^2]\mathrm{d}\tau & -\int_t^{t+T} q(\tau)r(\tau)\mathrm{d}\tau \\ -\int_t^{t+T} p(\tau)r(\tau)\mathrm{d}\tau & -\int_t^{t+T} q(\tau)r(\tau)\mathrm{d}\tau & \int_t^{t+T}[p(\tau)^2+q(\tau)^2]\mathrm{d}\tau \end{bmatrix} > \alpha \boldsymbol{I}_{3\times 3}, \tag{4.55}$$

A matrix is positive definite if the leading principal minors are positive (Chen, 2009). This gives the following three conditions for Eq. (4.55) to be satisfied

1.
$$\int_t^{t+T}[q(\tau)^2+r(\tau)^2]\mathrm{d}\tau > 0 \tag{4.56}$$

2.
$$\int_t^{t+T}[q(\tau)^2+r(\tau)^2]\mathrm{d}\tau \int_t^{t+T}[p(\tau)^2+r(\tau)^2]\mathrm{d}\tau - \left[\int_t^{t+T} p(\tau)q(\tau)\mathrm{d}\tau\right]^2 > 0 \tag{4.57}$$

3.
$$\begin{aligned} &\int_t^{t+T}[q(\tau)^2+r(\tau)^2]\mathrm{d}\tau \left\{\int_t^{t+T}[p(\tau)^2+r(\tau)^2]\mathrm{d}\tau \int_t^{t+T}[p(\tau)^2+q(\tau)^2]\mathrm{d}\tau - \right. \\ &\left.\left[\int_t^{t+T} q(\tau)r(\tau)\mathrm{d}\tau\right]^2\right\} - \\ &\int_t^{t+T} p(\tau)q(\tau)\mathrm{d}\tau \left\{\int_t^{t+T} p(\tau)q(\tau)\mathrm{d}\tau \int_t^{t+T}[p(\tau)^2+q(\tau)^2]\mathrm{d}\tau + \right. \\ &\left.\int_t^{t+T} q(\tau)r(\tau)\mathrm{d}\tau \int_t^{t+T} p(\tau)r(\tau)\mathrm{d}\tau\right\} - \\ &\int_t^{t+T} p(\tau)r(\tau)\mathrm{d}\tau \left\{\int_t^{t+T} p(\tau)q(\tau)\mathrm{d}\tau \int_t^{t+T} q(\tau)r(\tau)\mathrm{d}\tau + \right. \\ &\left.\int_t^{t+T} p(\tau)r(\tau)\mathrm{d}\tau \int_t^{t+T}[p(\tau)^2+r(\tau)^2]\mathrm{d}\tau\right\} > 0 \end{aligned} \tag{4.58}$$

Proposition 2 (PE of adaptive observer)**.** *The adaptive observer of Eq. (4.42) and (4.48) is persistently excited if the conditions of (4.56) - (4.58) are satisfied.*

Remark 1. *If $p = 0 \; \forall \; \bar{t} \in [t, t+T]$, the minimum requirement is that $r \neq 0$ for some time $\bar{t}$ in $[t, t+T]$, and that*

$$\int_t^{t+T} r(\tau)^2 \mathrm{d}\tau \int_t^{t+T} q(\tau)^2 \mathrm{d}\tau > \left[\int_t^{t+T} q(\tau) r(\tau) \mathrm{d}\tau \right]^2, \tag{4.59}$$

is satisfied. If $q = 0 \; \forall \; \bar{t} \in [t, t+T]$, the minimum requirement is that $r \neq 0$ for some time $\bar{t}$ in $[t, t+T]$, and that

$$\int_t^{t+T} r(\tau)^2 \mathrm{d}\tau > \left[\int_t^{t+T} p(\tau) r(\tau) \mathrm{d}\tau \right]^2, \tag{4.60}$$

is satisfied.

Example 2. *For a constant yaw rate (steady turn) r, that is nonzero for a time T, assume pitch motion is zero, and roll motion oscillates with a zero mean value. Let*

$$p(t) = \sin(t), \tag{4.61}$$
$$q(t) = 0, \tag{4.62}$$
$$r(t) = c_r \neq 0 \;\; \forall t \in [t, t+T], \tag{4.63}$$

where c_r is a constant. The left side of Eq. (4.60) from Remark 1 gives

$$\int_t^{t+T} c_r^2 \mathrm{d}\tau = c_r^2 T,$$

and the right side gives

$$\begin{aligned} \left[\int_t^{t+T} c_r \sin(\tau) \mathrm{d}\tau \right]^2 &= c_r^2 (\cos(t) - cos(t+T))^2 \\ &\leq 4 c_r^2, \end{aligned}$$

such that for $T > 4$,

$$c_r^2 T > \left[\int_t^{t+T} c_r \sin(\tau) \mathrm{d}\tau \right]^2 = c_r^2 (\cos(t) - cos(t+T))^2, \tag{4.64}$$

and PE is satisfied.

The discussion above in concluded in Theorem 4 below.

Theorem 4. *The adaptive observer design of (4.42) and (4.48) is globally asymptotically stable if Proposition 2 is satisfied.*

4.3 MRU

A MRU (Seatex, 2014) allows for the measuring of the body fixed accelerations (linear and angular) at the placement of the MRU, and by differentiating Equation (4.2) for the GNSS

equation twice a similar type of equations can be obtained for the acceleration, written as

$$\boldsymbol{A}_1 = \boldsymbol{A}_0 + \boldsymbol{R}(\boldsymbol{\Theta})\boldsymbol{S}(\boldsymbol{\omega})^2\boldsymbol{l}_1 + \boldsymbol{R}(\boldsymbol{\Theta})\boldsymbol{S}(\dot{\boldsymbol{\omega}})\boldsymbol{l}_1, \tag{4.65}$$

where $\boldsymbol{A}_1$ is the linear NED-acceleration, and $\boldsymbol{A}_0$ is the linear NED-acceleration at the reference point. The acceleration from the MRUs will have to be transformed into NED-coordinates in order to be used in the above equation, which is chosen to be in NED-coordinates to make it similar to the GNSS equation of (4.2). In the same way as for the GNSS equations of Eq. (4.2), the equations for several MRUs can be written as

$$\begin{aligned}
\boldsymbol{A}_1(t) &= \boldsymbol{A}_0(t) + \boldsymbol{R}(\boldsymbol{\Theta})\boldsymbol{S}(\boldsymbol{\omega})^2\boldsymbol{l}_1 + \boldsymbol{R}(\Theta)\boldsymbol{S}(\dot{\boldsymbol{\omega}})\boldsymbol{l}_1 \\
\boldsymbol{A}_2(t) &= \boldsymbol{A}_0(t) + \boldsymbol{R}(\boldsymbol{\Theta})\boldsymbol{S}(\boldsymbol{\omega})^2\boldsymbol{l}_2 + \boldsymbol{R}(\boldsymbol{\Theta})\boldsymbol{S}(\dot{\boldsymbol{\omega}})\boldsymbol{l}_2 \\
&\vdots \\
\boldsymbol{A}_m(t) &= \boldsymbol{A}_0(t) + \boldsymbol{R}(\boldsymbol{\Theta})\boldsymbol{S}(\boldsymbol{\omega})^2\boldsymbol{l}_m + \boldsymbol{R}(\boldsymbol{\Theta})\boldsymbol{S}(\dot{\boldsymbol{\omega}})\boldsymbol{l}_m
\end{aligned} \tag{4.66}$$

In the same manner as with the GNSS problem from Section 4.2 the rotation matrix $\boldsymbol{R}$, and the other signals, such as the angular rates, and the linear velocities are treated as input signals to the system, such that $\boldsymbol{R}(\boldsymbol{\Theta}) = \boldsymbol{R}(t)$, $\boldsymbol{S}(\boldsymbol{\omega} = \boldsymbol{S}(t)$, and $\boldsymbol{S}(\dot{\boldsymbol{\omega}}) = \dot{\boldsymbol{S}}(t)$. In this way the system is treated as a time varying linear system.

4.3.1 Luenberger observer design

Eq. (4.66) can be written on a state space form as

$$\boldsymbol{x} = \begin{bmatrix} \boldsymbol{A}_0 \\ \boldsymbol{l}_1 \\ \boldsymbol{l}_2 \\ \vdots \\ \boldsymbol{l}_m \end{bmatrix} \in \mathbb{R}^{3n}, \quad n = m + 1, \tag{4.67}$$

$$y = \begin{bmatrix} \boldsymbol{A}_{MRU1} \\ \boldsymbol{A}_{MRU2} \\ \vdots \\ \boldsymbol{A}_{MRUm} \end{bmatrix} \in \mathbb{R}^{3m}, \tag{4.68}$$

where $\boldsymbol{x}$ are the states to be estimated, and $\boldsymbol{y}$ is the output.

From Eq. (4.6)

$$\dot{\boldsymbol{P}}_{\boldsymbol{0}} = \boldsymbol{R}(t)\boldsymbol{\nu} = \boldsymbol{V}_0(t),$$

and by (time) differentiating $\boldsymbol{P}_0$ twice $\boldsymbol{A}_0$ can be found as

$$\dot{\boldsymbol{V}}_{\boldsymbol{0}} = \boldsymbol{R}(t)\boldsymbol{S}(t)\boldsymbol{\nu}(t) + \boldsymbol{R}(t)\dot{\boldsymbol{\nu}}(t) = \boldsymbol{A}_0(t), \tag{4.69}$$

$$\dot{\boldsymbol{A}}_{\boldsymbol{0}} = (\boldsymbol{R}(t)\boldsymbol{S}(t)^2 + \boldsymbol{R}(t)\dot{\boldsymbol{S}}(t))\boldsymbol{\nu}(t) + \boldsymbol{R}(t)\boldsymbol{S}(t)\dot{\boldsymbol{\nu}}(t) + \boldsymbol{R}(t)\ddot{\boldsymbol{\nu}}(t). \tag{4.70}$$

As with the GNSS-setup, the system description can be written as

$$\dot{\boldsymbol{x}} = \boldsymbol{A}\boldsymbol{x} + \boldsymbol{B}(t)\boldsymbol{u}(t), \tag{4.71}$$
$$\boldsymbol{y} = \boldsymbol{C}(t)\boldsymbol{x}, \tag{4.72}$$

where

$$\boldsymbol{A} = \boldsymbol{0}_{3n\times 3n}, \tag{4.73}$$
$$\boldsymbol{B}(t) = \begin{bmatrix} \boldsymbol{R}(t)\boldsymbol{S}(t)^2 + \boldsymbol{R}(t)\dot{\boldsymbol{S}}(t) & \boldsymbol{R}(t)\boldsymbol{S}(t) & \boldsymbol{R}(t) \\ \boldsymbol{0}_{3\times 3} & \boldsymbol{0}_{3\times 3} & \boldsymbol{0}_{3\times 3} \\ & \vdots & \\ \boldsymbol{0}_{3\times 3} & \boldsymbol{0}_{3\times 3} & \boldsymbol{0}_{3\times 3} \end{bmatrix} \in \mathbb{R}^{3n\times 3}, \tag{4.74}$$
$$\boldsymbol{u}(t) = \begin{bmatrix} \boldsymbol{\nu}(t) \\ \dot{\boldsymbol{\nu}}(t) \\ \ddot{\boldsymbol{\nu}}(t) \end{bmatrix}, \tag{4.75}$$

and

$$\boldsymbol{C}(t) = \begin{bmatrix} \boldsymbol{I}_{3\times 3} & \boldsymbol{R}(t)\boldsymbol{S}(t)^2 + \boldsymbol{R}(t)\dot{\boldsymbol{S}}(t) & \boldsymbol{0}_{3\times 3} & \cdots & \boldsymbol{0}_{3\times 3} \\ \boldsymbol{I}_{3\times 3} & \boldsymbol{0}_{3\times 3} & \boldsymbol{R}(t)\boldsymbol{S}(t)^2 + \boldsymbol{R}(t)\dot{\boldsymbol{S}}(t) & \ddots & \vdots \\ \vdots & \vdots & \ddots & \ddots & \boldsymbol{0}_{3\times 3} \\ \boldsymbol{I}_{3\times 3} & \boldsymbol{0}_{3\times 3} & \cdots & \boldsymbol{0}_{3\times 3} & \boldsymbol{R}(t)\boldsymbol{S}(t)^2 + \boldsymbol{R}(t)\dot{\boldsymbol{S}}(t) \end{bmatrix} \in \mathbb{R}^{3m\times 3n}. \tag{4.76}$$

Observability assessment

Observability will be investigated in a similar way as with the GNSS setup of Section 4.2.1, and Theorem 1 will be used. As discussed in Section 4.2.1, since the $\boldsymbol{A}(t)$ matrix of (4.73) is zero, only $\dot{\boldsymbol{C}}$, $\ddot{\boldsymbol{C}}$, and so on are relevant for the analysis. In fact, it is sufficient to include $\dot{\boldsymbol{C}}$, and this is shown by a simple example later (in Example 3).

The time derivative of $\boldsymbol{R}(t)\boldsymbol{S}(t)^2 + \boldsymbol{R}(t)\dot{\boldsymbol{S}}(t)$ gives

$$\begin{aligned} \frac{d}{dt}[\boldsymbol{R}(t)\boldsymbol{S}(t)^2 + \boldsymbol{R}(t)\dot{\boldsymbol{S}}(t)] &= \boldsymbol{R}(t)\boldsymbol{S}(t)^3 + \boldsymbol{R}(t)\dot{\boldsymbol{S}}(t)\boldsymbol{S}(t) + 2\boldsymbol{R}(t)\boldsymbol{S}(t)\dot{\boldsymbol{S}}(t) + \boldsymbol{R}(t)\ddot{\boldsymbol{S}}(t) \\ &=: \boldsymbol{R}(t)\boldsymbol{G}(t), \end{aligned} \tag{4.77}$$

and $\dot{\boldsymbol{C}}$ can be written

$$\dot{C}(t) = \begin{bmatrix} \boldsymbol{0}_{3\times 3} & \boldsymbol{R}(t)\boldsymbol{G}(t) & \boldsymbol{0}_{3\times 3} & \cdots & \boldsymbol{0}_{3\times 3} \\ \boldsymbol{0}_{3\times 3} & \boldsymbol{0}_{3\times 3} & \boldsymbol{R}(t)\boldsymbol{G}(t) & \ddots & \vdots \\ \vdots & \vdots & \ddots & \ddots & \boldsymbol{0}_{3\times 3} \\ \boldsymbol{0}_{3\times 3} & \boldsymbol{0}_{3\times 3} & \cdots & \boldsymbol{0}_{3\times 3} & \boldsymbol{R}(t)\boldsymbol{G}(t) \end{bmatrix} \in \mathbb{R}^{3m\times 3n}. \tag{4.78}$$

Then, by Theorem 1

$$\begin{bmatrix} \boldsymbol{N}_0 \\ \boldsymbol{N}_1 \end{bmatrix} = \begin{bmatrix} \boldsymbol{C} \\ \dot{\boldsymbol{C}} \end{bmatrix}$$
$$= \begin{bmatrix} \boldsymbol{I}_{3\times3} & \boldsymbol{R}(t)\boldsymbol{S}(t)^2 + \boldsymbol{R}(t)\dot{\boldsymbol{S}}(t) & \boldsymbol{0}_{3\times3} & \cdots & \boldsymbol{0}_{3\times3} \\ \boldsymbol{I}_{3\times3} & \boldsymbol{0}_{3\times3} & \boldsymbol{R}(t)\boldsymbol{S}(t)^2 + \boldsymbol{R}(t)\dot{\boldsymbol{S}}(t) & \ddots & \vdots \\ \vdots & \vdots & \ddots & \ddots & \boldsymbol{0}_{3\times3} \\ \boldsymbol{I}_{3\times3} & \boldsymbol{0}_{3\times3} & \cdots & \boldsymbol{0}_{3\times3} & \boldsymbol{R}(t)\boldsymbol{S}(t)^2 + \boldsymbol{R}(t)\dot{\boldsymbol{S}}(t) \\ \boldsymbol{0}_{3\times3} & \boldsymbol{R}(t)\boldsymbol{G}(t) & \boldsymbol{0}_{3\times3} & \cdots & \boldsymbol{0}_{3\times3} \\ \boldsymbol{0}_{3\times3} & \boldsymbol{0}_{3\times3} & \boldsymbol{R}(t)\boldsymbol{G}(t) & \ddots & \vdots \\ \vdots & \vdots & \ddots & \ddots & \boldsymbol{0}_{3\times3} \\ \boldsymbol{0}_{3\times3} & \boldsymbol{0}_{3\times3} & \cdots & \boldsymbol{0}_{3\times3} & \boldsymbol{R}(t)\boldsymbol{G}(t) \end{bmatrix}. \tag{4.79}$$

By the same argument as in Section 4.2.1 the observability requirement is that there has to exists a time t_1 where rank $[\boldsymbol{G}(t)] = 3$. This is summarized in the proposition below.

Proposition 3. *For the system of Eq. (4.71) and (4.72) to be observable at time t_0, there have to exist a time $t_1 > t_0$ where*

$$\textit{rank}[\boldsymbol{S}(t)^3 + \dot{\boldsymbol{S}}(t)\boldsymbol{S}(t) + 2\boldsymbol{S}(t)\dot{\boldsymbol{S}}(t) + \ddot{\boldsymbol{S}}(t)] = 3$$

Example 3. *For a constant yaw rate $r = 1$, $\dot{p} = 0.1$, and $\dot{r} = 0.1$, and p, q, $\dot{q}$, $\ddot{p}$, $\ddot{q}$, $\ddot{r} = 0$ at t_1, and , $\boldsymbol{G}(t)$ (Eq. (4.77) becomes*

$$\boldsymbol{G}(t) = \begin{bmatrix} -0.3 & 1 & 0.2 \\ -1 & -0.3 & -0.1 \\ 0.1 & 0 & 0 \end{bmatrix}$$

which has full rank, so the system is observable at t_0 for this excitation.

4.3.2 Observer equations and stability

Given the observer dynamics below

$$\dot{\hat{\boldsymbol{x}}} = \boldsymbol{B}(t)\boldsymbol{u}(t) + \boldsymbol{W}\boldsymbol{C}(t)^\top \tilde{\boldsymbol{y}} \tag{4.80}$$
$$= \boldsymbol{B}(t)\boldsymbol{u}(t) + \boldsymbol{W}\boldsymbol{C}(t)^\top \boldsymbol{C}(t)\tilde{\boldsymbol{x}}, \tag{4.81}$$

the error dynamics is given as

$$\tilde{\boldsymbol{x}} = -\boldsymbol{W}\boldsymbol{C}(t)^\top \boldsymbol{C}(t)\tilde{\boldsymbol{x}}, \tag{4.82}$$

which is similar to the error dynamics of the observer of Section 4.2.1. Therefore, following the same approach as Section 4.2.1, if if Proposition 3 is satisfied, exponential stability is concluded.

4.4 Case studies

Although the theoretical foundation derived above guarantees convergence of the lever arms for the various designs under the stated assumptions, it does not evaluate performance and robustness. To shed light on this, case studies are performed for the GNSS and the MRU lever arm estimation. Data from sea trials with R/V Gunnerus is used for the case studies.

For the GNSS lever arms two different case studies are performed for both the Luenberger observer, and the adaptive design. In the first case study the GPS data is simulated, using sea trial data. That is, the linear velocity, and Euler angles (Fossen, 2011) from the sea trial are used, and the GPS data is simulated based on that data (see Section 4.4.1). The reason GPS data is simulated, is to avoid signal synchronization and consistency issues in the input data. For the second case study the actual GPS data from the experiment is used.

For the MRU lever arm estimation one case study is performed. That is with the Luenberger observer of Section 4.3.2 on experimental data. All observer gains are found by trial and error.

4.4.1 Case studies - GNSS (GPS) lever arms

Gunnerus data In the August sea trials three turning maneuvers were performed. Two of them has a constant yaw rate, but with different rates, and the last one has a varying yaw rate. The intention was to use these maneuvers for lever arm verification. Unfortunately, the GPS measurements from MARINTEK are poor during those maneuvers(low resolution), and only the DP system GPS measurements are available. Since only one GPS measurement series is available for these maneuvers, a turning circle performed by MARINTEK is used instead. This still only gives one GPS measurement series, but all the other signals used (angular rates and linear velocities) are collected from MARINTEK measurements, so this reduce the problem of synchronization issues, since all the data is collected from the same source.

For the GPS case studies, data from a ”turning circle” (Fossen, 2011) maneuver is applied. The vessel turns with a constant rudder angle of 20 degrees on the rudders. The maneuver was performed by MARINTEK in the November sea trials. The GPS measurements available are the MARINTEK measurements, and the values for roll, pitch, and yaw rate from this maneuver are shown in Figure 4.1 below. The roll and pitch rates oscillate about a zero mean, whereas the yaw rate oscillates around a nonzero mean.

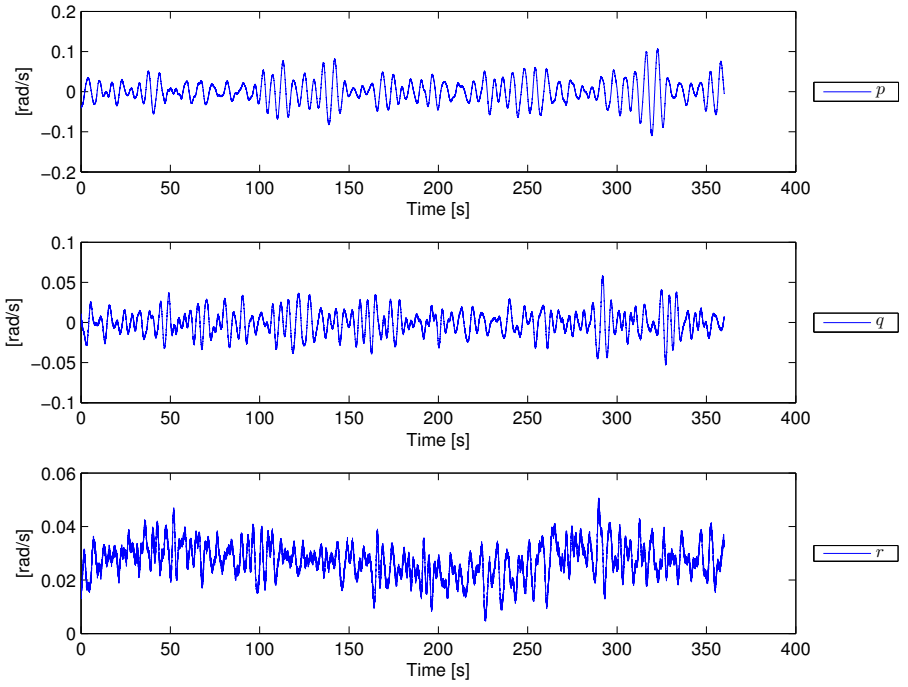

(a)

Figure 4.1: Plot of p, q, and r for GPS case study

Installed GPS antennas With the standard coordinate system used for ship navigation (Fossen, 2011) (x (pos forward), y (positive sb., z (pos down), the GPS antenna from the DP system, and the GPS antennas used by the seapath have the following coordinates, measured by surveillance (Parker, 2013).

Table 4.1: GPS coordinates

Antenna	**Coordinates**		
	x [m](pos fwd)	y [m](pos stb)	z [m](pos down)
GPS DP	0.202	-0.611	-13.891
Seapath fwd	1.571	0.691	-13.520
Seapath aft	-0.924	0.574	-13.567

R/V Gunnerus had 3 GPS antennas installed during the sea trials, but only two measurement series are available from the data. One from the DP system, and one from MARINTEK (Seapath).

Case study 1 - Simulated GPS data

In the first case study the GPS data for two GPS antennas are simulated. The simulations are done with experimental data for Θ and ν, and the GPS data is generated from Eq. (4.2)

$$\boldsymbol{P}_{GPSi} = \boldsymbol{P}_0 + \boldsymbol{R}(t)\boldsymbol{l}_i, \tag{4.83}$$

where $\boldsymbol{P}_0$ is found from integration of (Eq. (4.6))

$$\dot{\boldsymbol{P}}_0 = \boldsymbol{R}(t)\boldsymbol{\nu}. \tag{4.84}$$

Lever arms with coordinates as "seapath fwd", and "seapath aft" from Table 4.1 are added in Eq. (4.83). The initial condition of the estimated arm coordinates are

$\begin{bmatrix}1.0m & 0.3m & -13.0m\end{bmatrix}^\top$, and $\begin{bmatrix}-0.5m & 0.9m & -14.0m\end{bmatrix}^\top$. Simulation results for the Luenberger, and the adaptive observer are shown below.

Luenberger observer results The lever arm convergence results are shown below in Figure 4.2 and 4.3, and Table 4.2 summerize the results. The estimation of $\boldsymbol{P}_0$ is shown in Figure 4.4 where a North-East plot is shown. The estimated $\boldsymbol{P}_0$-values are initialized at the correct value of $\boldsymbol{P}_0$, so the estimated and measured $\boldsymbol{P}_0$ values are very similar during the entire simulation.

The gains used in the simulation are

$$\boldsymbol{W} = \begin{bmatrix} \boldsymbol{W}_1 & \boldsymbol{0}_{3\times3} & \boldsymbol{0}_{3\times3} \\ \boldsymbol{0}_{3\times3} & \boldsymbol{W}_2 & \boldsymbol{0}_{3\times3} \\ \boldsymbol{0}_{3\times3} & \boldsymbol{0}_{3\times3} & \boldsymbol{W}_2 \end{bmatrix}, \tag{4.85}$$

where

$$\boldsymbol{W}_1 = \boldsymbol{I}_{3\times3}, \tag{4.86}$$

$$\boldsymbol{W}_2 = \begin{bmatrix} 1.8 & 0 & 0 \\ 0 & 1.8 & 0 \\ 0 & 0 & 1.5 \end{bmatrix}. \tag{4.87}$$

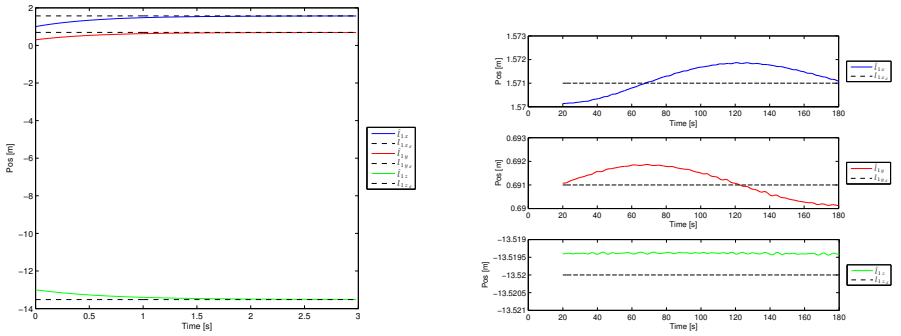

(a) **(b)**

Figure 4.2: Lever arm coordinates, l_1, observer, simulated GPS data

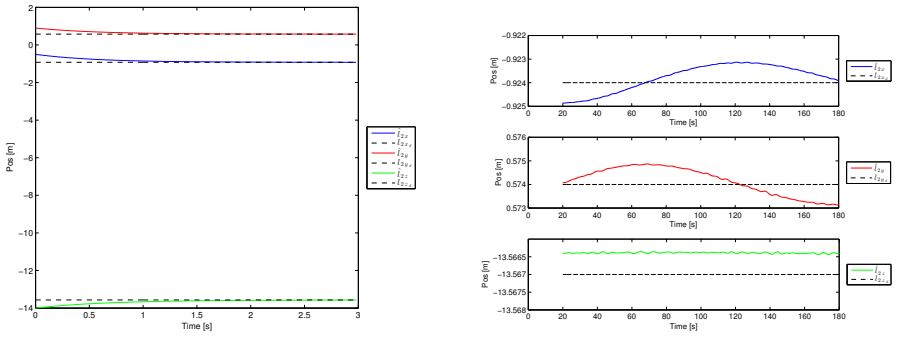

(a) **(b)**

Figure 4.3: Lever arm coordinates, l_2, observer, simulated GPS data

Table 4.2: Results, lever arm - observer, simulated GPS data

Lever arm	**Lever arm coordinates**						**Collected from interval**
	x [m]		y [m]		z [m]		
	Avg	*Std.* $[10^{-4}]$	*Avg*	*Std.* $[10^{-4}]$	*Avg*	*Std.* $[10^{-5}]$	
1	1.5712	5.6065	0.6912	5.8248	-13.5194	1.5667	20 - 180 [s]
2	-0.9238	5.6065	0.5742	5.8248	-13.5664	1.5667	20 - 180 [s]

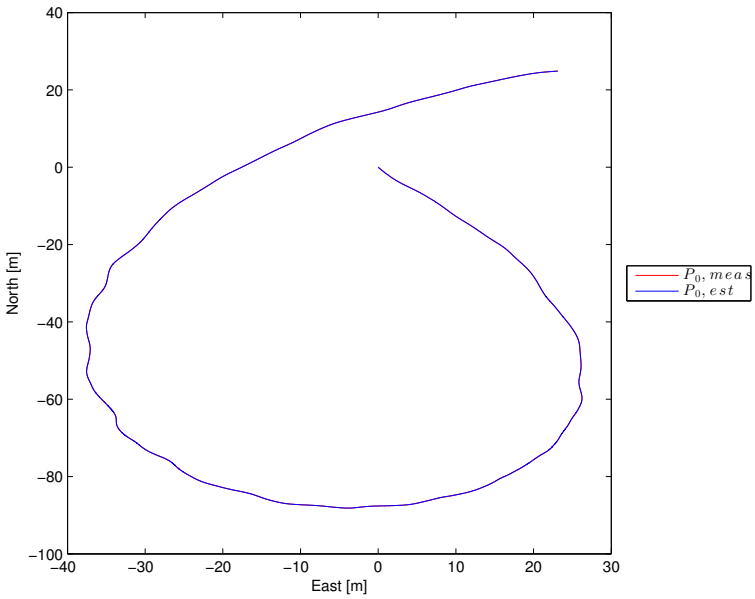

(a)

Figure 4.4: NE plot of P_0, observer

Adaptive observer results The gains used by the adaptive observer are

$$\boldsymbol{\Gamma} = diag\{45, 35, 80, 45, 35, 80\} \times 1000, \tag{4.88}$$

$$\boldsymbol{L} = 1000\boldsymbol{I}_{6\times 6}. \tag{4.89}$$

The initialization of the lever arms are similar for the Luenberger, and adaptive observer, but the adaptive observer is tuned quite high such that it has a large deviation at the beginning. As seen from Figure 4.5 and 4.6, and Table 4.3 lever arms converge quite well, but with higher standard deviations than the Luenberger observer.

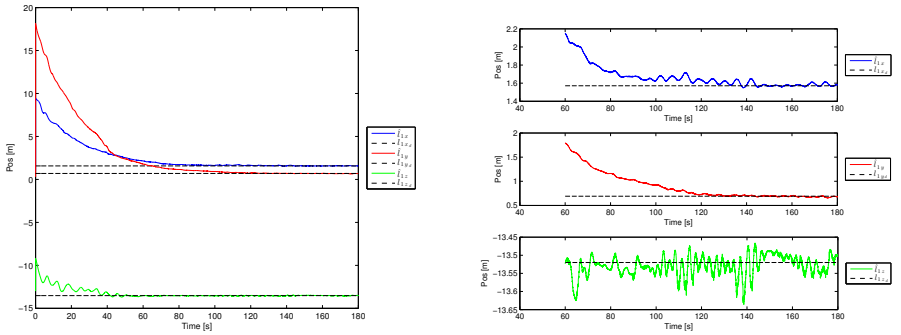

(a) **(b)**

Figure 4.5: Lever arm coordinates, l_1, adaptive, simulated GPS data

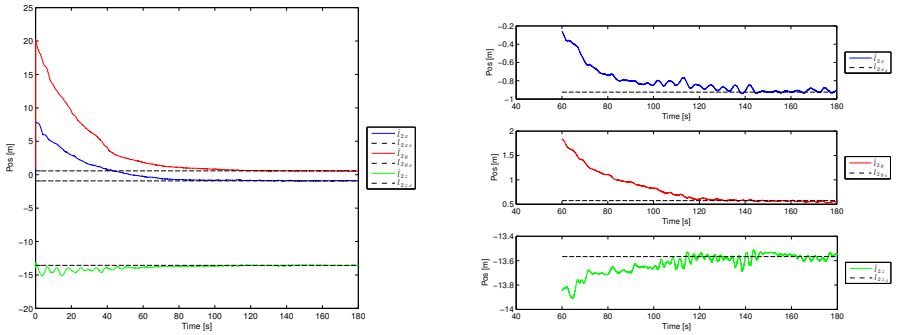

(a) **(b)**

Figure 4.6: Lever arm coordinates, l_2, adaptive, simulated GPS data

Table 4.3: Results, lever arm - adaptive, simulated GPS data

Lever arm	**Lever arm coordinates**						**Collected from interval**
	x [m]		y [m]		z [m]		
	Avg	*Std.*	*Avg*	*Std.*	*Avg*	*Std.*	
1	1.5787	0.0137	0.6842	0.0108	-13.5169	0.0205	150 - 180 [s]
2	-0.9132	0.0143	0.559	0.0116	-13.5636	0.0206	150 - 180 [s]

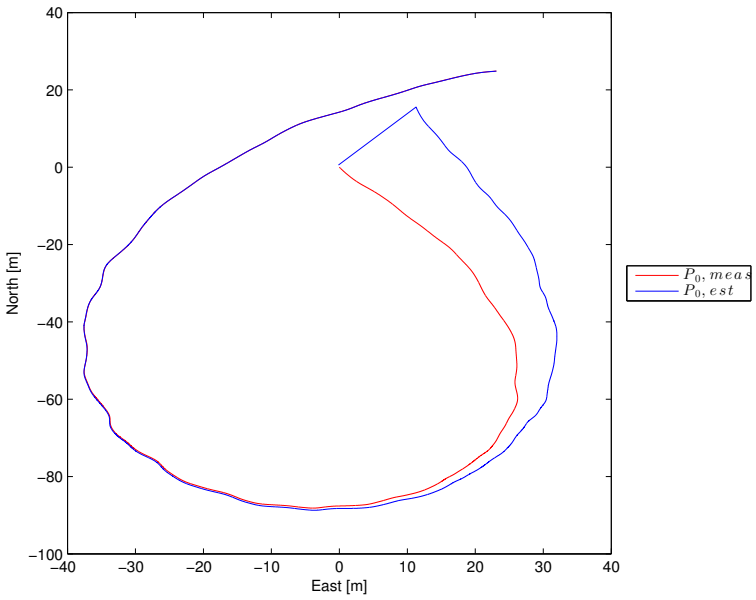

(a)

Figure 4.7: NE plot of P_0, adaptive observer

Case study 2 - Experimental GPS data

For this case study experimental GPS data is used. As mentioned in the beginning of Section 4.4.1 only one GPS measurement series is available, so only one lever arm will be estimated. The GPS data is expected to be translated to a chosen point in the vessel (a chosen $\boldsymbol{P}_0$), such that at least the lever arm coordinate in y and z-direction should converge to zero, but not necessarily in x-direction, if the chosen P_0 does not coincide with the rotation point of the vessel.

Luenberger observer results The initial conditions of the lever arm estimate are set as $\begin{bmatrix} 3.0m & 2.0m & -3.0m \end{bmatrix}^\top$.

The gains used in the simulation are

$$\boldsymbol{W} = \begin{bmatrix} \boldsymbol{W}_1 & \boldsymbol{0}_{3\times3} \\ \boldsymbol{0}_{3\times3} & \boldsymbol{W}_2 \end{bmatrix}, \tag{4.90}$$

where

$$\boldsymbol{W}_1 = 0.003\boldsymbol{I}_{3\times3}\times, \tag{4.91}$$
$$\boldsymbol{W}_2 = diag\{0.012, 0.0084, 0.012\}. \tag{4.92}$$

The lever arm convergence is shown in Figure 4.8, and values for x and z-coordinate averages are given in Table 4.4.

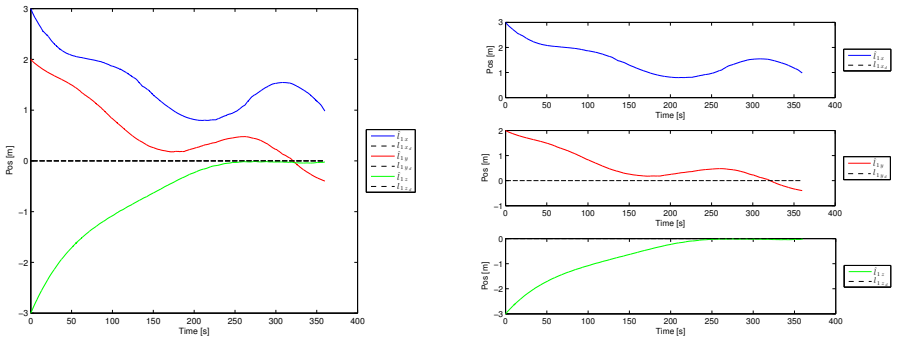

(a) **(b)**

Figure 4.8: Lever arm coordinates, l_1, observer, experimental GPS data

Table 4.4: Results, lever arm - observer, experimental GPS data

Lever arm	**Lever arm coordinates**						**Collected from interval**
	x [m]		y [m]		z [m]		
	Avg	*Std.*	*Avg*	*Std.*	*Avg*	*Std.*	
1	1.17	0.26	—	—	-0.05	0.05	130-360 [s] (x), 200-380 [s] (z)

The y-coordinate values are omitted in Table 4.4. The y-coordinate oscillates about zero, but it is not very clear. Higher tuning of the observer give more noise, but it is reasonable to assume that the y-value it should converge to is close to zero. Also, for the x-coordinate, it is difficult to precisely know the value it should converge to, but it appears to be close to 1.

Adaptive observer results The initial conditions of the lever arm estimate are set as $\begin{bmatrix} 3.0m & 2.0m & -1.0m \end{bmatrix}^\top$.

The gains used by the adaptive observer are

$$\boldsymbol{\Gamma} = diag\{1, 1.2, 15\}, \tag{4.93}$$

$$\boldsymbol{L} = diag\{0.1, 0.1, 0.01\}. \tag{4.94}$$

The lever arm convergence is shown in Figure 4.9, and values for x and y-coordinate averages are given in Table 4.5.

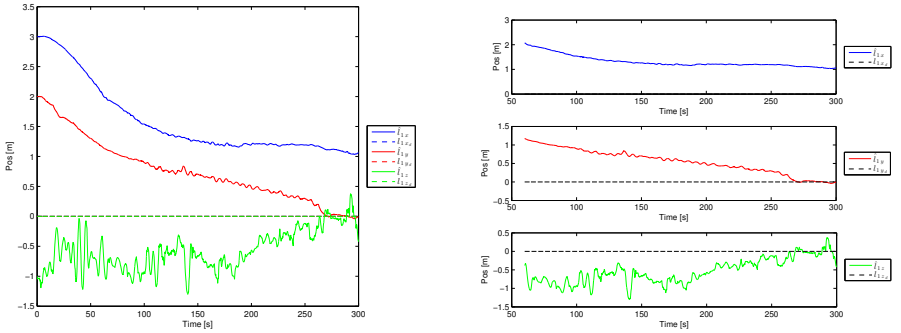

(a) **(b)**

Figure 4.9: Lever arm coordinates, l_1, adaptive, experimental GPS data

Table 4.5: Results, lever arm - adaptive, experimental GPS data

Lever arm	**Lever arm coordinates**						**Collected from interval**
	x [m]		y [m]		z [m]		
	Avg	*Std.*	*Avg*	*Std.*	*Avg*	*Std.*	
1	1.17	0.05	-0.003	0.02	—	—	170-300 [s] (x), 280-300 [s] (y)

The $\mathbf{\Gamma}$ matrix need high tuning in y and z to have convergence within the time of the maneuver performed. Convergence is the z-coordinate is not good. As with the Luenberger Observer result the x-coodinate seemingly converges to a value around 1.

The y-coordinate seems to converge, from Figure 4.9, but after $300s$, the value for y goes away from zero, possibly due to low excitation in the interval after 300 seconds.

Simulated vs recorded GPS data

The plot in Figure 4.10 and show the north and east data for simulated, and recorded GPS data. The data is simulated without any added lever arm. That is, the simulated GPS data is the simulated $\boldsymbol{P}_0$. The plots are quite similar, but at some parts they deviate a lot, especially around 300-350s for north.

The x-coordinate of the lever arm in case study 2 on recorded GPS data (Section 4.4.1) indicate that the x-coordinate could be close to 1. Because of this, a second plot is shown in Figure 4.11, where the simulated GPS data now have a lever arm of $1m$ in x-direction, and zero in y- and z-direction. Still, the differences of the data are present.

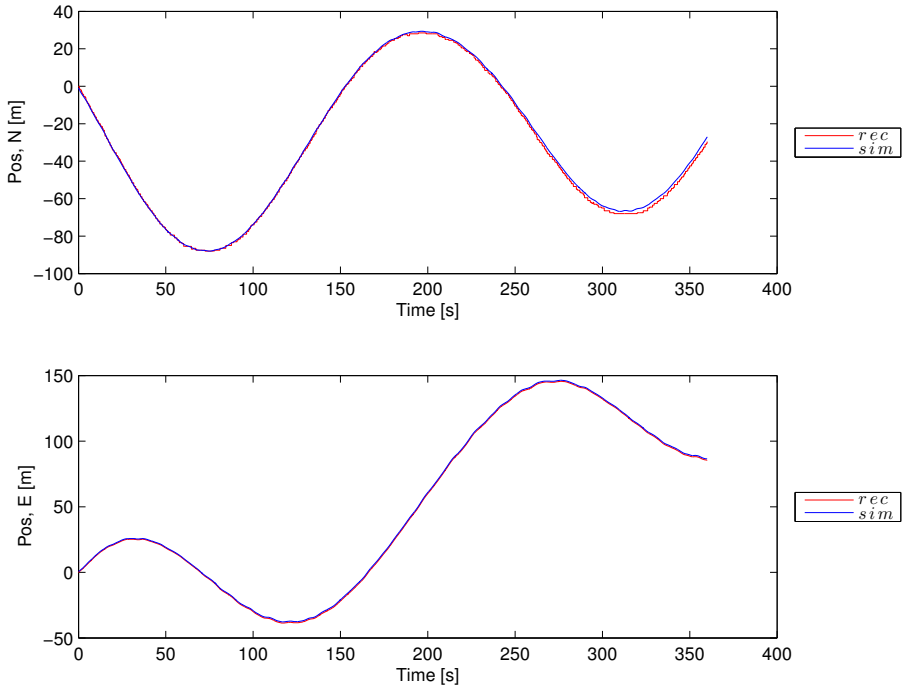

Figure 4.10: Comparison between recorded and simulated GPS data, no added arm

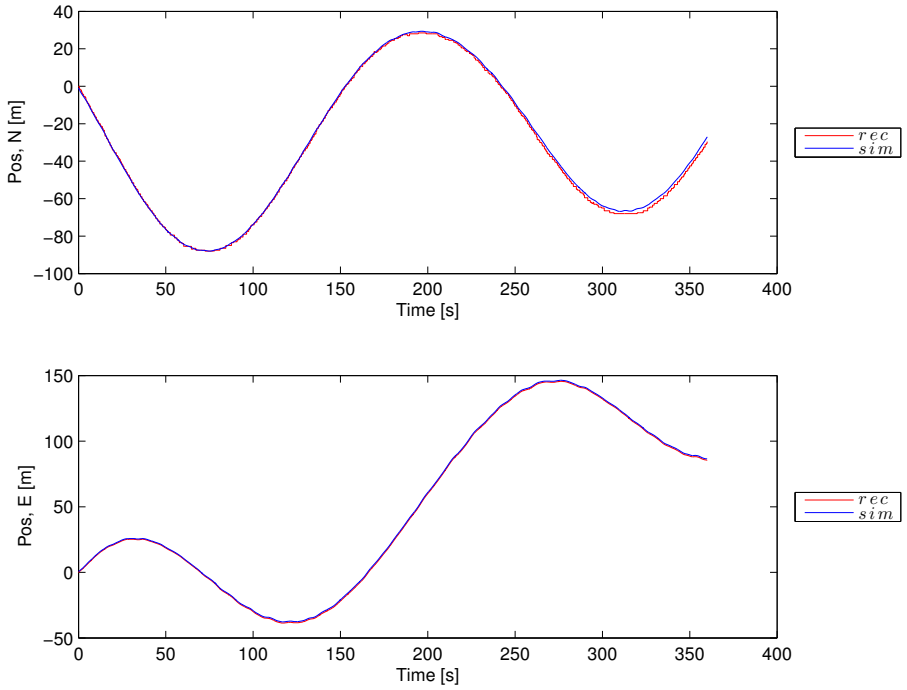

Figure 4.11: Comparison between recorded and simulated GPS data, added arm

4.4.2 Case study: MRU lever arms - Gunnerus data

The data used for the MRU case study is different from the one used for the GPS case studies. The reason for this is the update rate of the MARINTEK data. In August MARINTEK logs with an update rate of $100Hz$, and the MRUs also operate at $100Hz$, whereas in November MARINTEK logs with $50Hz$. The GPS has an update rate of $1Hz$, so it does not matter whether data from November or August is used, but for the MRUs a higher update rate is desirable. The data series that is used is one of the maneuvers intended for lever arm estimation. However, this maneuver is shorter than the one used for the GPS case studies.

The values for p, q, and r are shown in Figure 4.12. The yaw rate r appears to be somewhat constant, but it is higher than for the GPS case study of Section 4.4.1.

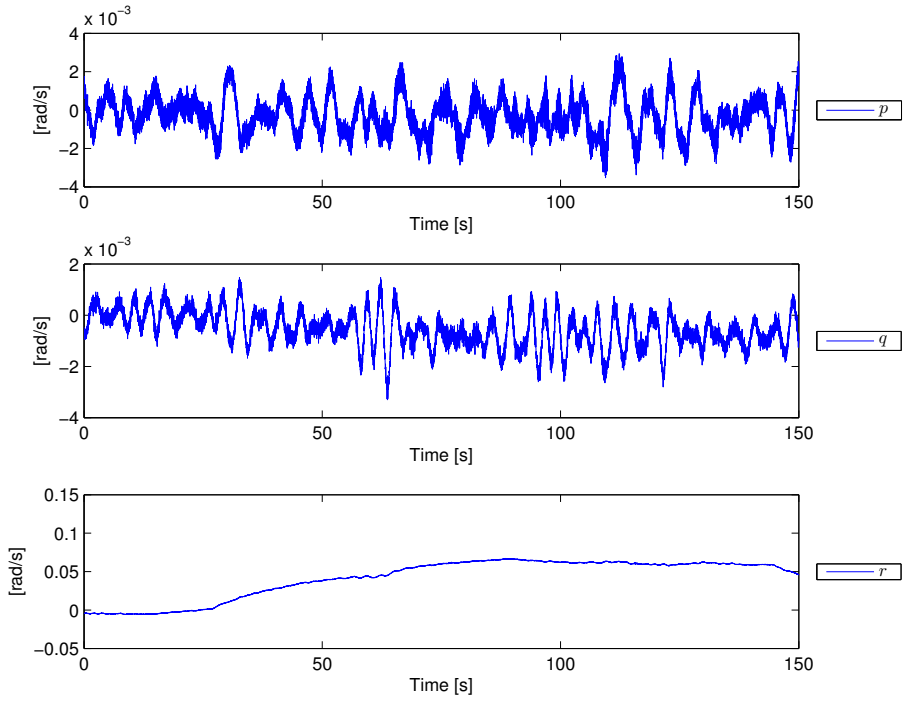

(a)

Figure 4.12: Plot of p, q, and r for MRU case study

Experimental measurements from MRU's in Gunnerus are used, and the acceleration measurements are transformed to NED-frame. There are no measurements of $\dot{\nu}$, and $\ddot{\nu}$ available. The values for $\dot{\nu}$ are found from Eq. (4.69) as

$$\dot{\boldsymbol{\nu}} = \boldsymbol{R}^{\top} \boldsymbol{A}_0 - \boldsymbol{S}\boldsymbol{\nu}, \tag{4.95}$$

and the value of $\ddot{\boldsymbol{\nu}}$ will be neglected from the observer equations in the case study.

Installed MRU's

There were 4 MRU's installed in R/V Gunnerus at the time of the sea trials, and in the case study data from two of them will be used. The lever arms of those two MRU's are given in Table (4.6) below. measured by surveillance (Parker, 2013).

Table 4.6: MRU coordinates

Antenna	**Coordinates**		
	x [m](pos fwd)	y [m](pos stb)	z [m](pos down)
MRU 1	0.358	0.804	4.321
MRU 2	14.978	0.039	0.568

Luenberger observer results

MRU accelerations from MRU's with lever arms of coordinates

$$\begin{bmatrix} 0.358m & 0.804m & -4.321m \end{bmatrix}^\top,$$

and

$$\begin{bmatrix} 14.978m & 0.039m & 0.568m \end{bmatrix}^\top,$$

are used. The initial condition of the estimated arm coordinates are $\begin{bmatrix} 30m & 30m & -30.0m \end{bmatrix}^\top$, and $\begin{bmatrix} 30m & 30m & 30m \end{bmatrix}^\top$.

The gains used in the simulation are

$$\boldsymbol{W} = \begin{bmatrix} \boldsymbol{W}_1 & \boldsymbol{0}_{3\times 3} \\ \boldsymbol{0}_{3\times 3} & \boldsymbol{W}_2 \end{bmatrix}, \tag{4.96}$$

where

$$\boldsymbol{W}_1 = \boldsymbol{I}_{3\times 3} \tag{4.97}$$

$$\boldsymbol{W}_2 = diag\{1, 0.8, 2\} \times 40000. \tag{4.98}$$

The results of the observer are shown in Figure 4.13.

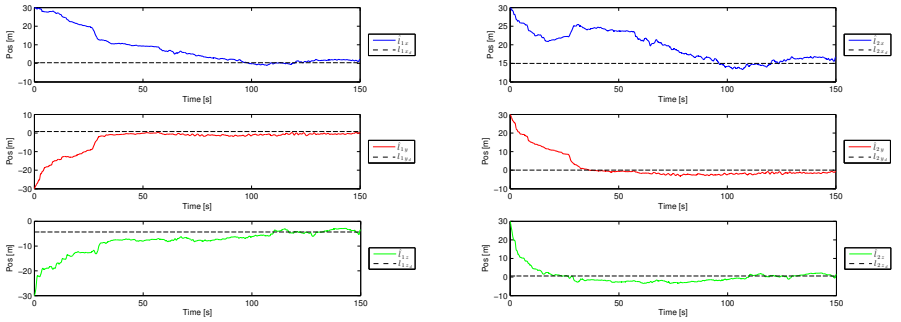

Figure 4.13: Lever arm coordinates l_1 (a), and l_2 (b) MRU case study

4.5 Conclusions and further work

For the GPS case studies where GPS data is simulated it can be seen from Section 4.4.1 that the lever arms and $\boldsymbol{P}_0$ are clearly observable (and the adaptive observer is PE). Both

observers have convergence in the lever arms, and the maneuver is sufficient for observability. The z-coordinate in the Luenberger observer have a (small) steady state offset, but this coordinate seems to converge for the adaptive observer, although it is a bit noisy.

For the GPS case studies where the recorded GPS data is used both for the Luenberger and the adaptive observer the lever arms converge close to the expected value. This becomes clear when the lever arm estimates are initialized far from the expected value. However, where the estimates of the lever arms were very accurate for the simulated GPS data, they are quite inaccurate for the experimental GPS data.

This inaccuracy could be explained by the difference in the simulated, and the experimental GPS data, as shown in Figure 4.10 and 4.11. There are small deviations between the GPS values, and this could be enough for the algorithms to become less accurate.

From Figure 4.13 is observed that the MRU estimation problem is observable. The lever arms converge quite well, and is better than the GPS lever arms when using experimental data. This is probably due to the fact that the MRU's have an update rate of $100Hz$, whereas the GPS has an update rate of $1Hz$.

For both the GPS and MRU case studies it would be interesting with a longer maneuver, such that both observer algorithms could have time to converge with lower tuning. It could also be interesting to look into the differences between the simulated GPS data, and the actual.

For the GPS case study on experimental GPS data the x-coordinate of the lever arm seemingly converges to a value close to $1m$ for both the Luenberger, and the adaptive observer. It is difficult to say whether this is the case, because these results change slightly depending on the tuning of the observers. This again motivates a longer maneuver such that low tuning can be used on both the observer designs, and more certain results can be obtained.

Chapter 5

Hybrid integral action for DP

5.1 Introduction

5.1.1 Motivation

The motivation behind the hybrid integral action proposed in the following chapter is a Dynamically Positioned (DP) marine vessel experiencing large unknown disturbances. DP vessels normally experience wave loads, wind loads, and current. The loads that the integral action part of the controller normally compensate for are slowly varying forces, almost constant for given periods of time. Because of this, the integral action is normally tuned very low, such that it does not induce unnecessary oscillation.

However, if the vessel experiences sudden load changes such as ice loads, or a mooring line that snaps, the integral action spends a long time (about 20 minutes) reaching the new steady state value. This chapter proposes a method that improves the convergence for the integral action when it is subject to large sudden disturbances that are constant some time after impact. The proposed method augments the standard PID controller with a hybrid integral action law.

5.1.2 Literature review

In El Rifai and El Rifai (2009), hybrid resetting of integral action for a PID controller is discussed. Based on the sign of the position state and the integral state, the integral action value is reset if they are of opposite sign, thereby reducing transient behavior of the closed loop plant. For Prieur et al. (2012) a hybrid high-gain observer is constructed to reduce the peaking behavior of the observer on a second order planar nonlinear system. Trajectories with peaking are projected into areas without peaking behavior.

A framework with several continuous controller and observer-pairs are proposed for hybrid control of DP vessels in Nguyen et al. (2007). The operational window of a DP vessel is extended by switching to different observer-controller pairs depending on the sea state. This approach could have been used to augment the plant with a controller with a high gain for the continuous integral action, and then switching back to a controller with lower integral action gains when the integral error is small.

The method of El Rifai and El Rifai (2009) is similar to that of the following chapter in that it uses the sign of the integral value and the states to determine when jumps can occur. However, the goal of the following chapter is to use information about the states to update the integral value, not only reset the integral value when the signs changes. This will be especially useful when large constant disturbances should quickly be compensated for by integral action.

5.1.3 Scope

The objective of the chapter is to improve performance of the PID controller when a system is subject to large disturbance changes that remain constant for some time (step disturbance). A PID-controller is augmented with a hybrid (Goebel et al., 2012) integral action law that changes the integral action value at discrete instances (jumps). When the absolute value of the error in states are small, jumps are no longer allowed. This discrete change in integral action value allows higher convergene of the integral action, with no, or small overshoot. This will be developed for both a first order linear system, and a DP system.

Section 5.2 considers the mathematical modeling. Section 5.2.1 the preliminaries for hybrid control theory and the Lyapunov stability theory needed is summarized. The stability conditions is then derived for both the first order system (Section 5.2.2), and the DP system (Section 5.2.3). In these sections a theorem concludes the stability conditions for the hybrid system. In Section 5.3 there are case studies for both a linear system (Section 5.3.1), and a DP system (Section 5.3.2).

5.2 Mathematical modelling

5.2.1 Preliminaries

The theory for hybrid control theory is based on Goebel et al. (2012). The benefit of the theory is that continuous and discrete dynamics can be combined, and stability can be proven. The aspects relevant for the approach of the chapter is mentioned below, but for a more in-depth analysis of hybrid control theory, it is referred to Goebel et al. (2012).

Continous dynamics, here called flow, given generally by a differential inclusion $F(x)$ is allowed on the flow set C. The discrete dynamics, here called jumps, given by the difference inclusion $G(x)$ is allowed on the jump set D. In the following only a differen-

tial equation $f(x)$, and difference equation $g(x)$ will be used instead of $F(x)$, and $G(x)$ respectively.

In order to prove stability of the systems in this paper, Theorem 3.18 of Goebel et al. (2012), using a Lyapunov function is applied. This theorem proves global uniform (pre-)asymptotic stability of the system, and requires the Lyapunov function to decrease in value for both flow and for a jump. Since the jump augmentation of the PID controller intends to improve performance, it makes sense to demand that $V(x)$ also decreases in jumps. To prove stability for a set A Theorem 3.18 in its most basic form is applied, and restated below for convenience. Please note that "pre-asymptotically stable" includes solutions not being complete (Goebel et al., 2012), and since this is of no concern for the systems considered, "pre-asymptotically stable" is the same as "asymptotically stable" for this chapter.

Theorem 5 (Goebel et al. (2012) Theorem 3.18)**.** *(Sufficient Lyapunov conditions) Let $H = (C, F, D, G)$ be a hybrid system and let $A \subset \mathrm{R}^{\mathrm{n}}$ be closed. If V is a Lyapunov function candidate for H and there exists α_1, $\alpha_2 \in K_\infty$, and a continuous positive definite function ρ such that*

$$\alpha_1(|x|_A) \leq V(x) \leq \alpha_2(|x|_A) \ \ \forall x \in C \cup D \cup G(D) \tag{5.1}$$

$$\langle V(x), f \rangle \leq -\rho(|x|_A) \ \ \forall x \in C, f \in F(x) \tag{5.2}$$

$$V(g) - V(x) \leq -\rho(|x|_A) \ \ \forall x \in D, g \in G(D) \tag{5.3}$$

then A is uniformly globally pre-asymptotically stable for H.

In the above theorem $|x|_A$ is the distance to the set A. In this paper the $\dot{V}$ notation will be used instead of $\langle V(x), f \rangle$, and for Eq. (**??**) $V(g)$ and $V(x)$ represents the value of $V(x)$ after and before a jump respectively. All stability proofs later in the chapter will use this theorem to prove stability.

About the approach

The key for the proposed hybrid integral action in Section 5.2.2, and 5.2.3 is the location of the jump set. It will be shown that when within the jump set, the proposed jump rule will guarantee decrease of the Lyapunov function. The clue is therefore to restrict the jump set to a set that will depend on the sign and size of the error in the integral value, and the sign and error in other states. By construction of the problem, the integral error (the difference between the unknown disturbance and the integral value) is unknown. Therefore, the dynamic equations will be used to find an expression for the integral error, and a new jump set will be formulated based on known states, and an estimate of a state derivative (that will be found by sampling). Flow can occur in the entire state space. The jump rule proposed is a linear jump rule, and jumps are proportional to the error in other state variables.

5.2.2 First order linear systems

In this approach a general first order system subject to an unknown constant disturbance is presented. A control law with proportional control, and integral action is proposed, and

the closed loop system dynamics is derived. Then the flow set, flow map, and the jump map are defined, before Theorem 6 defines a jump set such that the jumps always decrease the Lyapunov function. The theorem also gives conditions for stability in flow, such that the combined system is stable.

Consider the first order system with an unknown constant disturbance d as input to the system. The system is written as

$$\dot{z} = -az + d + u \tag{5.4}$$
$$\dot{d} = 0, \tag{5.5}$$

where $a > 0$. Let z_d be the desired z-value, and by selecting the control input u as

$$u = \dot{z}_d + az_d - k_p(z - z_d) - \hat{d}, \tag{5.6}$$

with $k_p > 0$, the closed loop error dynamics becomes

$$\dot{\tilde{z}} = -(a + k_p)\tilde{z} + \tilde{d} = -a'\tilde{z} + \tilde{d} \tag{5.7}$$
$$\dot{\tilde{d}} = \dot{d} - \dot{\hat{d}} = -\dot{\hat{d}} = -k_i z, \tag{5.8}$$

where $\tilde{d} = d - \hat{d}$, $a' = a + k_p > 0$.

Below the flow set, flow map, and the jump map are defined. The jump set is defined in Theorem 6. The states are defined as

$$\boldsymbol{x} = \begin{bmatrix} \tilde{z} \\ \tilde{d} \end{bmatrix} = \begin{bmatrix} x_1 \\ x_2 \end{bmatrix}. \tag{5.9}$$

.

Flow set

The flow set is the entire state space, so C is given as

$$C = \left\{ \boldsymbol{x} \in \mathrm{R}^2 \right\}. \tag{5.10}$$

Flow map

From (5.9), (5.7), and (5.8) the time derivative of the state $\dot{\boldsymbol{x}}$, or the flow map $f(\boldsymbol{x})$ is given as

$$\dot{\boldsymbol{x}} = \begin{bmatrix} \dot{\tilde{z}} \\ \dot{\tilde{d}} \end{bmatrix} = \begin{bmatrix} -a'x_1 + x_2 \\ -k_i x_1 \end{bmatrix} = \begin{bmatrix} -a' & 1 \\ -k_i & 0 \end{bmatrix} \begin{bmatrix} x_1 \\ x_2 \end{bmatrix} = \boldsymbol{A}\boldsymbol{x} = f(\boldsymbol{x}). \tag{5.11}$$

Jump map

In the proposed jump map x_1 remain the same, and x_2 is updated based on the x_1-value, such that

$$\boldsymbol{x}^+ = \begin{bmatrix} x_1^+ \\ x_2^+ \end{bmatrix} = \begin{bmatrix} x_1 \\ x_2 - \lambda x_1 \end{bmatrix} = \begin{bmatrix} 1 & 0 \\ -\lambda & 1 \end{bmatrix} \begin{bmatrix} x_1 \\ x_2 \end{bmatrix} = \boldsymbol{\Omega x} = g(\boldsymbol{x}) \tag{5.12}$$

Theorem 6. *Given a linear system with $\boldsymbol{x} \in \mathrm{R}^2$ of (5.9), the flow set C given by (5.10), and the closed loop flow map $f(\boldsymbol{x})$ given by (5.11), and jump map $g(\boldsymbol{x})$ given by (5.12), where the constants a', k_i, $\lambda > 0$, let α_1, $\alpha_2 \in \mathrm{K}_\infty$, and a Lyapunov function be given as*

$$\alpha_1(|\boldsymbol{x}|_A) \leq V(\boldsymbol{x}) = \boldsymbol{x}^\top \boldsymbol{P} \boldsymbol{x} \leq \alpha_2(|\boldsymbol{x}|_A), \tag{5.13}$$

where

$$\boldsymbol{P} = \begin{bmatrix} p_1 & p_2 \\ p_2 & p_3 \end{bmatrix} = \boldsymbol{P}^\top > 0, \tag{5.14}$$

is set such that the Lyapunov function decreases in flow. That is,

$$\dot{V}(\boldsymbol{x}) \leq -\rho(|x|_A) \;\; \forall \boldsymbol{x} \in C. \tag{5.15}$$

Let

$$\beta := 2\lambda p_3 > 0, \tag{5.16}$$
$$\gamma := \lambda^2 p_3 - 2\lambda p_2 > 0, \tag{5.17}$$
$$\varepsilon > 0, \tag{5.18}$$
$$\sigma > 0, \tag{5.19}$$

where ε and σ are constants. For the jump set given by

$$D = \left\{ \boldsymbol{x} \in \mathrm{R}^2 : |x_1| \geq \varepsilon, x_1 x_2 \geq \frac{(\gamma + \sigma)x_1^2 + \sigma x_2^2)}{\beta} \right\}, \tag{5.20}$$

then

$$V(g(\boldsymbol{x})) - V(\boldsymbol{x}) \leq -\sigma |\boldsymbol{x}|^2, \tag{5.21}$$

and by Theorem 5 the set $A = \{0, 0\}$ is uniformly globally pre-asymptotically stable for $\mathcal{H} = (C, f, D, g)$.

Proof. Consider the Lyapunov function given by (5.13). The time derivative of the Lyapunov function gives

$$\dot{V}(\boldsymbol{x}) = \left(\boldsymbol{x}^\top \boldsymbol{P} \dot{\boldsymbol{x}} + \dot{\boldsymbol{x}}^\top \boldsymbol{P} \boldsymbol{x} \right) \tag{5.22}$$
$$= \left[\boldsymbol{x}^\top (\boldsymbol{P}\boldsymbol{A} + \boldsymbol{A}^\top \boldsymbol{P}) \boldsymbol{x} \right], \tag{5.23}$$

so for

$$\boldsymbol{P}\boldsymbol{A} + \boldsymbol{A}^\top \boldsymbol{P} < 0, \tag{5.24}$$

$$\dot{V}(\boldsymbol{x}) < 0 \quad \forall \boldsymbol{x} \in C, \tag{5.25}$$

so if the matrix $\boldsymbol{P}$ is set such that $\boldsymbol{P}\boldsymbol{A} + \boldsymbol{A}^\top \boldsymbol{P} < 0$, the Lyapunov function decrease in flow.

The value of the Lyapunov function after a jump, $V(g)$ is

$$V(g) = \boldsymbol{x}^\top \boldsymbol{\Omega}^\top \boldsymbol{P} \boldsymbol{\Omega} \boldsymbol{x}, \tag{5.26}$$

such that

$$\begin{aligned} V(g) - V(\boldsymbol{x}) &= \boldsymbol{x}^\top [\boldsymbol{\Omega}^\top \boldsymbol{P} \boldsymbol{\Omega} - \boldsymbol{P}] \boldsymbol{x}, \\ &= \boldsymbol{x}^\top \begin{bmatrix} \lambda^2 p_3 - 2\lambda p_2 & -\lambda p_3 \\ -\lambda p_3 & 0 \end{bmatrix} \boldsymbol{x}. \end{aligned} \tag{5.27}$$

Expanding (5.27) gives

$$\begin{aligned} V(g) - V(\boldsymbol{x}) &= (\lambda^2 p_3 - 2\lambda p_2) x_1^2 - 2\lambda p_3 x_1 x_2, \\ &= \gamma x_1^2 - \beta x_1 x_2, \end{aligned} \tag{5.28}$$

and by inserting for (5.20) the inequality of (5.28) becomes

$$V(g) - V(\boldsymbol{x}) \leq -\sigma |\boldsymbol{x}|^2 \quad \forall \boldsymbol{x} \in D, \tag{5.29}$$

so by Theorem (5.3), uniform global pre-asymptotic stability is guaranteed. □

For Theorem 6 knowledge of the integral error is used to find the jump set. The integral error is not known, since the integral action is used to compensate for an unknown disturbance. Therefore, the results of Theorem (6) is not applicable for a practical implementation. In Remark 1, knowledge of the system dynamics is used to estimate the integral error, and to find a jump set based on x_1 and $\dot{x}_1$.

Remark 1 (Practical implementation)**.** *For a practical implementation of Theorem 6, the jump set D can not depend on x_2. From the flow map of (5.11) $x_1 x_2$ can be written as*

$$x_1 x_2 = a' x_1^2 + x_1 \dot{x}_1, \tag{5.30}$$

such that the jump set of (5.20) can be rewritten as

$$D = \left\{ \boldsymbol{x} \in \mathrm{R}^2 : |x_1| \geq \varepsilon, x_1 \dot{x}_1 \geq \frac{(\gamma + \sigma - a'\beta) x_1^2 + \sigma x_2^2)}{\beta} \right\}. \tag{5.31}$$

The value of σ can be set arbitrarily small, such that Eq. (5.31) does in practice not depend on the value of x_2.

5.2.3 DP system

Similar to the first order system, a closed loop system with integral action in the controller will be derived. Then the flow set, flow map, and jump map are defined. Thereafter Theorem 7 will define stability of the system by specifying a jump set that depends on the states of the system.

Consider the linearized DP system of Section 2.1.4, that has kinematics and kinetics given as

$$\dot{\boldsymbol{\eta}} = \boldsymbol{R}(\psi)\boldsymbol{\nu}, \tag{5.32}$$

$$\boldsymbol{M}\dot{\boldsymbol{\upsilon}} = -\boldsymbol{D}\boldsymbol{\nu} + \boldsymbol{R}(\psi)^\top \boldsymbol{b} + \boldsymbol{\tau}, \tag{5.33}$$

$$\dot{\boldsymbol{b}} = 0, \tag{5.34}$$

where $\boldsymbol{b}$ is considered a constant disturbance or bias force (from Eq. (5.34)), and the linear damping matrix satisfies $\boldsymbol{D} > 0$, and the mass matrix is assumed to have the following properties $\boldsymbol{M} = \boldsymbol{M}^\top > 0$, and $\dot{\boldsymbol{M}} = \boldsymbol{0}$. The system now contain a rotation matrix, making it nonlinear. However, the jump map used will be linear, and similar to the approach used in Section 5.2.2.

By using a backstepping approach with integral action (Skjetne and Fossen, 2004), the x-variables can be defined as

$$\boldsymbol{x} = \begin{bmatrix} \boldsymbol{R}^\top \tilde{\boldsymbol{\eta}} \\ \boldsymbol{\nu} - \boldsymbol{\mu}(\boldsymbol{\eta}, t) \\ \tilde{\boldsymbol{b}} \end{bmatrix} = \begin{bmatrix} \boldsymbol{x}_1 \\ \boldsymbol{x}_2 \\ \boldsymbol{x}_3 \end{bmatrix}, \tag{5.35}$$

where $\boldsymbol{\mu}(\boldsymbol{\eta}, t)$ is a virtual control law to be defined later. An integral state $\hat{\boldsymbol{b}}$ is augmented to the plant, and its dynamics are given as

$$\dot{\hat{\boldsymbol{b}}} = -\boldsymbol{K}_i \boldsymbol{R}(\psi)\boldsymbol{x}_2, \tag{5.36}$$

with $\boldsymbol{K}_i = \boldsymbol{K}_i^\top > 0$. The other variables are defined as $\tilde{\boldsymbol{\eta}} = \boldsymbol{\eta} - \boldsymbol{\eta}_d$, $\tilde{\boldsymbol{b}} = \boldsymbol{b} - \hat{\boldsymbol{b}}$, where $\boldsymbol{\eta}_d$ is the desired position, and the desired velocity is zero ($\boldsymbol{\nu}_d = 0$). By setting the virtual control law $\boldsymbol{\mu}(\eta, t)$ as

$$\boldsymbol{\mu}(\boldsymbol{\eta}, t) = -\boldsymbol{K}_p \boldsymbol{x}_1 + \boldsymbol{R}(\psi)^\top \dot{\boldsymbol{\eta}}_d, \tag{5.37}$$

with $\boldsymbol{K}_p = \boldsymbol{K}_p^\top > 0$, and the actual control input $\boldsymbol{\tau}$ as

$$\boldsymbol{\tau} = -\boldsymbol{x}_1 - \boldsymbol{K}_d \boldsymbol{x}_2 - \boldsymbol{R}(\psi)^\top \hat{\boldsymbol{b}} + \boldsymbol{D}\boldsymbol{\nu} + \boldsymbol{M}\dot{\boldsymbol{\mu}}, \tag{5.38}$$

where $\boldsymbol{K}_d = \boldsymbol{K}_d^\top > 0$. This results in the closed loop continuous dynamics

$$\dot{\boldsymbol{x}}_1 = -r\boldsymbol{S}\boldsymbol{x}_1 - \boldsymbol{K}_p \boldsymbol{x}_1 + \boldsymbol{x}_2 \tag{5.39}$$

$$\boldsymbol{M}\dot{\boldsymbol{x}}_2 = -\boldsymbol{x}_1 - \boldsymbol{K}_d \boldsymbol{x}_2 + \boldsymbol{R}(\psi)^\top \boldsymbol{x}_3 \tag{5.40}$$

$$\dot{\boldsymbol{x}}_3 = -\boldsymbol{K}_i \boldsymbol{R}(\psi)\boldsymbol{x}_2, \tag{5.41}$$

and this is shown in Appendix A.

From the states defined in (5.35), and the continuous closed loop dynamics of (5.39 - 5.41), the flow set, the flow map, and the jump map are defined below. The jump map is defined similarly to that of Section 5.2.2, and the jump set is defined in Theorem 7.

Flow set

Flow should be allowed in the entire state space, and the flow map C is given as

$$C = \left\{ \boldsymbol{x} \in \mathrm{R}^9 \right\}. \tag{5.42}$$

Flow map

Rewriting the equations (5.39 - 5.41), the flow map $f(\boldsymbol{x})$ is given as

$$\dot{\boldsymbol{x}}_1 = -r\boldsymbol{S}\boldsymbol{x}_1 - \boldsymbol{K}_p\boldsymbol{x}_1 + \boldsymbol{x}_2 \tag{5.43}$$

$$\boldsymbol{M}\dot{\boldsymbol{x}}_2 = -\boldsymbol{x}_1 - \boldsymbol{K}_d\boldsymbol{x}_2 + \boldsymbol{R}(\psi)^\top \boldsymbol{x}_3 \tag{5.44}$$

$$\dot{\boldsymbol{x}}_3 = -\boldsymbol{K}_i\boldsymbol{R}(\psi)\boldsymbol{x}_2. \tag{5.45}$$

Jump map

For the jump map chosen the jump in integral action is proportional to $\boldsymbol{x}_2$. That is, the same state variable used in the continuous integral action.

For a constant $\lambda > 0$,

$$\boldsymbol{\Lambda} = diag\{\lambda, \lambda, \lambda\} > 0, \tag{5.46}$$

the jump map is given as

$$\boldsymbol{x}^+ = \begin{bmatrix} \boldsymbol{x}_1^+ \\ \boldsymbol{x}_2^+ \\ \boldsymbol{x}_3^+ \end{bmatrix} = \begin{bmatrix} \boldsymbol{x}_1 \\ \boldsymbol{x}_2 \\ \boldsymbol{x}_3 - \Lambda\boldsymbol{x}_2 \end{bmatrix} = \begin{bmatrix} \boldsymbol{I} & \boldsymbol{0} & \boldsymbol{0} \\ \boldsymbol{0} & \boldsymbol{I} & \boldsymbol{0} \\ \boldsymbol{0} & -\boldsymbol{\Lambda} & \boldsymbol{I} \end{bmatrix} \begin{bmatrix} \boldsymbol{x}_1 \\ \boldsymbol{x}_2 \\ \boldsymbol{x}_3 \end{bmatrix} = \boldsymbol{\Omega}\boldsymbol{e} = g(\boldsymbol{x}) \tag{5.47}$$

Theorem 7. *Given the closed loop DP system with $\boldsymbol{x} \in \mathrm{R}^9$ of (5.35), the flow set given by (5.42), and the closed loop flow map given by (5.43 - 5.45), and jump map given by (5.47), let $\boldsymbol{M} = \boldsymbol{M}^\top$, $\dot{\boldsymbol{M}} = \boldsymbol{0}$, $\boldsymbol{K}_i = \boldsymbol{K}_i^\top$, α_1, $\alpha_2 \in \mathrm{K}_\infty$, and a Lyapunov function be given as*

$$\alpha_1(|\boldsymbol{x}|_A) \leq V(\boldsymbol{x}) = \frac{1}{2}\boldsymbol{x}_1^\top\boldsymbol{x}_1 + \frac{1}{2}\boldsymbol{x}_2^\top\boldsymbol{M}\boldsymbol{x}_2 + \frac{1}{2}\boldsymbol{x}_3^\top\boldsymbol{K}_i^{-1}\boldsymbol{x}_3 \leq \alpha_2(|\boldsymbol{x}|_A), \tag{5.48}$$

such that $\dot{V}(\boldsymbol{x}) < 0, \ \ \forall x \in C$ can be shown.

Let

$$\boldsymbol{\beta} := 2\boldsymbol{\Lambda}\boldsymbol{P}_3 > 0, \tag{5.49}$$

$$\boldsymbol{\Gamma} := \boldsymbol{\Lambda}^2\boldsymbol{P}_3 - 2\boldsymbol{\Lambda}\boldsymbol{P}_2 > 0, \tag{5.50}$$

$$\varepsilon_1 > 0, \tag{5.51}$$

$$\varepsilon_2 > 0, \tag{5.52}$$

$$\sigma > 0, \tag{5.53}$$

where ε_1, ε_2, and σ are constants. For the jump set given by

$$D = \big\{\boldsymbol{x} \in \mathrm{R}^9 : |\boldsymbol{x}_1| \geq \varepsilon_1, |\boldsymbol{x}_2| \geq \varepsilon_2, \tag{5.54}$$

$$\boldsymbol{x}_2^\top \boldsymbol{K}_i^{-1}\boldsymbol{x}_3 \geq \frac{\lambda}{2}\boldsymbol{x}_2^\top \boldsymbol{K}_i^{-1}\boldsymbol{x}_2 + \frac{\sigma}{2\lambda}[\boldsymbol{x}_1^\top \boldsymbol{x}_1 + \boldsymbol{x}_2^\top \boldsymbol{x}_2 + \boldsymbol{x}_3^\top \boldsymbol{x}_3]\Big\}, \tag{5.55}$$

then

$$V(g(\boldsymbol{x})) - V(\boldsymbol{x}) \leq -\sigma|\boldsymbol{x}|^2, \tag{5.56}$$

and the set $A = \{\mathbf{0}, \mathbf{0}, \mathbf{0}\}$ is uniformly globally pre-asymptotically stable for $\mathcal{H} = (C, f, D, g)$.

Proof. Stability in flow:

The time derivative of the Lyapunov function given by (5.48) gives

$$\begin{aligned}
\dot{V}(\boldsymbol{x}) &= \boldsymbol{x}_1^\top \dot{\boldsymbol{x}}_1 + \boldsymbol{x}_2^\top \boldsymbol{M}\dot{\boldsymbol{x}}_2 + \boldsymbol{x}_3^\top \boldsymbol{K}_i^{-1}\dot{\boldsymbol{x}}_3 \\
&= \boldsymbol{x}_1^\top[-rS\boldsymbol{x}_1 - \boldsymbol{K}_p\boldsymbol{x}_1 + \boldsymbol{x}_2] + \boldsymbol{x}_2^\top[-\boldsymbol{x}_1 - \boldsymbol{K}_d\boldsymbol{x}_2 + \boldsymbol{R}(\psi)^\top \boldsymbol{x}_3] \\
&+ \boldsymbol{x}_3^\top \boldsymbol{K}_i^{-1}[-\boldsymbol{K}_i\boldsymbol{R}(\psi)\boldsymbol{x}_2] \\
&= -\boldsymbol{x}_1^\top \boldsymbol{K}_p\boldsymbol{x}_1 - \boldsymbol{x}_2^\top \boldsymbol{K}_d\boldsymbol{x}_2 \leq 0,
\end{aligned} \tag{5.57}$$

and the continuous dynamics is uniformly globally stable (UGS) (Khalil, 2002), and to proove UGAS Barbalats Lemma (Lemma (2)) is applied, since the system is time varying. The double time derivative of $V(\boldsymbol{x})$, $\ddot{V}(\boldsymbol{x})$ is

$$\ddot{\boldsymbol{V}}(\boldsymbol{x}) = -2\boldsymbol{x}_1^\top \boldsymbol{K}_p\dot{\boldsymbol{x}}_1 - 2\boldsymbol{x}_2^\top \boldsymbol{K}_d\dot{\boldsymbol{x}}_2. \tag{5.58}$$

From Eq. (5.48) it is known that $\boldsymbol{x}_1$, $\boldsymbol{x}_2$, and $\boldsymbol{x}_3$ are bounded. From Eq. (5.43) is can be seen that $\dot{\boldsymbol{x}}_1$ is bounded, and from Eq. (5.44) $\dot{\boldsymbol{x}}_2$ is bounded, and hence, $\ddot{V}(\boldsymbol{x})$ is bounded, and

$$\lim_{t\to\infty} \dot{V} = \lim_{t\to\infty} (-\boldsymbol{x}_1^\top \boldsymbol{K}_p\boldsymbol{x}_1 - \boldsymbol{x}_2^\top \boldsymbol{K}_d\boldsymbol{x}_2) = 0$$

Since $\boldsymbol{x}_2$ goes to zero as time goes to infinity, then

$$\lim_{t\to\infty} \dot{\boldsymbol{x}}_2 = 0,$$

and by Eq. (5.44)

$$\lim_{t\to\infty} \boldsymbol{x}_3 = 0,$$

and UGAS can be concluded for flow $\forall \boldsymbol{x} \in C$.
Stability in jumps:

The value of the Lyapunov function after a jump $V(g)$ is given as

$$\begin{aligned} V(g) &= \frac{1}{2}\boldsymbol{x}_1^\top \boldsymbol{x}_1 + \frac{1}{2}\boldsymbol{x}_2^\top \boldsymbol{M}\boldsymbol{x}_2 + \frac{1}{2}(\boldsymbol{x}_3 - \boldsymbol{\Lambda}\boldsymbol{x}_2)^\top \boldsymbol{K}_i^{-1}(\boldsymbol{x}_3 - \boldsymbol{\Lambda}\boldsymbol{x}_2) \\ &= \frac{1}{2}\boldsymbol{x}_1^\top \boldsymbol{x}_1 + \frac{1}{2}\boldsymbol{x}_2^\top \boldsymbol{M}\boldsymbol{x}_2 \\ &+ \frac{1}{2}[\boldsymbol{x}_3^\top \boldsymbol{K}_i^{-1}\boldsymbol{x}_3 - \boldsymbol{x}_3^\top \boldsymbol{K}_i^{-1}\boldsymbol{\Lambda}\boldsymbol{x}_2 - \boldsymbol{x}_2^\top \boldsymbol{\Lambda}^\top \boldsymbol{K}_i^{-1}\boldsymbol{x}_3 + \boldsymbol{x}_2^\top \boldsymbol{\Lambda}^\top \boldsymbol{K}_i^{-1}\boldsymbol{\Lambda}\boldsymbol{x_2}], \end{aligned} \tag{5.59}$$

such that

$$V(g) - V(\boldsymbol{x}) = -\boldsymbol{x}_3^\top \boldsymbol{K}_i^{-1}\boldsymbol{\Lambda}\boldsymbol{x}_2 - \boldsymbol{x}_2^\top \boldsymbol{\Lambda}^\top \boldsymbol{K}_i^{-1}\boldsymbol{x}_3 + \boldsymbol{x}_2^\top \boldsymbol{\Lambda}^\top \boldsymbol{K}_i^{-1}\boldsymbol{\Lambda}\boldsymbol{x_2}, \tag{5.60}$$

and since $\boldsymbol{\Lambda} = \lambda \boldsymbol{I}$,

$$V(g) - V(\boldsymbol{x}) = -2\lambda \boldsymbol{x}_2^\top \boldsymbol{K}_i^{-1}\boldsymbol{x}_3 + \lambda^2 \boldsymbol{x}_2^\top \boldsymbol{K}_i^{-1}\boldsymbol{x}_2. \tag{5.61}$$

For

$$\boldsymbol{x}_2^\top \boldsymbol{K}_i^{-1}\boldsymbol{x}_3 \geq \frac{\lambda}{2}\boldsymbol{x}_2^\top \boldsymbol{K}_i^{-1}\boldsymbol{x}_2 + \frac{\sigma}{2\lambda}[\boldsymbol{x}_1^\top \boldsymbol{x}_1 + \boldsymbol{x}_2^\top \boldsymbol{x}_2 + \boldsymbol{x}_3^\top \boldsymbol{x}_3], \tag{5.62}$$

$$V(g) - V(\boldsymbol{x}) \leq -\sigma|\boldsymbol{x}|^2 < 0. \tag{5.63}$$

As with the approach of the first order system, σ can be arbitrary small, so it does not matter that $\boldsymbol{x}_3$ is unknown.

Since UGAS can be proved for both flow and jumps, UGAS (UGpAS) for the hybrid system is concluded. □

Remark 2 (Practical implementation)**.** *For a practical implementation of Theorem 7, the jump set D can not depend on $\boldsymbol{x}_3$. From the flow map equation of (5.44) $\boldsymbol{x}_2^\top \boldsymbol{K}_i^{-1}\boldsymbol{x}_3$ can be written as*

$$\boldsymbol{x}_2^\top \boldsymbol{K}_i^{-1}\boldsymbol{x}_3 = \boldsymbol{x}_2^\top \boldsymbol{K}_i^{-1}\boldsymbol{R}(\psi)[\boldsymbol{M}\dot{\boldsymbol{x}}_2 + \boldsymbol{x}_1 + \boldsymbol{K}_d\boldsymbol{x}_2] \tag{5.64}$$

such that the jump set of (5.55) can be rewritten as

$$D = \big\{\boldsymbol{x} \in \mathrm{R}^9 : |\boldsymbol{x}_1| \geq \varepsilon_1, |\boldsymbol{x}_2| \geq \varepsilon_2, \tag{5.65}$$

$$\boldsymbol{x}_2^\top \boldsymbol{K}_i^{-1}\boldsymbol{R}(\psi)\boldsymbol{M}\dot{x}_2 \geq \frac{\lambda}{2}\boldsymbol{x}_2^\top \boldsymbol{K}_I\boldsymbol{x}_2 + \frac{\sigma}{2\lambda}[\boldsymbol{x}_1^\top \boldsymbol{x}_1 + \boldsymbol{x}_2^\top \boldsymbol{x}_2 + \boldsymbol{x}_3^\top \boldsymbol{x}_3] \tag{5.66}$$

$$-\boldsymbol{x}_2^\top \boldsymbol{K}_i^{-1}\boldsymbol{R}(\psi)[\boldsymbol{x}_1 + \boldsymbol{K}_d\boldsymbol{x}_2]\big\} \tag{5.67}$$

As in Remark 1, the value of σ can be set arbitrarily small, such that Eq. (5.67) does in practice not depend on the value of the integral state error x_3.

5.3 Case studies

5.3.1 First order linear system

For this example both the cases when knowledge of x_2 is assumed known, and when x_2 is estimated from sampling of $\dot{x}_1$ are simulated. Consider the first order system

$$\dot{z} = -z + d + u \tag{5.68}$$

$$\dot{d} = 0, \tag{5.69}$$

and control input u as

$$u = \dot{z}_d + z_d - 9(z - z_d) - \hat{d}, \tag{5.70}$$

so that the closed loop continuous dynamics becomes

$$\dot{\tilde{z}} = -10\tilde{z} + \tilde{d} \tag{5.71}$$

$$\dot{\tilde{d}} = -k_i x_1. \tag{5.72}$$

Let the state vector be given as

$$\boldsymbol{x} = \begin{bmatrix} \tilde{z} \\ \tilde{d} \end{bmatrix} = \begin{bmatrix} x_1 \\ x_2 \end{bmatrix}. \tag{5.73}$$

Typically the integral action would have a low tuning, so set $k_i = 1$, and a' is given as 10 by (5.71), so $\dot{\boldsymbol{x}}$ is written as

$$\dot{\boldsymbol{x}} = \begin{bmatrix} -10 & 1 \\ -1 & 0 \end{bmatrix} \begin{bmatrix} x_1 \\ x_2 \end{bmatrix} = \boldsymbol{A}\boldsymbol{x}, \tag{5.74}$$

and for

$$\boldsymbol{P} = \begin{bmatrix} 1 & -0.1 \\ -0.1 & 1 \end{bmatrix} \tag{5.75}$$

the condition given by (5.24) is satisfied, and the Lyapunov function decrease in flow.

For this example, the values chosen for λ, and ε are

$$\lambda = 3, \tag{5.76}$$

$$\varepsilon = 0.3, \tag{5.77}$$

such that Eq. (5.16), and (5.17) gives $\beta = 6$, and $\gamma = 9.6$, and the jump set given by (5.20) becomes

$$D = \left\{ \boldsymbol{x} \in \mathrm{R}^2 : |x_1| \geq 0.3, x_1 x_2 \geq 1.6x_1^2 + \frac{\alpha_3}{\beta}(x_1^2 + x_2^2) \right\}. \tag{5.78}$$

Note that α_3 can be arbitrary small, so it is not considered in the simulation.

The jump set for when x_2 is not assumed known, given by (5.31) becomes

$$D = \left\{ \boldsymbol{x} \in \mathrm{R}^2 : |x_1| \geq 0.3, x_1 \dot{x}_1 \geq -8.4 x_1^2 + \frac{\alpha_3}{\beta}(x_1^2 + x_2^2) \right\}. \tag{5.79}$$

For both simulations a step of magnitude 100 at time $t = 5s$, and a step of -50 at time $t = 30$ is applied.

Even though it is not necessary in terms of stability, a dwell-time (Goebel et al., 2012) (minimum amount of time between jumps) of $T = 0.1s$ is demanded between each jump in the simulations. For the simulation run with x_2 assumed known, it would work fine without a dwell time, but if ε is set small, then all jumps necessary would be performed with a magnitude $\lambda\varepsilon_2$, which could require a lot of jumps. A method without dwell-time could be computationally unfeasible. Also, a method without a dwell-time constraint could be less robust, since it allows for an infinite number of jumps in no time, which means that is could respond too quickly to noise. However, if the dwell-time is slower than the noise, this would work as a noise filter. For the sampled version a dwell-time is needed in order to sample values of x_1.

For the second simulation run where $\dot{x}_1$ is found by sampling, a sampling period of $T_s = 0.03s$ is applied. Let x_1' be the value of x_1 at previous sampling instant. Then $\dot{x}_1$ is found from

$$\dot{x_1} = \frac{x_1 - x_1'}{T_s}. \tag{5.80}$$

White noise of power 0.1 is added to make the sampling process more realistic. It is not crucial that the value for $\dot{x}_1$ is correct, but it should be close in magnitude to the true value, at least when close to the boundary of the jump set. This is because $\dot{x}_1$ is just used as a jump condition (defines the jump set), and the value itself is not used in any feedback.

Results first order system - with knowledge of x_2

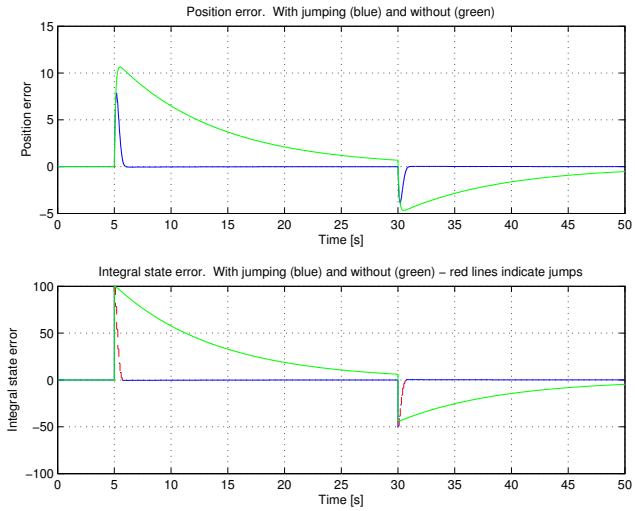

Figure 5.1: Position and integral state error first order system, no sampling

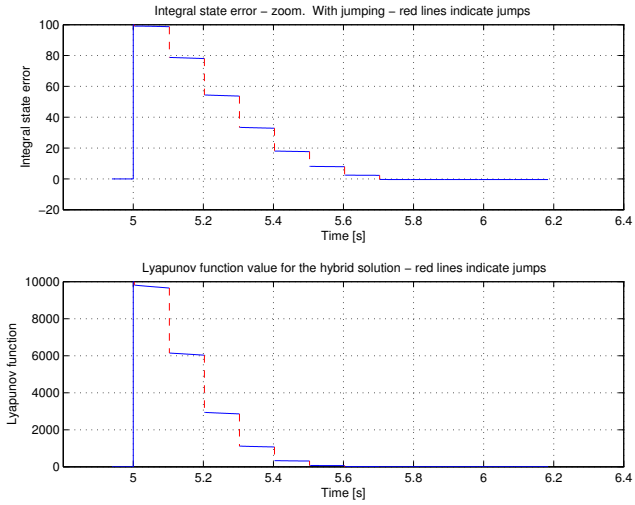

Figure 5.2: Lyapunov function and integral state error zoom at time $t = 5s$, no sampling

Results first order system - without knowledge of x_2

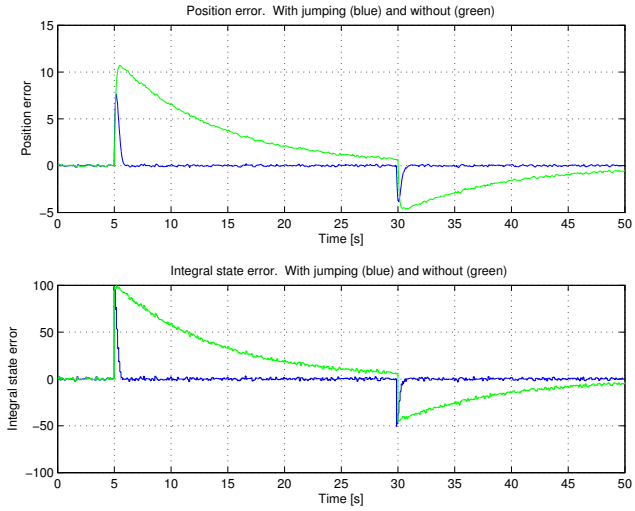

Figure 5.3: Position and integral state error first order system, with sampling, and white noise.

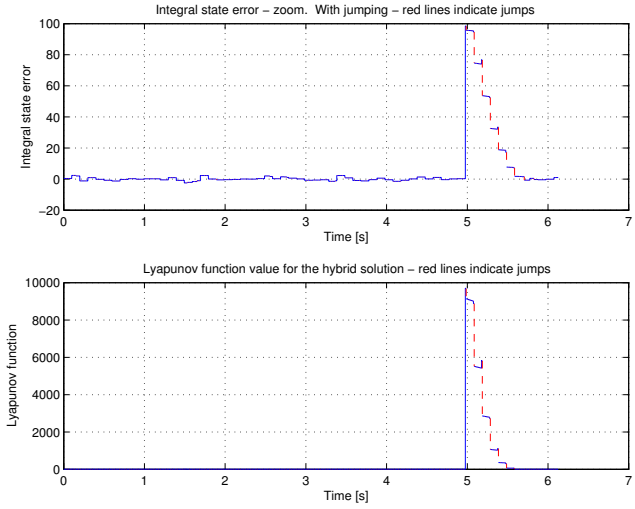

Figure 5.4: Lyapunov function and integral state error zoom at time $t = 5s$, with sampling, and white noise.

5.3.2 Example - DP

In this example, knowledge of $\boldsymbol{x}_3$ will be assumed known for the first simulation run. For the second simulation, $\boldsymbol{x}_2$ will be sampled to find an estimate of $\dot{\boldsymbol{x}}_2$. Some noise will be added to this simulation, to make the sampling process more realistic.

Consider the closed loop DP system of Eq. (5.43 - 5.45) as

$$\dot{\boldsymbol{x}}_1 = -r\boldsymbol{S}\boldsymbol{x}_1 - \boldsymbol{K}_p\boldsymbol{x}_1 + \boldsymbol{x}_2 \tag{5.81}$$
$$\boldsymbol{M}\dot{\boldsymbol{x}}_2 = -\boldsymbol{x}_1 - \boldsymbol{K}_d\boldsymbol{x}_2 + \boldsymbol{R}(\psi)^\top\boldsymbol{x}_3 \tag{5.82}$$
$$\dot{\boldsymbol{x}}_3 = -\boldsymbol{K}_i\boldsymbol{R}(\psi)\boldsymbol{x}_2 \tag{5.83}$$

with

$$\boldsymbol{M} = diag\{450, 450, 100\} \tag{5.84}$$
$$\boldsymbol{K}_p = diag\{100, 100, 50\} \tag{5.85}$$
$$\boldsymbol{K}_i = diag\{10, 10, 5\} \tag{5.86}$$
$$\boldsymbol{K}_d = diag\{500, 500, 200\}, \tag{5.87}$$

and λ, ε_1, and ε_2 chosen as

$$\lambda = 25, \tag{5.88}$$
$$\varepsilon_1 = 0.0001, \tag{5.89}$$
$$\varepsilon_2 = 0.01. \tag{5.90}$$

For both simulations a step of magnitude

$$\boldsymbol{b} = \begin{bmatrix} 3000 \\ 2000 \\ 1000 \end{bmatrix}, \tag{5.91}$$

is applied at time $t = 10s$.

By the same reasoning as for the example for the first order system of Section 5.3.1 a dwell-time is added between jumps here as well. The dwell chosen is $T = 0.1s$.

Similar to the example for the first order system of Section 5.3.1 a dwell-time is needed in order to sample values of x_2. For the second simulation run where $\dot{\boldsymbol{x}}_2$ is found by sampling, a sampling period of $T_s = 0.03s$ is applied. Let $\boldsymbol{x}_2'$ be the value of $\boldsymbol{x}_2$ at previous sampling instant then $\dot{\boldsymbol{x}}_2$ is found from

$$\dot{\boldsymbol{x}}_{\boldsymbol{2}} = \frac{\boldsymbol{x}_2 - \boldsymbol{x}_2'}{T_s}. \tag{5.92}$$

In the second simulation noise of power 20 has been added in all DOF.

Results DP - with knowledge of x_3

For the results below is says (N), (E), $(Heading)$, on the plots, but this is not entirely the case. The $\boldsymbol{x}_1$ state is $\tilde{\boldsymbol{\eta}}$ transformed to body coordinates, and $\boldsymbol{x}_2$ is not equal to $\boldsymbol{\nu}$, but in the plots $\boldsymbol{x}_1$, and $\boldsymbol{x}_2$ are called "position" and "velocity".

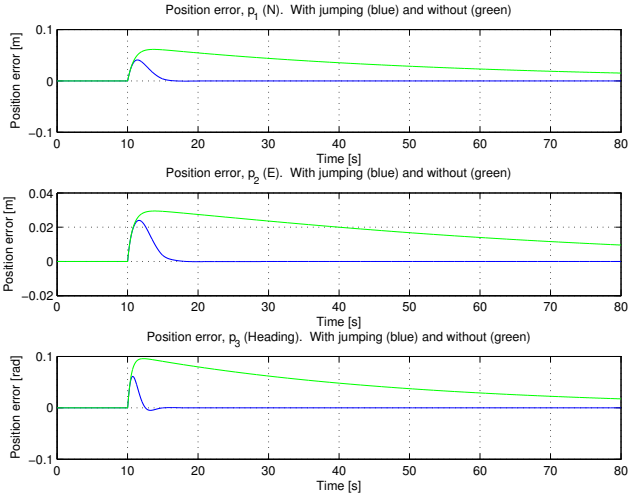

Figure 5.5: Position error DP, no sampling

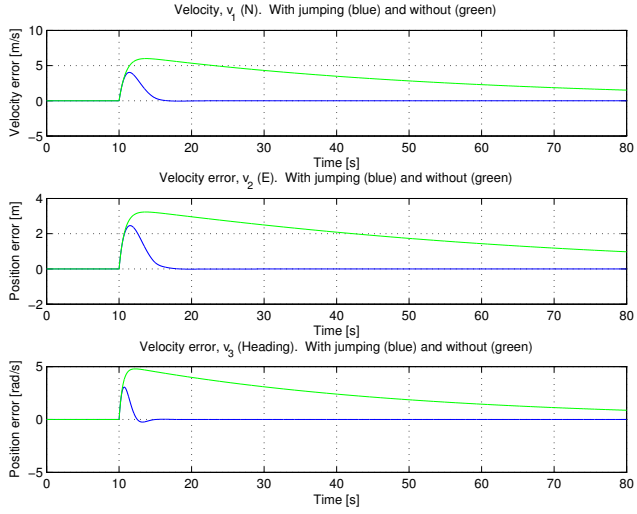

Figure 5.6: Velocity error DP, no sampling

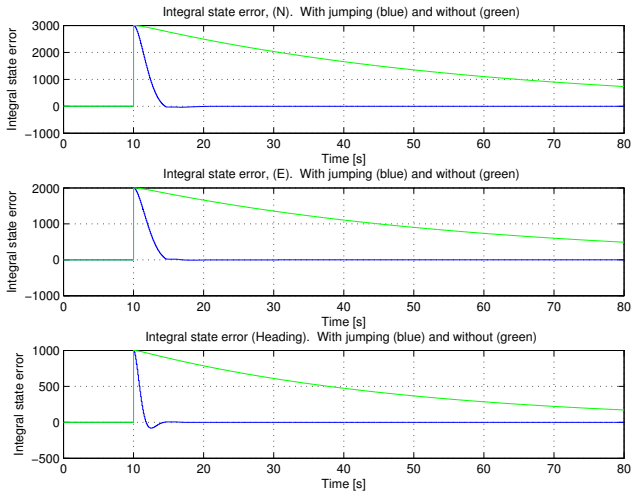

Figure 5.7: Integral error DP, no sampling

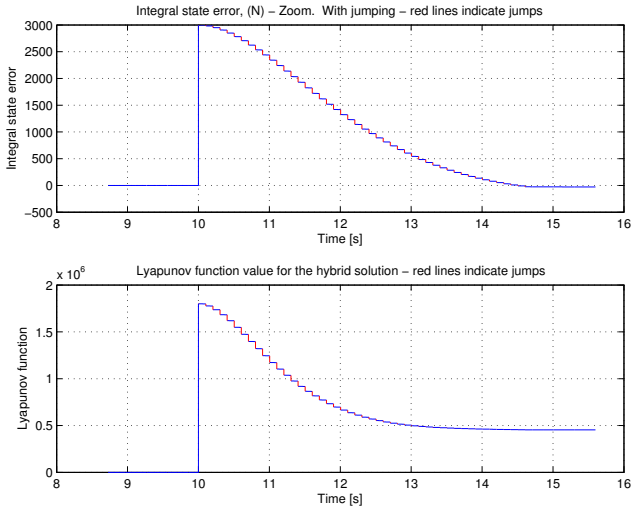

Figure 5.8: Lyapunov function and zoom on integral error, no sampling

Results DP - without knowledge of x_3 - sampling of x_2

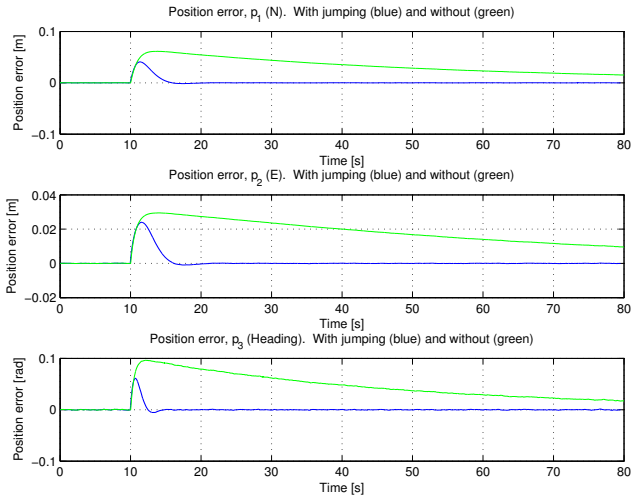

Figure 5.9: Position error DP, with sampling

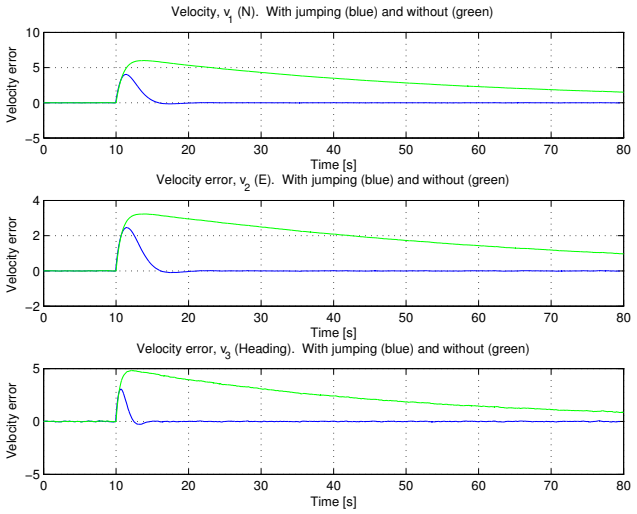

Figure 5.10: Velocity error DP, with sampling

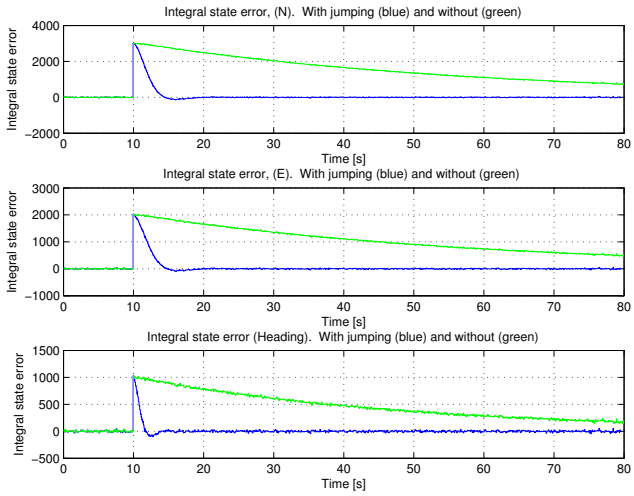

Figure 5.11: Integral error DP, with sampling

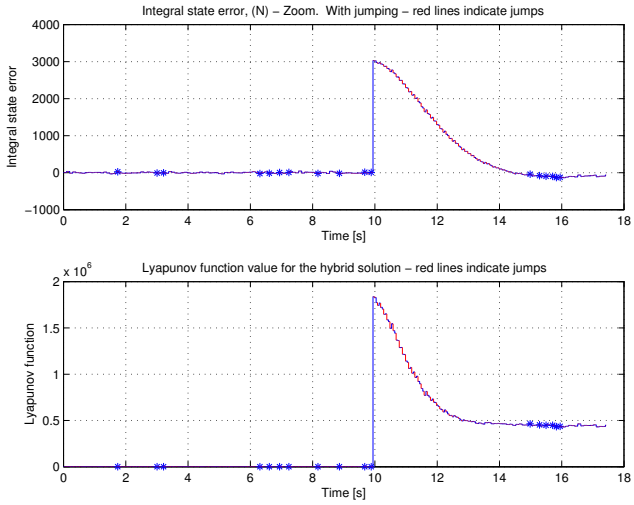

Figure 5.12: Lyapunov function and zoom on integral error, with sampling

5.4 Conclusions and further work

For both the first order linear system, and the DP system the hybrid integral action improves performance for large constant disturbances. The state estimates, and the integral action error converge much faster than in the case without jumps. After a step the integral action converge to the new value quickly, and (almost) without overshoot. When sampling

is used to find the jump set, the performance decrease is negligible compared to the ideal case, and the noise does not induce problems.

For further work the algorithm should be tested on more realistic data, either a comprehensive numerical ice simulation, or a model test for a DP vessel subject to large step changes in disturbances. It would be interesting to see how this approach could improve performance (offset from desired position), thrust, and power consumption. One other interesting aspect for a model test is how performance is affected by sensor noise. For the DP system an alternative to sampling the velocity is to use accelerometers to find the accelerations.

Bibliography

Anderson, B. D. O., Bitmead, R. R., Johnson, Jr., C. R., Kokotovic, P. V., Kosut, R. L., Mareels, I. M., Praly, L., Riedle, B. D., 1986. Stability of Adaptive Systems: Passivity and Averaging Analysis. MIT Press, Cambridge, MA, USA.

Batista, P., Silvestre, C., Oliveira, P., 2011. On the observability of linear motion quantities in navigation systems. Systems & Control Letters 60 (2), 101–110.

Chen, C.-T., 2009. Linear System Theory and Design - International Edition, 3rd Edition. Oxford University Press.

El Rifai, K., El Rifai, O., 2009. Design of hybrid resetting pid and lag controllers with application to motion control. In: Advanced Intelligent Mechatronics, 2009. AIM 2009. IEEE/ASME International Conference on. IEEE, pp. 685–692.

Faltinsen, O., 1990. Sea loads on ships and offshore structures. Cambridge University Press.

Fossen, T. I., 2011. Handbook of marine craft hydrodynamics and motion control. John Wiley & Sons.

Goebel, R., Sanfelice, R. G., Teel, A. R., 2012. Hybrid Dynamical Systems: modeling, stability, and robustness. Princeton University Press.

Hong, S., Lee, M. H., Chun, H.-H., Kwon, S.-H., Speyer, J. L., 2005. Observability of error states in gps/ins integration. Vehicular Technology, IEEE Transactions on 54 (2), 731–743.

Hong, S., Lee, M. H., Chun, H.-H., Kwon, S.-H., Speyer, J. L., 2006. Experimental study on the estimation of lever arm in gps/ins. Vehicular Technology, IEEE Transactions on 55 (2), 431–448.

Hong, S., Lee, M. H., Kwon, S. H., Chun, H. H., 2004. A car test for the estimation of gps/ins alignment errors. Intelligent Transportation Systems, IEEE Transactions on 5 (3), 208–218.

Khalil, H. K., 2002. Nonlinear systems, 3rd Edition. Prentice hall Upper Saddle River.

Kongsberg Maritime, 2006. Kongsberg K-Pos Dynamic Positioning - Optimizing complex vessel operations. Brochure.

Nguyen, T. D., Sørensen, A. J., Tong Quek, S., 2007. Design of hybrid controller for dynamic positioning from calm to extreme sea conditions. Automatica 43 (5), 768–785.

Palm, W. J., 2009. System dynamics, 2nd Edition. McGraw-Hill Higher Education.

Parker, M. A., 08 2013. R/v gunnerus summary report offset survey and gyro-calibration additional survey of em3002s survey of dps232, seapath, mru5 and mru5+. Tech. rep., NTNU.

Prieur, C., Tarbouriech, S., Zaccarian, L., et al., 2012. Hybrid high-gain observers without peaking for planar nonlinear systems. Proceedings of CDC 2012.

Rangaiah, G. P., Krishnaswamy, P. R., 1994. Estimating second-order plus dead time model parameters. Industrial & engineering chemistry research 33 (7), 1867–1871.

Rolls-Royce Marine, 2009. Icon DP - A positioning product from Rolls-Royce. Brochure.

Schultz, T., 2013. personal communication.

Seatex, K., 03 2014. Mru 5+. Tech. rep., KM.

Seborg, E. D., Edgar, F. E., Mellichamp, D. A., 2004. "Process Dynamics and Control", 2nd Edition. John Wiley & Sons.

Skjetne, R., Fossen, T. I., 2004. On integral control in backstepping: Analysis of different techniques. In: American Control Conference, 2004. Proceedings of the 2004. Vol. 2. IEEE, pp. 1899–1904.

Slotine, J.-J. E., Li, W., 1991. Applied Nonlinear Control. Prentice hall, Englewood Cliffs.

Smith, C. A., Corripio, A. B., 2006. "Principles and practice of automatic process control", 3rd Edition. Springer, London.

Smith, C. L., 1972. Digital computer process control. Intext Educational Publishers Scranton.

Smogeli, Ø. N., 2006. Control of marine propellers. Ph.D. thesis, Dept. of Marine Technology, Norwegian Univ. of Sci. and Tech.

Sørensen, A. J., 2012. Marine Control Systems - Lecture notes. Department of Marine Technology, Norwegian Univ. of Sci. and Tech.

Strand, J. P., Sørensen, A. J., Ronæss, M., Fossen, T. I., 2001. Position control systems for offshore vessels. In: The Ocean Engineering Handbook. Ed. Ferial El-Hawary Boca Raton CRC Press LLC. 2001.

Tang, Y., Wu, Y., Wu, M., Wu, W., Hu, X., Shen, L., 2009. Ins/gps integration: global observability analysis. Vehicular Technology, IEEE Transactions on 58 (3), 1129–1142.

Appendix

By differentiating Eq. (5.35), using the dynamics from Eq. (5.32), (5.33), and (5.36), and inserting for the virtual control $\mu(\eta, t)$ given by (5.37), and the controller τ given by (5.38), the resulting closed loop dynamics for $\dot{x}$ becomes

$$\begin{aligned}
\dot{\boldsymbol{x}}_1 &= \dot{\boldsymbol{R}}(\psi)^\top(\boldsymbol{\eta} - \boldsymbol{\eta}_d(t)) + \boldsymbol{R}(\psi)^\top(\dot{\boldsymbol{\eta}} - \dot{\boldsymbol{\eta}}_d(t)) \\
&= -r\boldsymbol{S}\boldsymbol{R}(\psi)^\top(\boldsymbol{\eta} - \boldsymbol{\eta}_d(t)) + \boldsymbol{\nu} - \boldsymbol{R}(\psi)^\top\dot{\boldsymbol{\eta}}_d(t)) \\
&= -r\boldsymbol{S}\boldsymbol{x}_1 + \boldsymbol{x}_2 + \boldsymbol{\mu}(\boldsymbol{\eta}, t) - \boldsymbol{R}(\psi)^\top\dot{\eta}_d(t)) \\
&= -r\boldsymbol{S}\boldsymbol{x}_1 - \boldsymbol{K}_p\boldsymbol{x}_1 + \boldsymbol{x}_2,
\end{aligned}$$

$$\begin{aligned}
\boldsymbol{M}\dot{\boldsymbol{x}}_{\boldsymbol{2}} &= \boldsymbol{M}\dot{\boldsymbol{\nu}} - \boldsymbol{M}\dot{\boldsymbol{\mu}} \\
&= -D\boldsymbol{\nu} + \boldsymbol{R}(\psi)^\top\boldsymbol{b}(t) + \boldsymbol{\tau} - \boldsymbol{M}\dot{\boldsymbol{\mu}} \\
&= -\boldsymbol{x}_1 - \boldsymbol{K}_d\boldsymbol{x}_2 - \boldsymbol{R}(\psi)^\top(\hat{\boldsymbol{b}} - \boldsymbol{b}) \\
&= -\boldsymbol{x}_1 - \boldsymbol{K}_d\boldsymbol{x}_2 - \boldsymbol{R}(\psi)^\top\boldsymbol{x}_3,
\end{aligned}$$

such that the closed loop dynamics is given as

$$\begin{aligned}
\dot{\boldsymbol{x}}_1 &= -r\boldsymbol{S}\boldsymbol{x}_1 - \boldsymbol{K}_p\boldsymbol{x}_1 + \boldsymbol{x}_2 \\
\boldsymbol{M}\dot{\boldsymbol{x}}_2 &= -\boldsymbol{x}_1 - \boldsymbol{K}_d\boldsymbol{x}_2 + \boldsymbol{R}(\psi)^\top\boldsymbol{x}_3 \\
\dot{\boldsymbol{x}}_3 &= -\boldsymbol{K}_i\boldsymbol{R}(\psi)\boldsymbol{x}_2
\end{aligned}$$